INCORPORATING CELLULOSE NANOCRYSTALS INTO WATERBORNE ACRYLIC COATINGS TOWARDS ECO-FRIENDLY FORMULATIONS

A Dissertation
Presented to
The Academic Faculty

By

Ezgi Melis Dogan Guner

In Partial Fulfillment
of the Requirements for the Degree
Doctor of Philosophy in the
School of Chemical & Biomolecular Engineering

Georgia Institute of Technology

August 2021

INCORPORATING CELLULOSE NANOCRYSTALS INTO WATERBORNE ACRYLIC COATINGS TOWARDS ECO-FRIENDLY FORMULATIONS

Approved by:

Dr. Carson Meredith, Advisor
Chemical & Biomolecular Engineering
Georgia Institute of Technology

Dr. F. Joseph Schork
Chemical & Biomolecular Engineering
Georgia Institute of Technology

Dr. Meisha L. Shofner, Co-advisor
Materials Science & Engineering
Georgia Institute of Technology

Dr. Gregory T. Schueneman
Forest Products Laboratory
U.S. Forest Service (USFS)

Dr. Martha Grover
Chemical & Biomolecular Engineering
Georgia Institute of Technology

Date approved: June 7, 2021

Dedicated to my grandmother,

Aysel Şen (1947-2020), who taught me compassion, kindness, and patience.

ACKNOWLEDGMENTS

This dissertation would not be possible without the guidance and support of numerous people. First, I would like to thank my advisors, Dr. Carson Meredith and Dr. Meisha Shofner, for their mentorship and continuous support. I appreciate the opportunity you gave me to do a unique research that challenged me during my studies; I learned a lot in the last four years. I would like to thank the dissertation committee members: Dr. Joseph Schork, Dr. Gregory Schueneman, and Dr. Martha Grover. They provided valuable feedback on my thesis proposal, pre-doctoral review, and this dissertation. Also, I thank my collaborator, Stan Brownell at Dow Chemical, for the helpful discussions that contributed to my learning and development in the coating field. I am grateful to the material characterization facility staff at Georgia Tech for their teaching and support for the material characterizations in my studies. Additionally, I would like to acknowledge p3Nano program by U.S. Endowment for Forestry and Communities, Inc. for providing funding and U.S. Forest Service Forest Products Laboratory for providing cellulose materials used in my project.

I thank the present and some past members of the Meredith and Shofner research groups: Zihao Qu, Chinmay Satam, Songcheng Wang, Madelyn Smart, Omotola Okesanjo, Yue Ji, Aaron Liu, Tanner Hickman, Rahul Venkatesh, Zeyang Yu, Yang Lu, Cameron Irvin, Matthew Orr, Zach Seibers, Ian Pelse, Emily Ryan, Keya Shial, Andrew Morgenstern.

I would like to take this opportunity and show my appreciation to Gamze, Cansu, Dogukan, Damla, Efe, Sezen, and Berkay for their friendship and the great times we spent outside the school.

I would like to express my deepest gratitude to my parents: Metin and Belkis, my sister: Ecrin, my grandparents: Bahattin and Aysel, my father-in-law: Turgut, my mother-in-law: Nuran, my brothers-in-law: Sergen and Ali, and my sisters-in-law: Tugba, Seda, and Eda, for their love, encouragement, and support from overseas.

Last but certainly not the least, to my husband and my best friend, Feyyaz Guner: thank you for being always by my side with your unconditional love, kindness, support, and encouragement. Thank you for trusting me more than myself. Thank you for keeping our lives on track when I was too busy with experiments. Thanks for your companionship in the late-night lab visits. Thank you for so many more things I cannot finish counting. You are the joy of my life, and I am looking forward to starting a new chapter in our life.

Finally, I would like to dedicate this dissertation to my grandmother, Aysel Şen, who recently passed away. I had her unwavering love and support ever since my first moment in this life. No other person could fill her special place in my heart.

TABLE OF CONTENTS

LIST OF TABLES

LIST OF FIGURES

LIST OF SYMBOLS AND ABBREVIATIONS

Symbols

E_A	Axial elastic modulus
T_g	Glass transition temperature
M_n	Number average molecular weight
α	Significance level in t-test

Abbreviations

AFM	Atomic force microscopy
AGU	Anhydroglucopyranose unit
ATR-FTIR	Attenuated total reflection-Fourier transform infrared spectroscopy
BA	Butyl acrylate
BPO	Benzoyl peroxide
CMC	Critical micelle concentration
CNC	Cellulose nanocrystal
CNF	Cellulose nanofiber
DBTDL	Dibutyltin dilaurate
DMA	Dynamic mechanical analysis
DMF	Dimethylformamide
DMSO	Dimethyl sulfoxide
DS	Degree of substitution
DSC	Differential scanning calorimetry
EA	Ethyl acrylate

FE-SEM	Field emission-scanning electron microscopy
GPC	Gel permeation chromatography
HD	Hexadecane
HEMA	Hydroxyethyl methacrylate
HTMECH	High-throughput mechanical characterization
IEM	Isocyanatoethyl methacrylate
KPS	Potassium persulfate
LCA	Life cycle assessment
MAA	Methacrylic acid
MFFT	Minimum film formation temperature
MMA	Methyl methacrylate
NMR	Nuclear magnetic resonance
PBA	Poly(butyl acrylate)
PLM	Polarized light microscopy
PMMA	Poly(methyl methacrylate)
PSA	Pressure sensitive adhesive
SDBS	Sodium dodecyl benzene sulfonate
SI-ATRP	Surface-initiated atom transfer radical polymerization
SLS	Sodium lauryl sulfate
TEM	Transmission electron microscopy
TGA	Thermogravimetric analysis
THF	Tetrahydrofuran
UTS	Ultimate tensile strength
UV-Vis	Ultraviolet-visible
VOC	Volatile organic compound
XPS	X-ray photoelectron spectroscopy
XRD	X-ray diffraction

SUMMARY

Waterborne coatings are primarily produced by using hard acrylic polymers with a moderate glass transition temperature ($T_g \sim 48$ °C) to provide adequate hardness, adhesion strength, and surface uniformity. Hard acrylic latexes cannot form a continuous polymer film at ambient conditions; therefore, coating formulations include volatile organic compounds (VOCs) as coalescents to ensure film formation. However, volatile coalescents evaporate during drying of the coatings, resulting in air pollution and health concerns. The industry has been working to reduce VOC levels in the formulations to meet demanding environmental regulations. Non-volatile coalescent alternatives have been developed, but they often result in tacky coatings and lack adequate hardness by remaining in the coating long-term. Soft latex particles easily form a continuous film at ambient conditions without coalescents; however, the resulting film lacks adequate hardness. Successfully balancing hardness while reducing VOCs and ensuring proper film formation is challenging. This dissertation explores the incorporation of cellulose nanocrystals (CNCs) as performance additives to improve the hardness and strength of ambient film-forming latex coatings. CNCs are stiff rod-shaped nanomaterials and possess attractive properties, including high specific strength and modulus, low density compared to other hard fillers, and tunable surface chemistry. The research in this dissertation aims to provide a methodology for incorporating CNCs into different phases of polymer latexes: aqueous and polymer phases; also aims to understand the effect of CNC location on the latex properties. Moreover, a versatile surface modification scheme was developed for CNCs to increase their compatibility with the organic phase of latex.

First, unmodified CNCs (umCNCs) were incorporated into the aqueous phase of ambient film-forming acrylic latex by a post-synthesis blending approach. CNCs formed nano-sized aggregates within the interstitial regions between latex particles as water dries; however, film coalescence was not compromised. Films with 15 wt% CNC showed almost

230% improvement in Koenig hardness and 10× improvement in the nanoindentation hardness compared to neat films, achieving properties similar to hard VOC-containing acrylic binders. This work showed the remarkable effect of using CNCs to improve the mechanical performance of ambient film-forming acrylic coatings.

Second, a surface modification method was investigated for CNCs to increase their compatibility with acrylic monomers to be used in the latex synthesis. Isocyanatoethyl methacrylate (IEM), a bifunctional molecule carrying both isocyanate and vinyl functional groups, was chosen for the modification. Isocyanate groups of IEMs were used to react with hydroxyl groups on the CNC surface (urethanization) and the pendant vinyl groups provided macromonomer functionality to the CNCs. The influence of urethanization reaction time and temperature was studied to optimize the degree of substitution, crystallinity, and morphology of the CNCs. The degree of modification was a strong and increasing function of reaction temperature over the range studied. However, the highest temperature (65 °C) and the longest time of reaction (6 h) resulted in shorter, thinner, and less crystalline CNCs. Also, the copolymerization ability of mCNCs was verified by polymerizing attached IEMs with acrylic monomers via solution polymerization. The polymer grafting facilitated a more homogeneous dispersion in acrylic polymer matrix compared to unmodified CNC (umCNC). The more homogeneous dispersion of polymer-grafted CNCs resulted in approximately 100% improvement in the tensile strength and about 53% enhancement in the hardness of the acrylic films relative to neat and umCNC loaded films. This study demonstrated a versatile modification scheme resulting in tunable macromonomer functionality and polymer grafting.

Finally, CNCs were incorporated into the polymer phase of latex via miniemulsion polymerization. Different types of CNCs (unmodified, modified/macromonomer, and polymer-grafted) were prepared to be used in the monomer phase of miniemulsion. The macromonomer and polymer-grafted CNCs favored the monomer phase based on partition tests, whereas umCNCs preferred the water phase. Miniemulsion polymerizations were per-

formed with CNCs (1 wt%) added into the monomer phase. AFM images displayed the umCNCs outside the latex particles and the polymer-grafted CNCs as partially embedded in the latex particles. However, macromonomer CNCs coagulated during the polymerization and therefore could not be incorporated into the latex system. This comparison emphasizes how the compatibility of CNCs with the monomer phase is essential to maintain the CNCs in the organic phase during the miniemulsion. The addition of polymer-grafted CNC did not improve the mechanical properties of latex films relative to the neat and umCNC-added latex. The high amount of polymer grafting on CNCs and the limited CNC loading (1 wt%) may be the reasons preventing the improvement in the mechanical properties of the latex films. This result underlined the importance of optimization for polymer grafting of CNCs to use their reinforcement potential effectively.

Overall, the findings in this dissertation will guide the researchers in the paint, coating, and cosmetic industries to extend the use of CNCs in waterborne formulations. The knowledge presented will contribute to development of latex binders with CNCs for more environmentally friendly waterborne coatings.

CHAPTER 1
INTRODUCTION

This chapter first delivers background knowledge about coatings in general, waterborne acrylic formulations, and the structure of cellulose/nanocellulose. Afterward, motivation, objectives and outline of the research presented in this dissertation are provided.

1.1 An overview of paints and coatings

Coatings are a part of our daily lives, from automobiles, computers, furniture to aerospace vehicles and military applications. A coating is described as either a continuous or discontinuous film formed after drying a material applied on a surface [1]. The material applied or the process of application is also known as a coating. The coating material is typically liquid and dries by carrier solvent evaporation or different curing methods, including oxidative, ultraviolet light, or thermal. The terms *paint* and *coating* are frequently used as synonymous, even though coating is a general term and paint is one kind of coating material. Paint is a dispersion composed of polymer/resin (also called binder), carrier medium (organic solvents or water), pigments, and additives such as catalysts, coalescents, antifoaming agents, flow agents [2]. The polymer or resin provides adhesion of the coating to the applied surface, forms a continuous film and binds the solid components of the paint in the final film [3]. The type of binder, carrier medium, pigments and additives vary depending on the formulation purpose.

When the paint components are dispersed in organic solvents, the coating is solvent-borne. If the medium is water, then the coating is waterborne. In the solid (100%) paints, such as powder coatings, the pigments and additives are dispersed in the binder [3]. Binders are macromolecular materials with a molecular weight ranging from 500-30000 g/mol [4]. A variety of polymers and resins have been used based on the area of application. The

low molecular weight binders (e.g., alkyds, polyurethanes, amino resins, phenolic resins, epoxide resins) need a further chemical reaction to form a continuous film after applying to the substrate. The chemical reaction provides high molecular weight cross-linked macromolecules. The high molecular weight binders such as vinyl, acrylic, polyvinyl acetate, and polyester resins do not require a chemical reaction during drying. Acrylics are now one of the heavily used binder classes in commercial paints and coatings [5].

Paints and coatings have a growing market estimated at approximately 43 million tons in 2016 [6] because of various large end-use industries such as automotive, marine, construction, and industrial/OEM. Paints and coatings fall into three broad categories: architectural, industrial, and specialty coatings. Architectural products make up the largest category of this market. Producers have adopted low-solvent technologies in the past 40 years, including waterborne coatings, high solid coatings, powder coatings, and radiation-curable coatings [7]. Waterborne formulations are the leading product segment in the architectural category, with a value of over USD 49 billion in revenue in 2016 [6]. Waterborne acrylics dominate the architectural coatings and also frequently used in industrial painting [6].

1.2 Acrylic resins and waterborne acrylic coatings

An acrylic resin is a polymeric material that can be solid, solution in organic solvents, or aqueous dispersion in water (latex). Acrylics were first introduced to coatings in 1930s in solventborne formulations, and their commercial use grew significantly due to the benefits of acrylics compared to other binders [8]. These resins offer excellent exterior durability (weather resistance), water resistance, transparency, gloss/color retention, and tunability for various applications. In the 1950s, waterborne coatings were first available with the use of styrene-butadiene latexes [9]. Following increasing concerns about solvent use and its environmental effects, waterborne coatings were then developed with a broader range of resins. Waterborne acrylic latexes have been improved over the years and now they are widely used as architectural and industrial coatings [10].

Acrylic polymers are a class of vinyl polymers obtained from acrylate monomers. These monomers are esters of acrylic acid and its derivatives; for example, methacrylates from methacrylic acid (Figure 1.1). Acrylic resins may also contain non-acrylic monomers such as styrene and vinyl acetate at lower fractions for tuning the properties or lowering the cost [5].

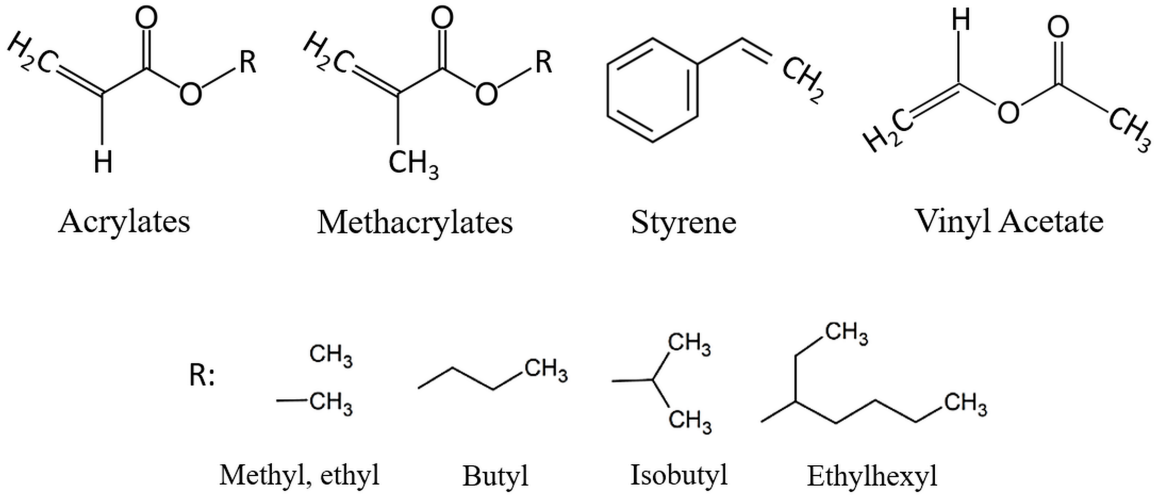

Figure 1.1: General molecular structures of monomers used in acrylic resins.

A wide range of acrylic monomers possessing different hydrophobicity, glass transition temperature (T_g), and functionality (hydroxyl, amine, epoxy, or isocyanate) are available. Therefore, acrylic polymers with various physical and chemical properties can be designed by choosing suitable monomers. Table 1.1 shows some examples of acrylic monomers with their T_g values and water solubilities.

Waterborne acrylic coatings are obtained from water-based acrylic polymers, known as latexes. Acrylic latex is a stable aqueous dispersion of nano/micro scale acrylic polymer particles. Each spherical particle contains many acrylic polymer chains. Copolymerization is extensively used to tailor the properties of the final coatings [11]. For example, the molar ratio of the monomers used in the copolymer determines the T_g of the final polymer, affecting the coating's cohesive strength (hardness), elasticity, and film formation temperature. Acrylic latexes have found numerous applications, including household paints, pressure

Table 1.1: Examples of the monomers used to produce acrylic binders.

Name	T_g (°C)	Water solubility (mmol/L)
Acrylates		
Acrylic acid	110	miscible
Methyl acrylate	8	741
Ethyl acrylate	-22	233
Butyl acrylate	-54	5.8
2-ethylhexyl acrylate	-65	0.971
Methacrylates		
Methacrylic acid	155	miscible
Methyl methacrylate	105	150
Butyl methacrylate	20	2.5
Isobutyl methacrylate	48	9.2
Non-acrylic monomers		
Styrene	100	4.3
Vinyl acetate	29	565

sensitive adhesives (PSAs), textiles, construction materials, paper coatings, and inks for printing. Polymer latexes are prepared mainly by oil-in-water emulsion polymerization or by oil-in-water miniemulsion polymerization, a newer process relative to conventional emulsion polymerization. These polymerization methods are described in the following section.

1.2.1 Preparation techniques

Emulsion and miniemulsion polymerizations are each a type of dispersed-phase polymerization process. In the dispersed-phase polymerization, the dispersed phase is a liquid monomer/s, whereas the continuous phase is usually water. During polymerization of the dispersed monomer, water helps to keep the viscosity of the dispersion low, facilitating the removal of the heat of reaction due to polymerization. Since the continuous phase is water, dispersed-phase polymerization is environmentally friendly and inexpensive compared to solution polymerization. Research efforts on emulsion polymerization and miniemulsion polymerization have grown over the years; the number of publications have increased (Figure 1.2). Miniemulsion polymerization is a relatively new and a specialized field of

study compared to emulsion polymerization. Although miniemulsion polymerization was discovered about 40 years later than emulsion polymerization, the number of contributions with miniemulsion have risen about five-fold since 2000s.

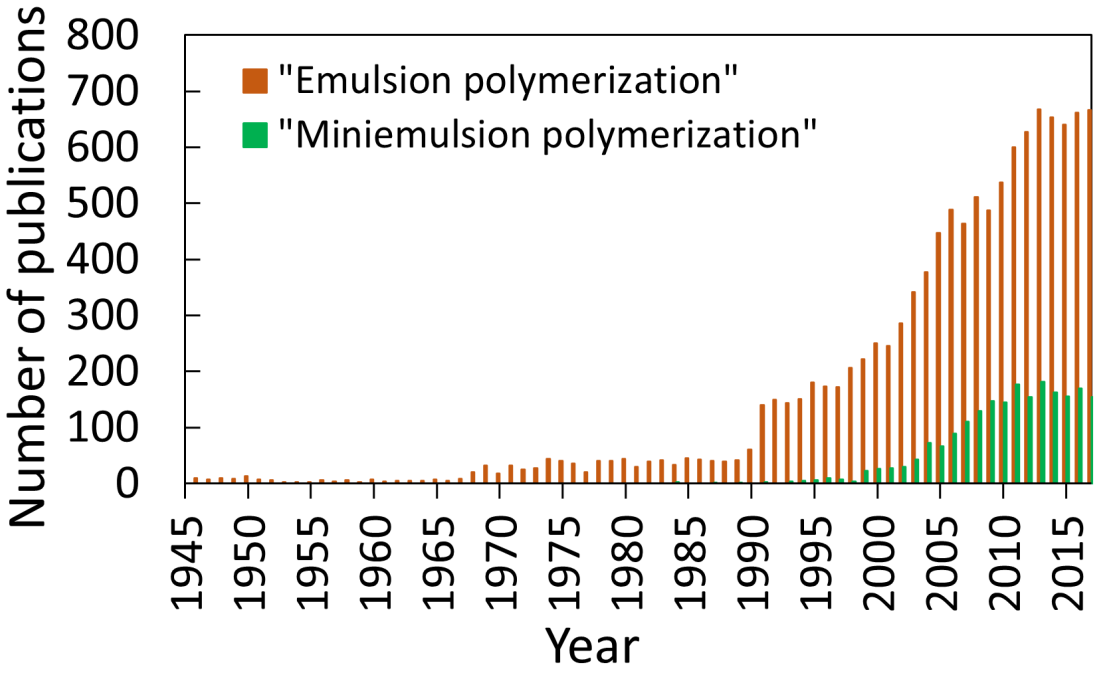

Figure 1.2: Annual number of scientific publications between 1944-2018 with a topic search using keywords of "emulsion polymerization" and "miniemulsion polymerization" in Web of Science in April 2021.

Both emulsion and miniemulsion are initially aqueous dispersions of monomer droplets stabilized by surfactants. The monomer polymerizes via typically free-radical polymerization forming polymer particles; however, the polymerization process of emulsion and miniemulsion have different particle growth mechanisms (Figure 1.3).

In conventional emulsion polymerization, the monomer is mixed with an aqueous surfactant solution and dispersed in the water phase by applying shear to the mixture. Some surfactants stabilize the monomer droplets (1-10 μm diameter) [12], and the remaining surfactants with a concentration above critical micelle concentration (CMC) form micelles in the aqueous phase. The monomer is distributed between the droplets, micelles, and the aqueous phase. Some monomer molecules reside in the interior of micelles, resulting in

monomer-swollen micelles (about 2-10 nm diameter) [13]. Moreover, a small number of monomer molecules dissolve in the water phase, depending on the water solubility of the monomer used. A water-soluble initiator is added to initiate the polymerization with radicals. Emulsion polymerization takes place in three main intervals, as shown in Figure 1.3a. In the first interval, the radicals form and grow with monomers in the aqueous phase, becoming oligomers. Then, these oligomers either enter into micelles after enough propagation (known as micellar nucleation) or form the primary latex particles when they become large enough in the aqueous phase (known as homogeneous nucleation). The monomer conversion is only 2-10%, and the monomer is mainly in the large droplets. The entry of oligomer radicals to monomer droplets (known as droplet nucleation) is insignificant in this interval due to the relatively large size of monomer droplets compared to micelle size. The second interval relies on the diffusion of monomers from relatively large monomer droplets into the monomer-swollen micelles. Monomer droplets act like a reservoir and supply monomers to the chain growth in the micelles. Polymer particles grow until the monomer droplets are exhausted. In the last interval, monomer droplets disappear, and the polymer particles become monomer starved as the monomer concentration decreases towards the end of the polymerization. The diameter of final polymer particles in the latex ranges from 50 to 500 nm [12].

In miniemulsion polymerization, the size of monomer droplets is reduced sufficiently to increase the number and the total surface area of monomer droplets. Either water-soluble or oil-soluble initiators can be used due to the small size of monomer droplets [3]. Therefore, radicals mostly grow in the droplets and droplet nucleation becomes the dominant mechanism for the polymerization. Miniemulsion initially contains smaller (< 0.5 μm) [12] monomer droplets stabilized with an effective surfactant and costabilizer system. These small droplets are obtained by using a high shear device to break up the emulsion droplets that are naturally formed after mixing the aqueous and monomer phases. Sonication has been the most popular high shear device used in laboratory investigations. Mass transfer

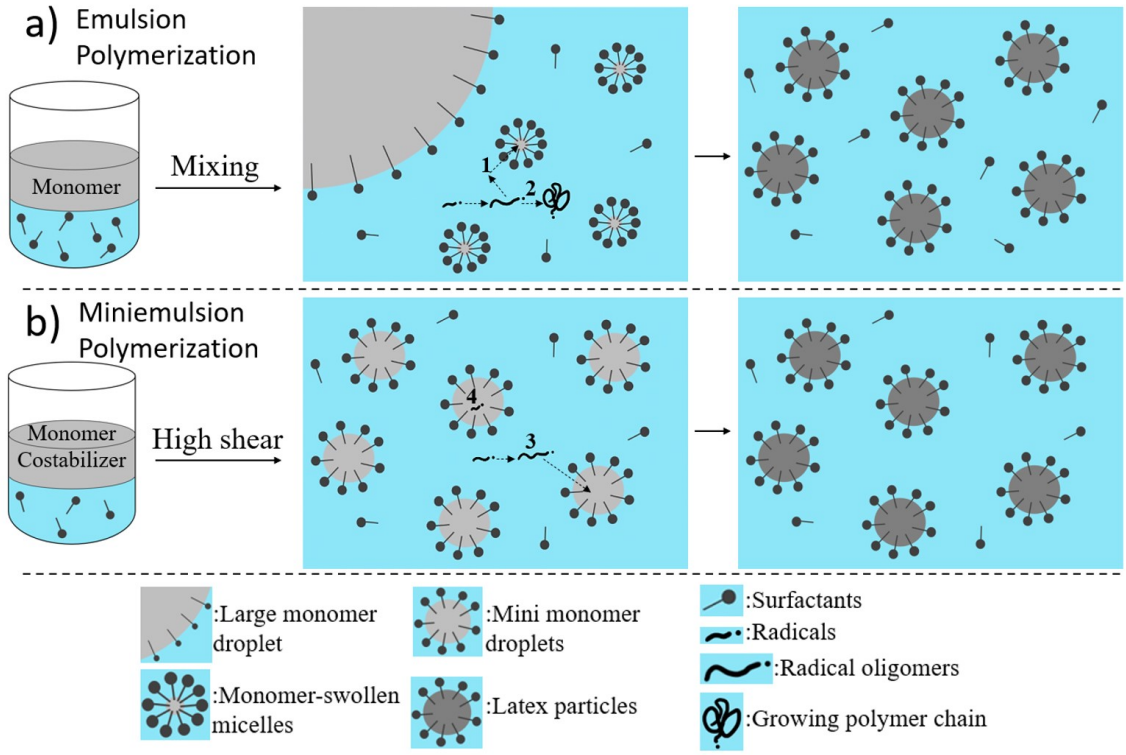

Figure 1.3: Schematic diagram showing the initial states and polymerization mechanisms for a) conventional emulsion polymerization and b) miniemulsion polymerization (1: micellar nucleation, 2: homogeneous nucleation, 3: droplet nucleation with water-soluble initiators, 4: droplet nucleation with oil-soluble initiators).

is limited between droplets. The size of monomer droplets is maintained using a water-insoluble component known as costabilizer to retard monomer diffusion from the submicron monomer droplets [12]. Typically used costabilizers are hexadecane (HD) and cetyl alcohol (CA), which have low molecular weights, high monomer solubilities, and low water solubilities. Almost all surfactants are adsorbed on the surface area of monomer droplets, and no more micelles remain in the aqueous phase. The surfactant concentration in the aqueous phase after miniemulsification should be kept below CMC to avoid the micellar nucleation during the polymerization. While surfactants provide stability against coalescence of the monomer droplets, costabilizers prevent the diffusion of monomers (Ostwald ripening). Therefore, the size of droplets is maintained during the polymerization and final polymer particles that are in a similar size to the initial droplets can be produced.

Table 1.2 shows the differences between emulsion polymerization and miniemulsion polymerization in colloid components, polymerization mechanisms, and advantages/disadvantages. Since the monomer droplets act as *nanoreactors*, miniemulsion polymerization has advantages over conventional emulsion polymerization. First, the latex size can be controlled by adjusting the droplet size with the surfactant and the sonication parameters. Second, the particle size distribution is more reproducible since the size is not affected by polymerization parameters, unlike in emulsion polymerization. These advantages are favorable for the encapsulation of preformed particles inside the polymer particles. More details about encapsulation via miniemulsion polymerization are available in Chapter 4.

Table 1.2: Characteristics of emulsion and miniemulsion polymerizations.

	Polymerization type	
	Emulsion	Miniemulsion
Principle components	Heterogeneous mixture: -Monomer -Water -Surfactant (above CMC) -Initiator (typically water-soluble)	Heterogeneous mixture: -Monomer -Hydrophobe -Water -Surfactant (below CMC) -Initiator (either water-soluble or oil-soluble)
Initial state	Large monomer droplets (1-10 μm) and micelles in the aqueous phase	Small monomer droplets (< 0.5 μm) and no micelles in the aqueous phase
Primary mechanisms for particle growth	-Micellar nucleation -Homogeneous nucleation	-Droplet nucleation
Final latex size	50-500 nm	50-500 nm
Advantages	-No need for costabilizer	-Increased latex shear stability -Reproducible particle nucleation -No monomer transport limitations
Disadvantages	-Dependence of kinetics and particle size on the polymerization parameters -Need for slightly water-soluble monomers due to the diffusion mechanism	-Adoption for industrial processes due to miniemulsification step

1.2.2 Film formation

The properties of acrylic coatings depend on not only basic polymer properties such as copolymer composition, molecular weight, and chain sequence but also the film formation process. This process involves drying of latex deposited on a substrate until obtaining a continuous film. Film formation has three phases: particle packing, particle deformation, and interdiffusion across the latex particle boundaries (Figure 1.4). Water evaporation increases the particle concentration and results in a hexagonal closed-packed network. After that, particle deformation begins, and the void space between particles is filled. The contact between adjacent polymer particles initiates polymer diffusion between particles, termed coalescence. Many articles [14–16] reviewed the studies in the literature about the mechanism of latex film formation.

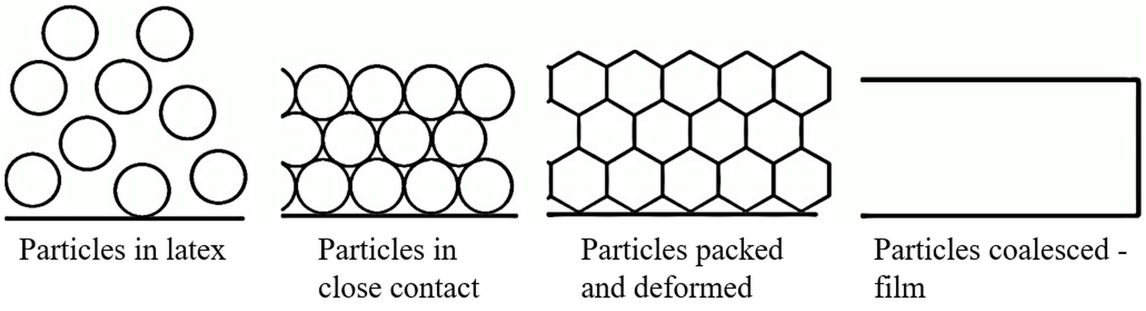

Figure 1.4: Film formation process.

Many variables, including polymer T_g, drying temperature, latex particle size, and particle morphology, affect the extent of film formation [17]. Latexes have their characteristic minimum film formation temperatures (MFFTs) depending on their T_g and particle deformability. The MFFT is the lowest temperature resulting in a crack-free and homogeneous film. The drying temperature must be above the MFFT of the latex to allow particle deformation and interdiffusion of polymer chains. A fully coalesced film cannot be formed at drying temperatures below MFFT since the particles are too hard for deformation. The MFFT is closely related to the T_g of the polymers in the latex because the polymer T_g determines the extent of particle deformation.

Acrylic monomers commonly used in latexes such as butyl acrylate and methyl methacrylate produce polymer particles possessing different hardness. Poly(butyl acrylate) has a low T_g (-54 °C), whereas poly(methyl methacrylate) has a high T_g (105 °C). The drying temperature is typically ambient in most architectural coating applications. Therefore, low T_g polymer particles can form a continuous film at ambient temperature, but the resulting films are often tacky and lack film hardness. Conversely, high T_g polymer particles give superior mechanical properties to the film, but complete film formation needs drying at elevated temperatures. Overall, there is a trade-off between ambient film formation and the mechanical performance of the coatings, also known as *film formation dilemma*. The conventional film formation process requires a certain percentage of organic solvents as coalescing aids for film formation. These volatile coalescing aids temporarily plasticize higher T_g polymer particles and allow them to undergo complete film formation at lower temperatures. Lowering T_g increases the interdiffusion of polymer particles by increasing the free volume [18]. The polymer retains its original hardness after complete evaporation of the volatile content.

1.2.3 Characterization of latexes

A variety of physical and chemical characterization methods are typically performed on aqueous polymer dispersions and their resulting latex films. Determining solid content and coagulum fraction of the latex is the first step of any routine characterization after the polymerization. Surface tension, pH, particle size analysis, and zeta potential measurements assess the latex's colloidal stability and particle size distribution. Characterization of flow behavior includes measurement of the rheological properties that influence end-applications. Microscopy and light transmission are used to understand the particle morphology and microstructure of the latex films.

Understanding the film formation process is important because film formation affects the macroscopic and microscopic properties of the film. Thermal properties such as T_g

and MFFT are measured. Chemical composition in polymer films is usually characterized via spectroscopic methods. The transparency and gloss of the latex films are typically characterized by UV-visible spectroscopy. Mechanical characterization of the latex films is generally performed by strain-stress measurements, dynamic mechanical analysis, and hardness measurements. Moreover, many application-specific tests are available in addition to general physical and chemical characterization. The detailed descriptions of various measurement methods followed in this study are provided in the characterization sections of each main chapter.

1.3 Sustainability trends in waterborne coatings

Waterborne formulations decreased the use of solvents compared to traditional solvent-based counterparts; however, the acrylic coating industry remains one of the prominent consumers of solvents [19], named volatile organic compounds (VOCs). VOCs are classified as organic compounds with a boiling point of less than 250 °C [20]. Their content in coatings still varies with different paint systems, ranging from 70% for solvent-based wood stains to 10% for emulsion-based lacquers, 5% for conventional interior paints and less than 0.07% for low-emission interior decorative paints [21]. The primary VOC emissions from conventional latex paints include propylene glycol, ethylene glycol, and (2-butoxyethoxy) ethanol [22]. VOCs give the required mobility to polymer particles in the coating and help develop a better coalescence film during drying. However, the evaporation of these compounds causes environmental and health-related problems. VOCs used in coatings release toxic oxidants to the atmosphere, damaging the ozone layer and contributing to greenhouse gases [23]. Moreover, workers in coating applications have raised health concerns due to long-term exposure to VOC emissions [24, 25].

Regulations have been applied towards reducing the use of coalescent to decrease the level of toxic volatile chemicals in the atmosphere. For example, European Union (EU) implemented EU Directive 2004/42/EC legislation to reduce the maximum VOC content

limits (from 150 g/L to 100 g/L for interior glossy walls and ceilings) in 2010 [26]. China has instituted a 5% tax on all coatings with VOC content greater than 400 g/L [27].

Coating producers are under increased pressure to eliminate VOCs because of the legislation and strong customer demand for such products. However, the removal of VOC use can cause negative impacts on the performance and quality of paints. Various approaches have been followed to manage the *film formation dilemma*. Table 1.3 summarizes these approaches, their effects, and the related limitations. One approach is to prepare composites of hard and soft polymers in the latex by either blending particles [28, 29] or synthesizing core/shell particle morphologies [30, 31]. The second approach is to dry coatings at elevated temperatures [32]. Also, introducing hydrophilic groups such as acrylic acids can reduce the use of coalescent such that hydrophilic groups interacting with water swell the latex particles, producing a plasticization effect [33]. However, these methods have their limitations and there is still a need for new approaches to eliminate the use of VOCs.

Table 1.3: Different approaches to achieve film formation of a hard latex film.

Approach	Effect	Drawback
Using coalescent aid	Reduces T_g and MFFT	High VOC emission
Placing latex film in an oven	Facilitates particle deformation	Energy-intensive
Modifying polymer with particle blends or heterogenous particle	Manipulates MFFT	Reduced hardness Slower property development
Introducing hydrophilic groups to the polymer	Plasticize the polymer	Water uptake in coatings

1.4 Cellulose and nanocellulose

1.4.1 Cellulose

Cellulose is the most abundant natural polymer on earth, with 1.5×10^{12} tons of total annual biomass production [34]. This natural polymer is a structural component or skeletal material of the cell wall of various plants and some living species such as algae, fungi, bacteria, and tunicates [35]. The most commonly used renewable sources of cellulose are wood pulp with about 35-50% cellulose content [36] and cotton containing about 90% cellulose [37], the highest content of the plants.

Efforts on understanding the structure and morphology of cellulose began in 1838 with its first chemical separation by French chemist Anselme Payen [34]. In 1920s, the pioneering work of Hermann Staudinger recognized the polymeric structure of cellulose [38]. Cellulose is a homo polysaccharide composed of a linear repetition of β-D-gluco-pyranose molecules, which are ring form of the six-member glucose units, also known as anhydroglucopyranose units (AGU). These molecules are connected through β-(1, 4) glycosidic bond where two pyranoses undergo a condensation reaction. Figure 1.5 displays the chemical structure of cellulose, highlighting six-carbon members of AGU and alcohol functional groups. Each polymer chain consists of a non-reducing end with a pendant hydroxyl group (-OH) and a reducing end with a hemiacetal unit. Every other AGU is rotated 180° to its neighbor. These neighbor AGUs are named together as a cellobiose unit, the smallest repeating unit in the cellulose chain. The number of AGU or degree of polymerization in the polymer chain ranges from hundreds to several tens of thousands, depending on the cellulose source [39].

The unique molecular structure of cellulose leads to its diverse properties such as chirality, hydrophilicity, degradability, and chemical tunability. The hydroxyl groups exposed outside the AGU rings also allow cellulose to form hydrogen bond networks by inter-and intramolecular hydrogen bondings. The intermolecular hydrogen bonding allows sheet-

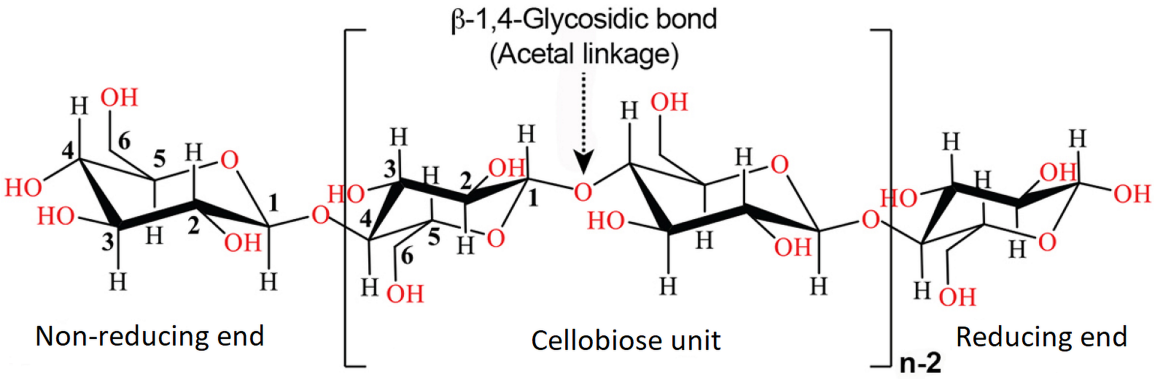

Figure 1.5: Molecular structure of cellulose (n = degree of polymerization) (adapted from Ref. [40] with permission from The Korean Society for Agricultural Machinery).

like structures, whereas intramolecular hydrogen bonding imparts stiffness and strength to cellulose [41]. Because of the hydrogen bonding network, in nature, cellulose does not exist as individual chains, instead found as microfibril bundles of closely packed cellulose chains (Figure 1.6). The bundle of cellulose chains assembles into larger units known as elementary fibrils (∼3 nm in diameter) [42]. The number of cellulose chains were estimated as 36 [42], 24 [43] or 18 [44]. The elementary fibrils assemble into even larger units called microfibrils (20-50 nm in diameter) [45] and these microfibrils are packed into cellulose fibers (3-100 μm in diameter) [45]. Therefore, this hierarchical organization imparts cellulose fiber partially crystalline structure. Its crystallinity can change from 40 to 70%, depending on the cellulose source and extraction method [46]. Cellulose fibers can be broken down employing mechanical or chemical methods to isolate the fibers on the nanoscale. The isolated cellulose particles with at least one dimension measuring 1-100 nm are called nanocellulose [47].

1.4.2 Nanocellulose

Research on nanocellulose over the past decade has exhibited the potential of cellulose for high-performance materials. Compared to molecular and fiber forms of cellulose adapted to industrial products, nanocellulose is a new class of cellulosic material showing inspiring properties for the next generation of renewable products [49]. Nanocellulose has gained

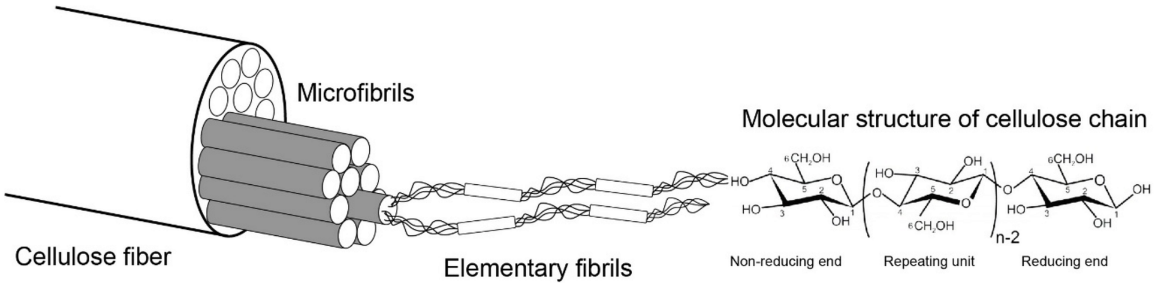

Figure 1.6: Hierarchical organization of cellulose fibers (reproduced from Ref. [48] with permission from BioResources).

increasing interest over the past decade. The number of publications increased approximately 40 times since 2010 (Figure 1.7). Nanocellulose has been studied for various applications, from polymer nanocomposites, flexible displays, and transparent barrier films to food products and biomedical applications [47]. Also, the nanocellulose market is predicted to achieve $\sim$700 million dollars by 2025 [46]. Diverse properties of nanocellulose such as dimensions, remarkable mechanical properties, low density, and chemical tunability have played an essential role in this increasing interest. However, the nanocellulose structure and morphology, and consequently, properties are affected by the processing conditions from macroscale to nanoscale. Based on the type of treatment, two main classes of nanocellulose are: (i) cellulose nanofibrils (CNFs) obtained by mechanical disintegration and (ii) cellulose nanocrystals (CNCs) extracted through a chemical hydrolysis.

The main difference between CNF and CNC is resulting from the partially crystalline nature of cellulose fiber containing both ordered and disordered regions (Figure 1.8). For CNFs, mechanical treatment breaks inter-fibrillated hydrogen bonds (shown in Figure 1.8) and leave the ordered and disordered regions together. On the other hand, CNCs are the ordered regions of cellulose separated through acid hydrolysis. The acid degrades the amorphous regions and leaves the crystals intact. Figure 1.9 shows the electron micrographs of wood cellulose fibers, CNCs and CNFs retrieved from literature [50]. Depending on the source and extraction method, CNF has a width ranging 5-50 nm and a length of several micrometers [48], while CNC has dimensions of 2-20 nm [48] in width and 5-500 nm [50]

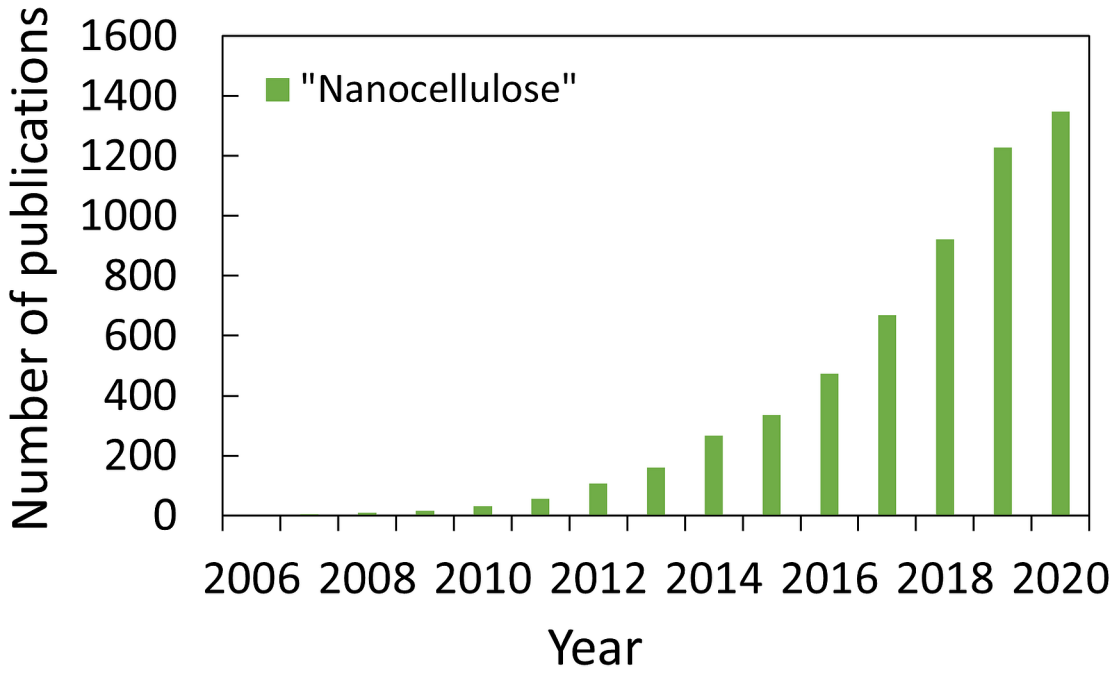

Figure 1.7: Annual number of scientific publications with a topic search using a keyword of "nanocellulose" in Web of Science in April 2021.

in length. The choice of CNC vs. CNF depends on the desired application and properties. CNFs are often entangled due to their high aspect ratio; therefore, they may be suitable for viscosity modification and reinforcing applications. CNCs have a high specific surface area making them ideal for applications such as films and barriers. The following section gives more information about CNCs, which is the focus of this dissertation.

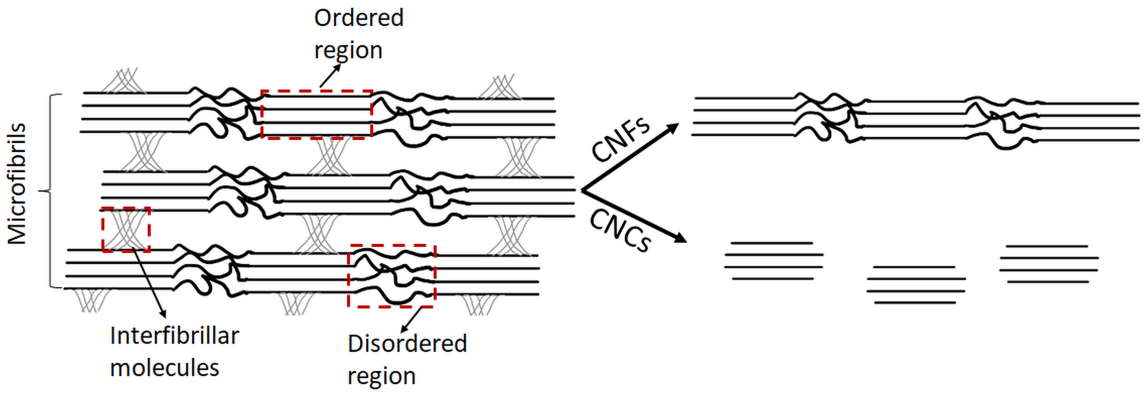

Figure 1.8: The relationship between cellulose fiber and the structures of CNF and CNC.

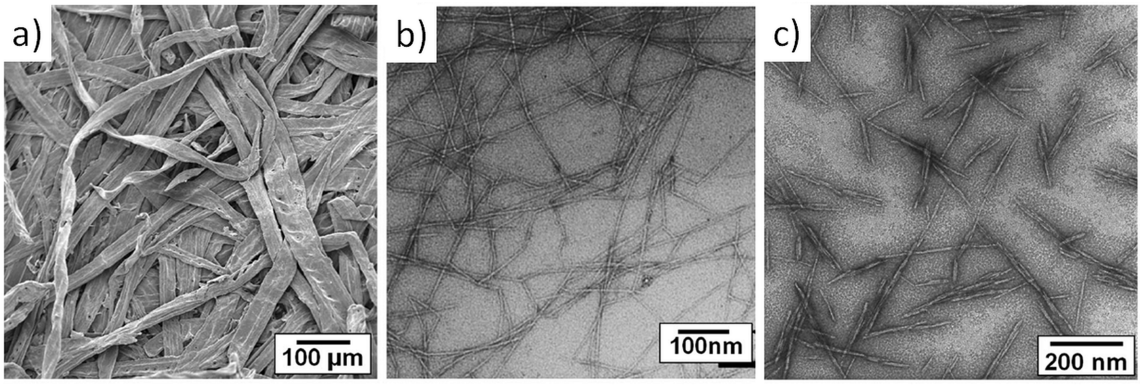

Figure 1.9: Electron micrographs of a) wood cellulose fibers (reproduced from Ref. [50] with permission from The Royal Society of Chemistry), b) CNFs (adapted with permission from Ref. [51] ©American Chemical Society, and c) CNCs (reproduced from Ref. [50] with permission from The Royal Society of Chemistry).

1.4.3 Cellulose nanocrystals (CNCs)

The first report of CNC extraction via acid hydrolysis was reported in 1947 by Nickerson and Habrle [52]. Since then, we learned that the degradation by acid begins with the most accessible parts of the fiber and continues with the reducing end groups and the crystal surfaces [47]. Hydrolysis parameters such as acid concentration, reaction time and temperature should be controlled to preferentially hydrolyze only disordered regions while keeping the ordered regions intact because of their high resistance to acid attack. CNCs are produced along with some by-products such as residual acid and degraded sugars. CNCs are purified through cycles of centrifugation and dialysis. Typically, ultrasonic treatment is performed after the purification to disperse the nanocrystals in water and obtain colloidally stable aqueous CNC suspension [53].

The dimensions and properties of the extracted CNCs heavily depend on the source and hydrolysis method [54]. Table 1.4 lists the length and the cross-section of CNCs obtained from various sources. Cellulose sources vary in their microfibril dimensions and the degree of crystallinity. For example, microfibril dimensions of wood and cotton are smaller than the microfibrils of tunicate, bacterial and algal cellulose, similar to their resulting CNC dimensions [54]. The crystallinity of CNCs relative to cellulose ranges from 54 to 88%

[50]. The hydrolysis parameters such as acid concentration, reaction time and temperature also influence the dimensions of CNCs. Increasing at least one of these parameters makes the acid attack more severe, depolymerizing the crystalline parts in addition to disordered regions and decreasing the dimensions of CNCs [55]. On the other hand, decreasing the severity of the hydrolysis can result in incomplete removal of disordered regions, causing changes in the morphology of CNCs [56].

Table 1.4: The variability in the dimensions of CNCs from different sources (adapted with permission from Ref. [54] ©American Chemical Society).

Cellulose type	Length	Cross-section	References
Wood	100 - 300 nm	3 – 5 nm	[57, 58]
Cotton	200 – 350 nm	5 nm	[58]
Algal (Valonica)	>1000 nm	10 – 20 nm	[59, 60]
Bacterial	100 nm to several μm	5 – 10 by 30 - 50 nm	[61, 62]
Tunicate	100 nm to several μm	10 – 20 nm	[63, 64]

The type of acid also affects the hydrolysis kinetics [65]. While sulfuric acid is the most commonly used acid for hydrolysis, many researchers have studied the alternative routes using mineral acids or organic acids like hydrochloric acid [66], phosphoric acid [67], hydrobromic acid [68], oxalic acid [69], or maleic acid [70]. Hydrolysis with sulfuric acid adds anionic sulfate half ester groups to the CNC surface, typically ranging from 0.6 to 1.1 wt% Sulfur [71]. These anionic sulfate groups help CNCs to be colloidally stable in water. Electrostatic repulsion between surface charges of nanocrystals is the main driving force for the dispersibility of CNCs in water [72]. When hydrochloric and hydrobromic acids are used, no charge is added to the CNC surface, resulting in large aggregates in water [65]. Phosphoric acid imparts phosphate half ester groups to the CNC surface; however, these groups are not enough to provide good colloidal stability. Oxalic acid and maleic acid result in highly stable aqueous dispersion of CNCs but their yields are low [65].

Mechanical properties of cellulose nanocrystals

CNCs are stiff rod-shaped nanoparticles and exhibit high strength and modulus, characteristics that originate from hydrogen bonding between hydroxyl groups of AGU in the crystalline regions of cellulose. Axial elastic modulus (E_A) of crystalline regions within cellulose (110-220 GPa) is superior than Kevlar (124-130 GPa) and within the range of moduli of other reinforcement material such as steel wire (210 GPa) and carbon fiber (150-500 GPa) [50]. We should note the influence of the extraction process on the elastic modulus of CNCs; however, direct measurement of the modulus of a single CNC is rare. Rusli et al. [73] performed a direct measurement on the CNCs extracted from cotton with Raman spectroscopy and calculated the E_A as 57 GPa and 105 GPa by assuming CNCs in a 2D or 3D network, respectively. Šturcová et al. [74] also used a similar technique on tunicate CNCs and calculated the E_A as 143 GPa.

In the last decade, a significant research effort has been given to use of CNCs as a barrier film and a reinforcement element in polymer composites. Mechanical property is a strong function of the CNC network within the material; therefore, the structure-mechanical properties relation in neat CNC films and CNC-reinforced polymer matrix has been of interest. Overall, CNC-CNC or CNC-polymer network can change based on the CNCs' dimensions, surface chemistry, and moisture content. A neat CNC film is held together by hydrogen bonding of interconnected CNC network; therefore, mechanical properties of neat CNC films are mainly affected by the porosity in the films due to the gaps within the CNC network. In the mechanical properties of CNC reinforced polymer composites, the degree of CNC dispersion/aggregation in the polymer matrix largely contributes to changes in the mechanical properties of the reinforced polymer.

Surface modification of cellulose nanocrystals

Surface hydroxyl groups of CNCs allow for various modifications at their surface due to high donor reactivity of the alcohol groups. Surface modifications are mainly performed

to impart new functionalities to CNCs, facilitate the addition of CNCs into hydrophobic media (e.g., polymer resins), or improve the dispersion of CNCs in organic solvents. The surface chemistry can be tuned through non-covalent surface modifications or covalent surface modifications, including small molecule attachment and polymer grafting.

Non-covalent surface modifications are primarily carried out via electrostatic adsorption of surfactants, polyelectrolytes, or oppositely charged groups (relative to the surface charge of CNCs) [75]. The adsorption mechanism can be hydrophilic affinity or hydrogen bonding in addition to electrostatic interactions [75]. Several researchers [76–78] have modified the negatively charged surface of CNCs with cationic surfactants by taking advantage of electrostatic attraction.

Covalent surface modifications are achieved by covalently attaching small molecules or polymers to the nanoparticle surface. Hydroxyl groups at the surface can be reacted with different functional groups. Figure 1.10 shows the common chemistries for covalent surface modifications of CNCs. Small molecules can be attached to the CNC surface with numerous approaches: oxidation [79, 80], etherification [81], esterification [82, 83], silylation [84], urethanization [85]. Alternatively, polymers can be grafted to the CNC surface. Three main approaches to graft polymers on CNC surfaces are *grafting to*, *grafting from*, and *grafting through* (Figure 1.11). Pre-synthesized polymer is attached to the CNC surface in *grafting to* whereas polymers grow from the surface of CNCs in *grafting from*. *Grafting through* is an intermediate approach between *grafting to* and *grafting from* because polymerization occurs both in the solution media and on the surface of CNCs.

In *grafting to*, using pre-synthesized polymers allows characterization of the attached polymer before grafting reaction; however, it limits the polymer density on the CNC surface (grafting density) due to steric hindrance. On the contrary, high grafting densities can be obtained in *grafting from* approach since monomers are stepwise added to the immobilized initiator on the CNC surface. However, challenging polymerization kinetics and difficulty in the characterization of the attached polymer are drawbacks of *grafting*

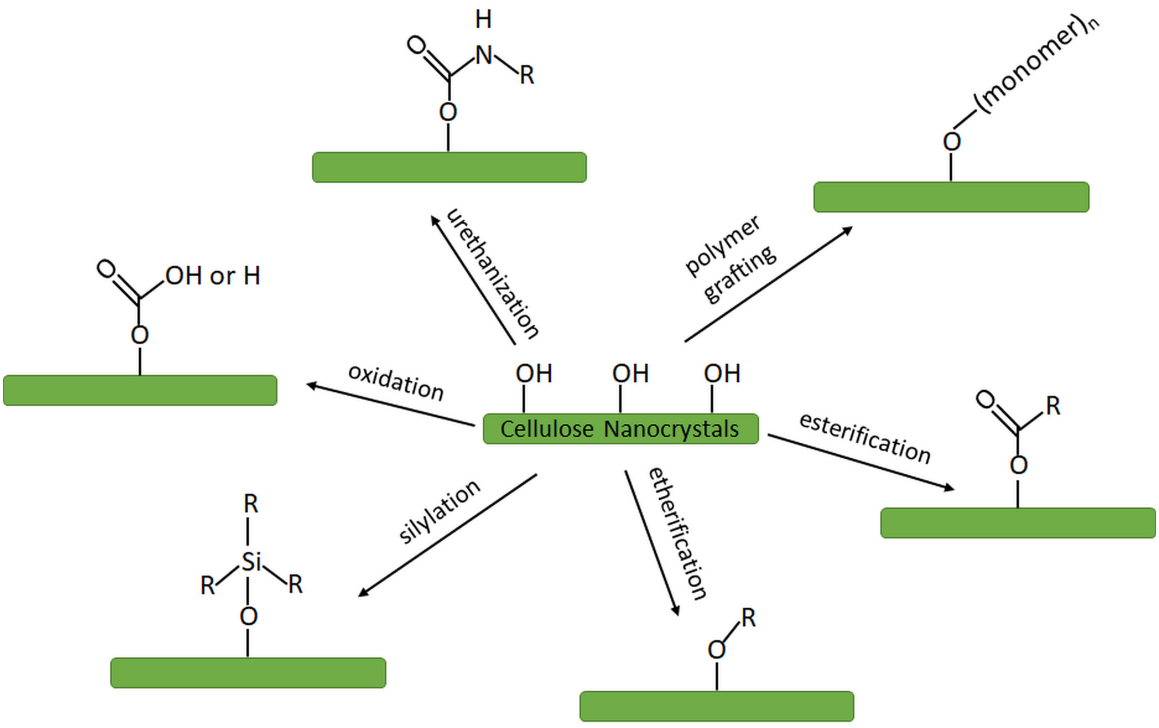

Figure 1.10: Schematic showing the common surface modification chemistries for CNCs.

from approach [86]. *Grafting through* is based on conducting solution polymerization in the presence of the modified surface of CNCs. *Grafting through* method, also known as macromonomer method, requires attachment of vinyl groups first to the CNC surface to prepare a macromonomer. Then, monomers or growing chains in the solution can react with the vinyl groups on the CNC surface. Polymer characterization is challenging as in *grafting from*; however, less steric hindrance occurs compared to *grafting to* approach [87].

Characterization of cellulose nanocrystals

Characterizations of the surface chemistry, morphology, purity and crystallinity of CNCs are vital to advance their utilization. The physical and chemical properties of CNCs can be characterized by using CNCs either dried or dispersed in water. Using dynamic light scattering technique and measuring zeta potential of aqueous CNC dispersions can give an idea about the size and charge of CNCs. In the dried state, the size and morphology of CNCs are

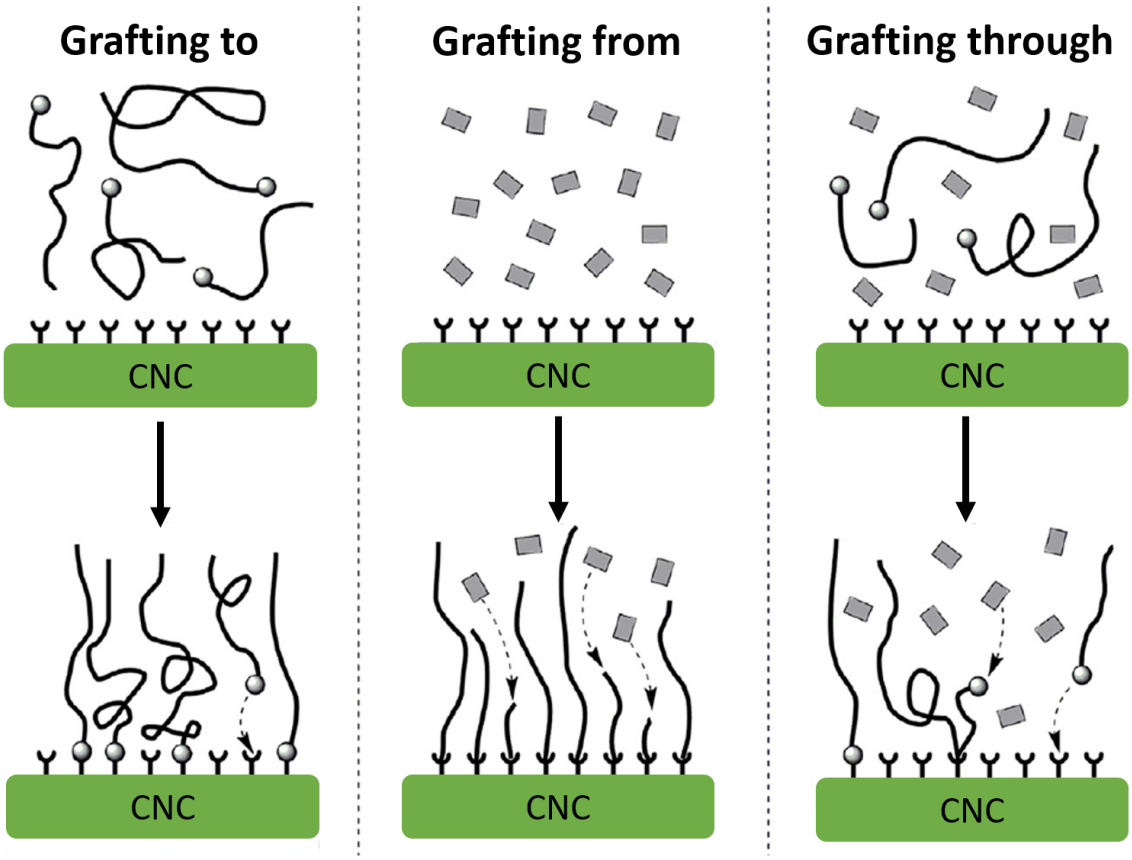

Figure 1.11: Schematic of three main polymer grafting approaches: *grafting to*, *grafting from*, and *grafting through*.

commonly analyzed by using atomic force microscopy (AFM) and transmission electron microscopy (TEM). Elemental composition can be determined via elemental analysis and X-ray photoelectron spectroscopy (XPS). The chemistry of CNCs can be characterized by using Fourier transform infrared spectroscopy (FTIR) or solid state nuclear magnetic resonance (NMR). Water contact angle measurement on the dried material or dispersion test in various solvents is used to evaluate the hydrophilicity/hydrophobicity of the CNCs. Thermogravimetric analysis (TGA) is a common technique to understand the thermal stability of CNCs. Crystallinity of CNCs is determined by using X-ray diffraction (XRD). The characterization techniques followed in this work are explained in detail in the characterization sections of each main chapter.

1.5 Motivation

The *film formation dilemma* in waterborne coatings (section 1.2.2) was the driving force for the studies presented in this dissertation. Producing hard latex film with zero VOC emission is currently a significant challenge in the coating industry. Zero-VOC coatings can be prepared by using a polymer or composition of polymers with low T_g to facilitate film formation at ambient temperature. However, these polymer films underperform compared to benchmark coatings. In this research, the incorporation of CNCs was explored as an approach to improve the mechanical properties of ambient-film-forming waterborne latex films. As an additive to acrylic latex particles, CNCs could be placed in either the aqueous phase or the polymer phase. This dissertation aims to determine optimal methods of CNC addition to waterborne acrylic latexes, to identify the challenges in controlling the CNC location in the latex system, and to characterize film formation and properties of final dried films.

1.6 Dissertation overview

The main objectives of this dissertation are to understand mechanisms controlling the location of CNCs with respect to acrylic latex particles in waterborne systems, and to investigate the effect of CNC location on the film formation and mechanical properties of the latex film. The specific objectives are as follows:

1. Incorporate CNCs into the aqueous phase of latex

   a) Obtain latex particles modified with carboxylic groups

   b) Develop a blending protocol and investigate film formation

   c) Characterize the nanocomposite films for mechanical, thermal, and optical properties

2. Develop a surface modification framework for obtaining macromonomer CNCs

   a) Verify the urethanization chemistry on the CNC surface by using isocyanatoethyl

methacrylate molecules

b) Investigate the effect of reaction conditions on the crystallinity and morphology of CNCs

c) Demonstrate the copolymerization ability of modified CNC (mCNC) as a macromonomer

d) Evaluate the dispersion performance of functionalized CNCs in the acrylic polymer matrix compared to unmodified CNCs (umCNCs)

3. Incorporate functionalized CNCs into the polymer phase of latex via miniemulsion polymerization

   a) Prepare acryloyl-modified (mCNC) and acrylic polymer-grafted CNCs (gmCNC) for compatibilization with acrylic monomers

   b) Evaluate the preference of functionalized CNCs to aqueous or monomer phases of miniemulsion relative to umCNC

   c) Develop a synthesis procedure to control the size of latex particles in the miniemulsion of neat acrylic monomers

   d) Synthesize latexes by using functionalized CNCs and umCNC in the monomer phase of the miniemulsion

   e) Investigate the particle morphology in the latexes and mechanical properties of the resulting latex films

For these objectives, three major studies (Figure 1.12) were conducted and presented as three main chapters (Chapter 2, Chapter 3, and Chapter 4) parallel to the specific objectives above. Chapter 2 investigates the addition of CNCs to the aqueous phase of acrylic latex. The content of Chapter 2 has been published in *Progress in Organic Coatings* [88]. Chapter 3 demonstrates a framework to functionalize the CNC surface with acryloyl groups and acrylic polymers. Chapter 4 explores the incorporation of functionalized CNCs into the polymer phase of latex via miniemulsion polymerization. Chapter 5 summarizes the major findings from this dissertation and provides recommendations for future work.

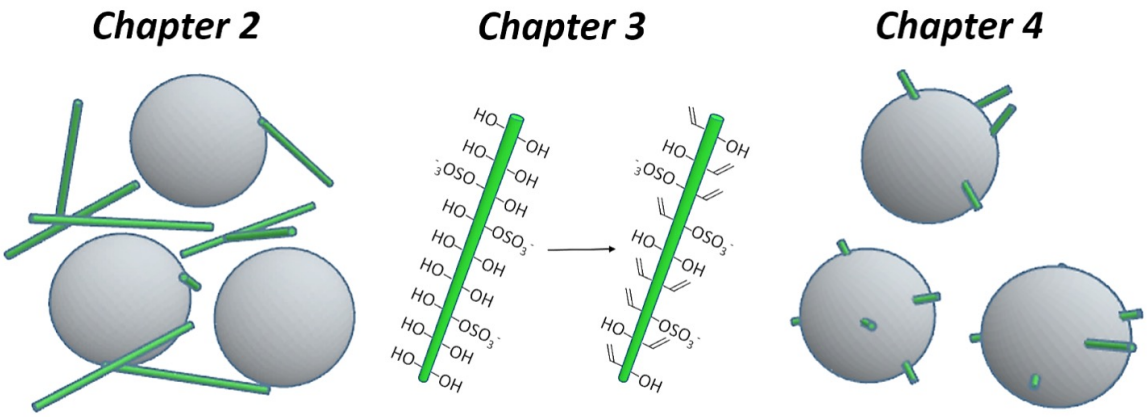

Figure 1.12: Schematic showing the specific objectives/main chapters of the dissertation.

CHAPTER 2

ENABLING ZERO ADDED-COALESCENT WATERBORNE ACRYLIC COATINGS WITH CELLULOSE NANOCRYSTALS

This chapter investigates the addition of CNCs to the aqueous phase of acrylic latex (Figure 2.1). Film formation and properties of nanocomposite latexes were examined. This chapter and Appendix A are adapted from a published article. Reprinted by permission from Elsevier: Dogan-Guner, E. M.; Brownell, S.; Schueneman, G. T.; Shofner, M. L.; Meredith, J. C., Enabling zero added-coalescent waterborne acrylic coatings with cellulose nanocrystals. Progress in Organic Coatings 2021, 150, 105969, https://doi.org/10.1016/j.porgcoat.2020.105969.

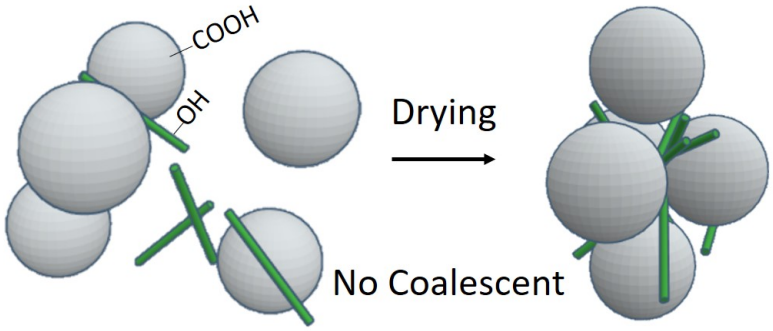

Figure 2.1: Schematic showing latex particles and CNCs in the aqueous phase during film formation.

2.1 Introduction

Paints and coatings with a market of ∼43 million tons in 2016 [6], have annual volatile organic compound (VOC) emissions of ∼2 million tons [19]. Reducing VOC release has driven development of waterborne paints, but despite advances many interior waterborne products contain 250 g/L VOCs [89]. In addition to inherent health effects [20], VOCs react with atmospheric nitrogen oxides, forming ground-level ozone [90] that contributes to

global warming and harms health [91]. Coating producers are under increasing pressure to decrease VOC content because of legislation and customer demand. However, transitioning to low VOC products brings a challenge known as the *film formation dilemma*, in which the VOC organic coalescents are needed to plasticize individual latex particles so that they form hard, durable coatings following VOC evaporation. Acrylics are the most used binder resin in waterborne coatings. Hardness of the acrylic is an important aspect of coating durability. Soft latex particles that easily coalesce to form a film lack adequate hardness. Latexes are often formulated with copolymers with high glass transition temperature (T_g) but VOC coalescents are added to temporarily plasticize the particles to enable film formation at ambient conditions [18]. Industry also employs non-evaporative plasticizers that provide coalescence. However, the film remains tacky after curing. Thus, alternative approaches are desired to achieve the performance of high T_g acrylic latex coatings in the lower VOC formulations of today.

One approach is to add a hardening filler to the polymer matrix. Mechanically robust nanoscale fillers have been shown to improve polymer mechanical performance [92], including nanoscale fillers such as clay [93], silica [94], and carbon nanotubes [95]. Cellulose nanocrystals (CNCs) are proposed as a renewable filler to enhance mechanical performance of soft latex films, due to their high crystallinity, strength, and modulus, low density (relative to mineral fillers), and optical transparency (when dispersed adequately or matched to the matrix refractive index) [49, 50, 96]. In contrast to mineral or synthetic based fillers mentioned above, CNCs are plant-based, highly ordered rod-shaped particles with high elastic moduli in the range of 100-150 GPa [97]. Due to anionic sulfate half-ester surface groups, these CNCs form a charge-stabilized dispersion in water. As a result, they can be readily added to waterborne polymers as a reinforcing filler [98, 99]. Indeed researchers [100–102] have observed improved coating hardness by blending CNC dispersions with acrylic latexes, but unfortunately these studies used VOCs or otherwise did not quantify VOC content. Abitbol et al. [100] and Pu et al. [101] used a commercial latex containing

approximately 10 wt% coalescent and 100 g/L VOC, respectively.

We report a simple method of adding unmodified CNCs to enhance the mechanical performance of ambient film-forming acrylic coatings that have zero added coalescent. Compared to in situ polymerization with CNCs, this approach does not require surface functionalization or copolymerization with CNCs. VOC content of the latex used in this work was measured to be ∼0.64 g/L (Table A.1), whereas the threshold VOC limits are 50 g/L for low-VOC and 5 g/L for zero-VOC labeled paints. In addition to the use of an ambient film-forming binder with zero added coalescent, a difference relative to previous work is the use of latexes containing methacrylic acid (MAA) to introduce carboxylic functional groups that promote interactions with CNCs. Wood-derived CNCs were blended into these latexes at different loadings. We characterized the resulting acrylic latex/CNC films to determine the film formation, the morphology of CNCs in the latex matrix, and mechanical performance in order to demonstrate that CNCs enable zero VOC binder formulations with mechanical performance similar to VOC-containing hard acrylics.

2.2 Experimental section

2.2.1 Materials

Aqueous CNC dispersion

An aqueous CNC dispersion (5.5 wt%, Na^+ form, USDA Forest Service Forest Products Laboratory, Madison, WI) was used as received. The dispersion was prepared from mixed southern yellow pine dissolving pulp via 64% sulfuric acid digestion, described elsewhere [54]. The CNCs had 0.86 wt% sulfur (dry basis) due to sulfate half-ester groups from the hydrolysis.

Waterborne acrylic latex formulations

Two well-characterized coalescent-free latexes with a solid content of 39.4 wt% were provided by Dow Chemical. These latexes were prepared by emulsion polymerization of butyl acrylate (BA), methyl methacrylate (MMA), and MAA. The monomers were emulsified with sodium lauryl sulfate (SLS) and polymerized with thermally-initiated ammonium persulfate at 87 °C for 120 min. The pH was adjusted to 7.0 – 8.0 with dilute ammonium hydroxide to provide long term colloidal stability. Additional details are provided in Appendix A (Table A.2). The two latexes are denoted as MAA5 and MAA10, corresponding to MAA content. MAA5 contained 60% BA, 35% MMA, and 5% MAA. MAA10 contained 65% BA, 25% MMA, and 10% MAA. MAA assists electrostatic stabilization of polymer particles. The higher MAA fraction makes the polymer particles more hydrophilic due to -COOH functional groups, with a goal of promoting compatibility with CNCs. Carboxylic acid co-monomers were previously found to increase shear strength of acrylic latex films due to intermolecular dipole-dipole interactions of acid groups [103, 104]. Hydrogen bonding between carboxylic acid groups with hydroxyl groups on CNCs was also demonstrated [105, 106].

2.2.2 Preparation of composite films

Acrylic latex/CNC composites were prepared by post-synthesis blending. Figure 2.2 shows a schematic representation of physical blending and a composite film. The aqueous CNC dispersion (5.5 wt%) was blended into the MAA5 and MAA10 latexes. Different amounts of CNC dispersion (0-18.9 g) were added to 15 g of base latex to change the CNC loading (0-15 wt%) in the dry films. Additional information is provided in Table A.3. The resulting mixture was vortexed for 1 min (IKA Vortex3). Vortex method resulted in better dispersion compared to use of magnetic stirrer (Figure 2.3). A mixing time of 1 minute was sufficient to obtain a homogeneous dispersion of CNCs in the latexes. The latex samples were cast on 0.25 cm thick glass substrates (10 cm $\times$ 10 cm) with a Gardco drawdown plate and an

Elcometer 3540 film applicator to obtain 300 μm thick wet coatings. Coatings were dried overnight resulting in dry films with thicknesses ranging from 90 to 180 μm depending on the solid content (Table A.3).

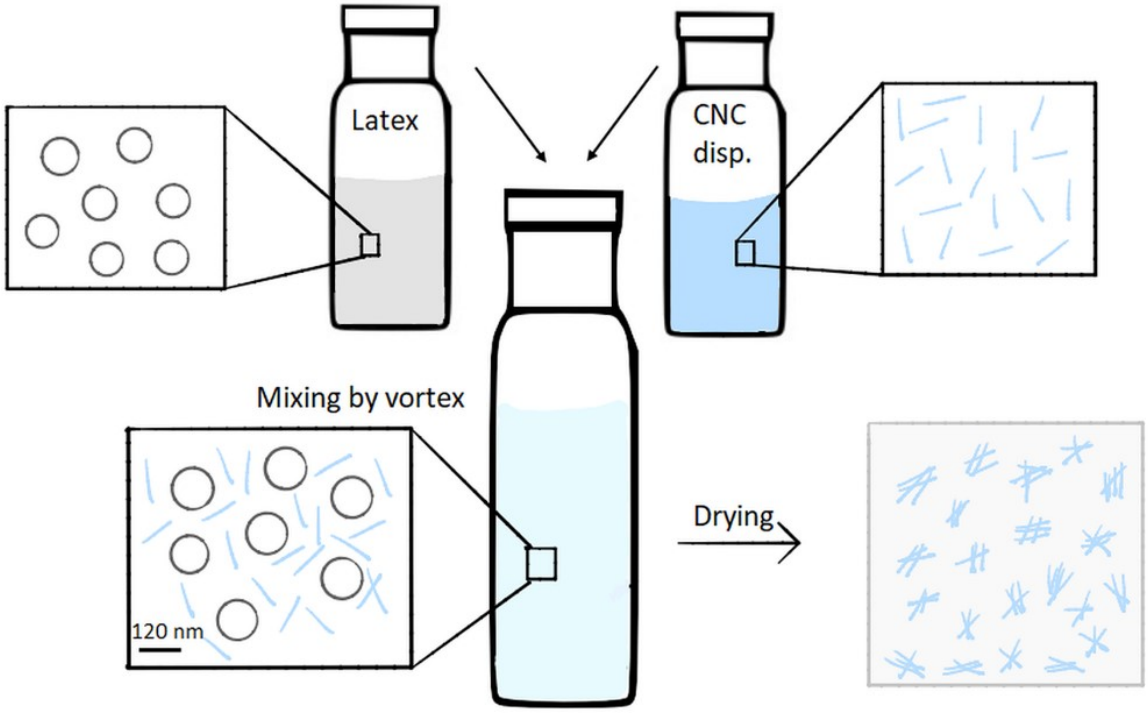

Figure 2.2: Schematic representation of the blending process and the composite film.

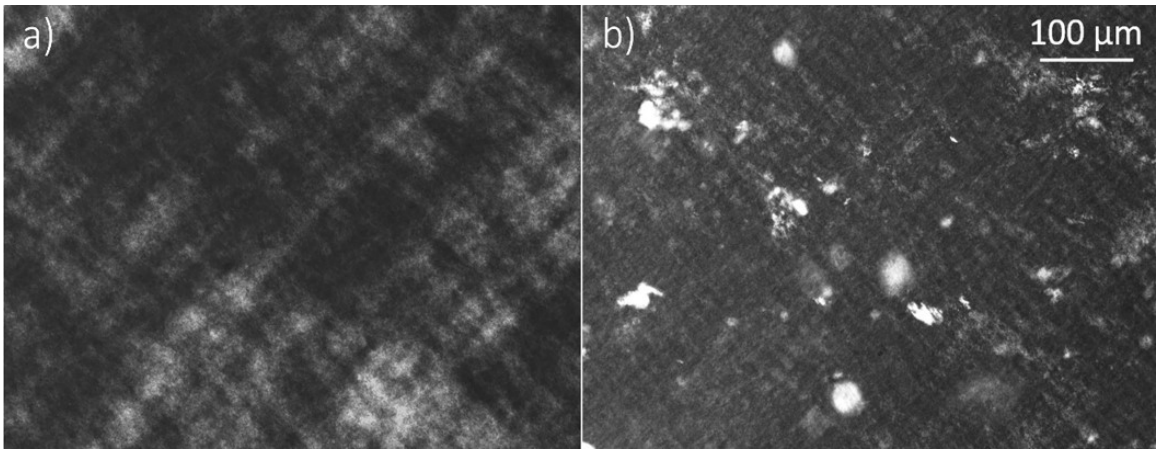

Figure 2.3: Polarized light microscope images of 5 wt% CNC loaded MAA5 films prepared by using a) vortex for 1 min and b) magnetic stirrer for 2 h at 400 rpm.

2.2.3 Characterization of CNC dispersion and latexes

A Bruker Icon atomic force microscopy (AFM) instrument was used to image individual CNCs. The CNC/water dispersion was diluted with DI water to 0.001 wt% and blade-coated onto a cleaned silicon wafer. Images were analyzed by using Gwyddion software to obtain length and height for individual CNCs. 50 isolated particles were measured from 10 different AFM topography images. The cross section of CNCs was taken as the height at the center of its length to avoid tip-broadening effects.

A Malvern Zetasizer Nano ZS90 was used to measure the zeta potential and average particle size of the CNC dispersion and latexes. For particle size distribution, the CNC/water dispersion was used as received and latexes were diluted with DI water to 0.025 wt%. From three measurements, the z-average intensity-weighed mean diameter of particles was determined. Average zeta-potential was determined from three measurements on 10 μl CNC dispersion and latexes diluted with 2 ml DI water.

A Mettler Toledo Seven2Go pH/mV meter was used to measure the pH of CNC dispersion and latexes.

2.2.4 Characterization of CNC and latex films

A silicon cantilever with rotated tip (8 nm radius) was used in an AFM (Veeco, Dimension 3100) to study dry film surface topography. The AFM probe had a nominal spring constant and frequency of 1.6-6 N/m and 50-100 kHz, respectively. Height and amplitude images were captured with tapping mode in air. Roughness values (rms) were determined on 500 nm $\times$ 500 nm square areas.

T_g values of neat and 15 wt% CNC films were measured by differential scanning calorimetry (DSC - TA Instruments, DSC Discovery). Samples were equilibrated at -50 °C and heated to 150 °C under nitrogen at 10 °C/min. The midpoint T_g was measured to capture the as-processed structure.

Minimum film formation temperatures (MFFTs) of all composite films were measured

visually based on the change in optical clarity upon film formation, over a temperature range from -5 to 13 °C in desiccated air.

The water content of latex films was evaluated with thermogravimetric analysis (TGA - TA Instruments, Q5000). Neat, 5 wt% and 15 wt% CNC samples were heated from room temperature to 400 °C at 10 °C/min.

CNC composition in the films was evaluated with Attenuated total reflection Fourier transform infrared (ATR-FTIR) spectroscopy (Nicolet iS50 with diamond ATR crystal). The scan range was 4000 cm^{-1} – 600 cm^{-1} with a resolution of 4 cm^{-1} and a total of 64 scans. Two randomly-chosen locations were scanned on the films for each composition and we found no difference (paired t-test with α=0.05) between spectra at these locations. The spectra were normalized at the 1725 cm^{-1} peak associated with carbonyl groups in acrylic polymers.

Polarized light microscopy (PLM) was used to assess the dispersion of CNC in acrylic films by observing birefringence in transmission under crossed polarizer and analyzer (Olympus BX51).

The cross-sections of the films were characterized using field emission scanning electron microscopy (FE-SEM - Zeiss Ultra60). Latex films were cryo-fractured by immersing in liquid nitrogen, and surfaces were sputter-coated with gold and imaged at 3 kV.

Optical transparency of the films was assessed by light transmission over wavelengths of 200-800 nm with a UV-Vis spectrometer (Shimadzu UV-1800). Transmittance values were normalized to a film thickness of 100 μm by using the Beer-Lambert law.

A high-throughput mechanical characterization (HTMECH) instrument [107] was used to deform films biaxially with a 1.25 mm diameter hemispherical indenter normal to the film plane at a speed of 10 mm/s. The average ultimate tensile strength (UTS) and strain at break were reported from five stress-strain curves per sample.

Uniaxial tensile testing was performed (Instron 5566) to obtain modulus, by using crosshead displacement data, for relative comparison among samples. Three films pre-

pared by using a *dog bone* cutting die for the ASTM D-1708 geometry were tested for each composite composition at lab conditions (approximately 20 °C and 26% relative humidity) with a strain rate of 10 mm/min.

A Hysitron TriboIndenter equipped with a Berkovich diamond indenter was used in a load-controlled mode to indent neat and CNC loaded latex films at room temperature at loads between 200-500 μN with 100 μN increments. A polycarbonate reference was used to determine the area function of the indenter tip. A triangle load function was used with constant indentation time. Four indentations were performed on each film.

Pencil hardness was measured with an Elcometer 501 test kit by ASTM D3363. The reported hardness is the hardest pencil grade that does not cut the coating at 45°, based on testing each film twice.

Koenig hardness was measured on the first and seventh day of drying for coatings cast on aluminum Q panels by using a TQC pendulum tester (Model SP0500). The average measurement from three spots on the panels is reported.

2.3 Results and discussion

2.3.1 Characterization of CNC dispersion and composite latexes

The hydrodynamic diameter of CNCs in the dispersion was measured as 114 $\pm$ 2 nm by DLS. For rod-shaped CNC particles, DLS provides an apparent size assuming spherical geometry of the particle [108]. The average length and cross section of individual CNCs were measured from AFM imaging (Figure 2.4) as 135 $\pm$ 13 nm and 6 $\pm$ 1 nm, respectively, leading to an aspect ratio estimated as 22. The dimensions and the aspect ratio are similar to those previously reported [71, 99].

As expected, the hydrodynamic diameter of the CNCs is smaller compared to the length obtained from AFM imaging. The apparent particle size of CNCs measured by DLS is only used to show the relative changes in the particle size or state of dispersion [109]. The apparent size of CNCs in this work is larger than previously reported apparent size of CNCs

(same source) [71], indicating that some CNCs formed aggregates in water.

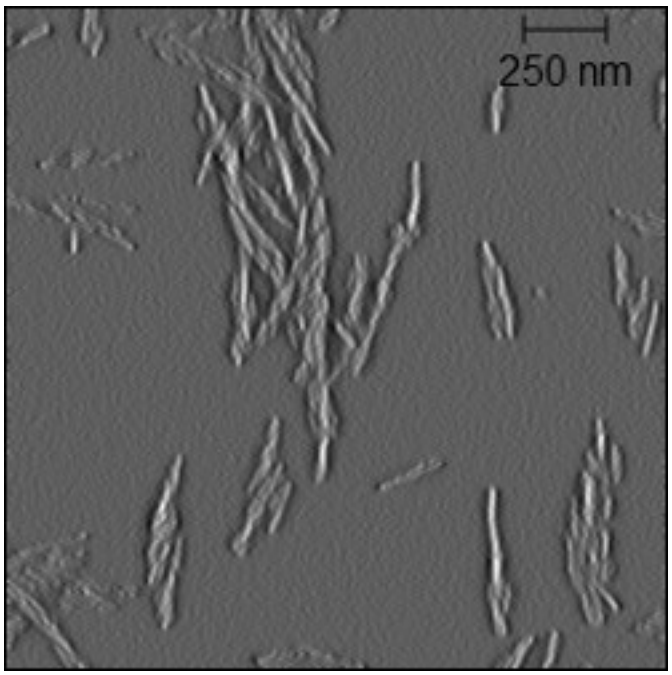

Figure 2.4: AFM image of wood-derived CNCs.

Figure 2.5 shows latex/CNC mixtures (MAA5 post-blends for 0-5 wt% CNC loadings). The pH, average particle size, and zeta potential of the CNC dispersion, neat latexes, and latex/CNC blends are provided in Table A.4. The pH of the latexes remained the same after the addition of the CNC dispersion. Latex dispersions remained stable after addition of CNCs in all cases (Table A.4). The particle sizes of neat MAA5 and MAA10 latexes measured by DLS were similar, 117 $\pm$ 2 nm and 116 $\pm$ 1 nm, respectively. The addition of CNCs had a negligible impact on latex particle sizes, suggesting that CNCs do not aggregate on latex particles in suspension, consistent with their electrostatic charge. The zeta potential of the aqueous CNC dispersion (5.5 wt%) was measured to be -47 mV, due to anionic sulfate half-ester groups, indicating electrostatic stability similar to a previous study [71]. The zeta potentials of MAA5 and MAA10 latexes were measured to be -44 mV and -47 mV, respectively, attributed to the anionic surfactant (SLS) and MAA on the particle surface.

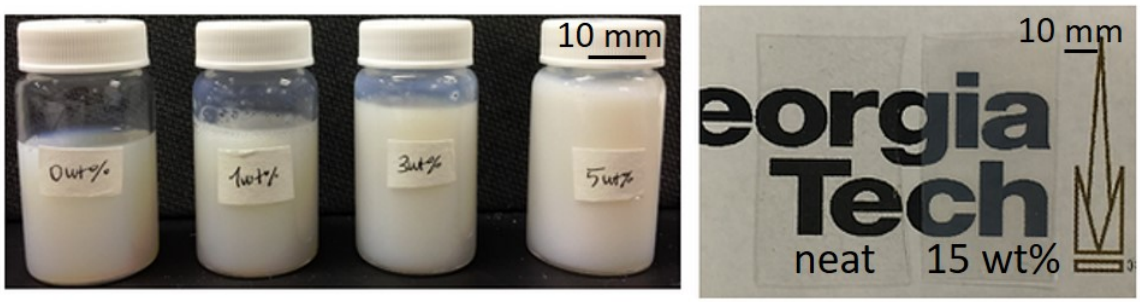

Figure 2.5: Photographic images of CNC-MAA5 latex post-blending (left) and dried films of neat MAA10 and 15 wt% MAA10/CNC composite (right).

2.3.2 Acrylic latex/CNC composite film formation

Figure 2.5 shows films prepared from MAA10 latex, indicating that the CNCs did not impede film formation. The CNC-loaded films were visually similar to the neat films. The values of T_g for MAA5 and MAA10 latexes were measured with DSC to be -7 °C (MAA5) and -11 °C (MAA10). Figure A.1 displays the portion of DSC heating curves highlighting the heat flow change due to the T_g. The addition of CNCs did not affect the T_g of the films in these experiments. Additionally, all composites resulted in MFFT of approximately 0 $\pm$ 0.4 °C.

The dispersion of CNCs in latex films was evaluated with PLM images, shown in Figure 2.6 for neat and CNC-loaded MAA5 films. No birefringence was observed in the neat MAA5 film. The interaction of polarized light with CNCs resulted in birefringent domains of a size range suggesting CNC aggregation. Birefringence in the CNC loaded films was homogeneous and had low intensity, indicating that CNC aggregates are well-distributed in the water phase of the latex. The birefringent domains spread out and brighten with increasing CNC loadings, as expected. Similar results were observed for MAA10/CNC latex composite films (Figure 2.7).

PLM also gives information about whether a film is isotropic or anisotropic. Maltese cross patterns (Figure A.2) were observed in both MAA5 and MAA10 composite films containing CNC loadings of 3-15 wt%. The maltese cross pattern indicates CNCs located

between coalesced acrylic particles forming a spherical symmetry [110] following drying.

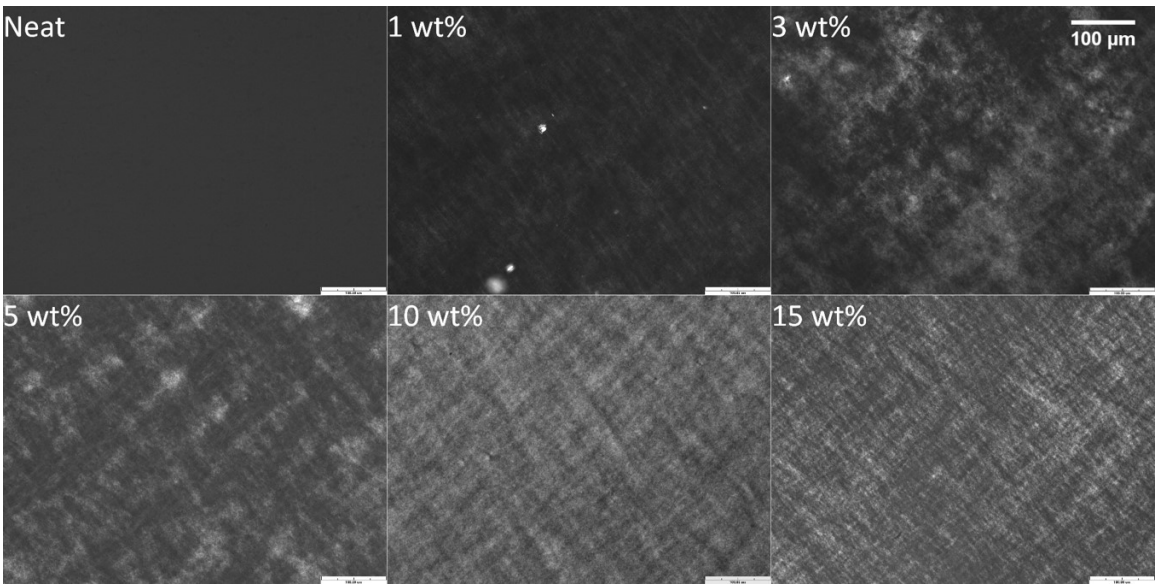

Figure 2.6: Polarized light microscope images of MAA5 and MAA5/CNC composites. The scale bar is 100 μm in all images.

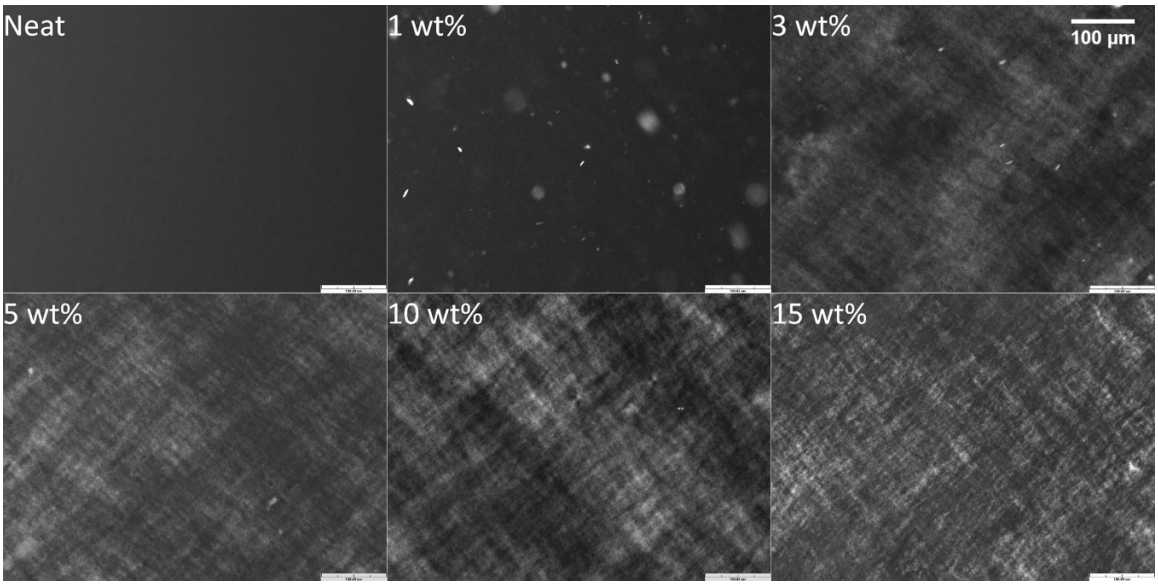

Figure 2.7: Polarized light microscope images of MAA10 and MAA10/CNC composites.

AFM amplitude images are given in Figure 2.8. All film surfaces were relatively smooth with rms roughness less than 10 nm (Table 2.1). The addition of CNC in each latex type increased the coating roughness by a statistically significant amount based on one-way

ANOVA and t-tests (α=0.05). MAA10/CNC films have slightly higher surface roughness than MAA5/CNC films.

Table 2.1: Average roughness (nm) of latex/CNC composite films.

CNC loading (wt%)	Roughness (nm)	
	MAA5	MAA10
0	1.8 ± 0.6	1.9 ± 0.3
5	2.8 ± 0.3	3.5 ± 0.5
15	3.4 ± 0.3	4.5 ± 0.5

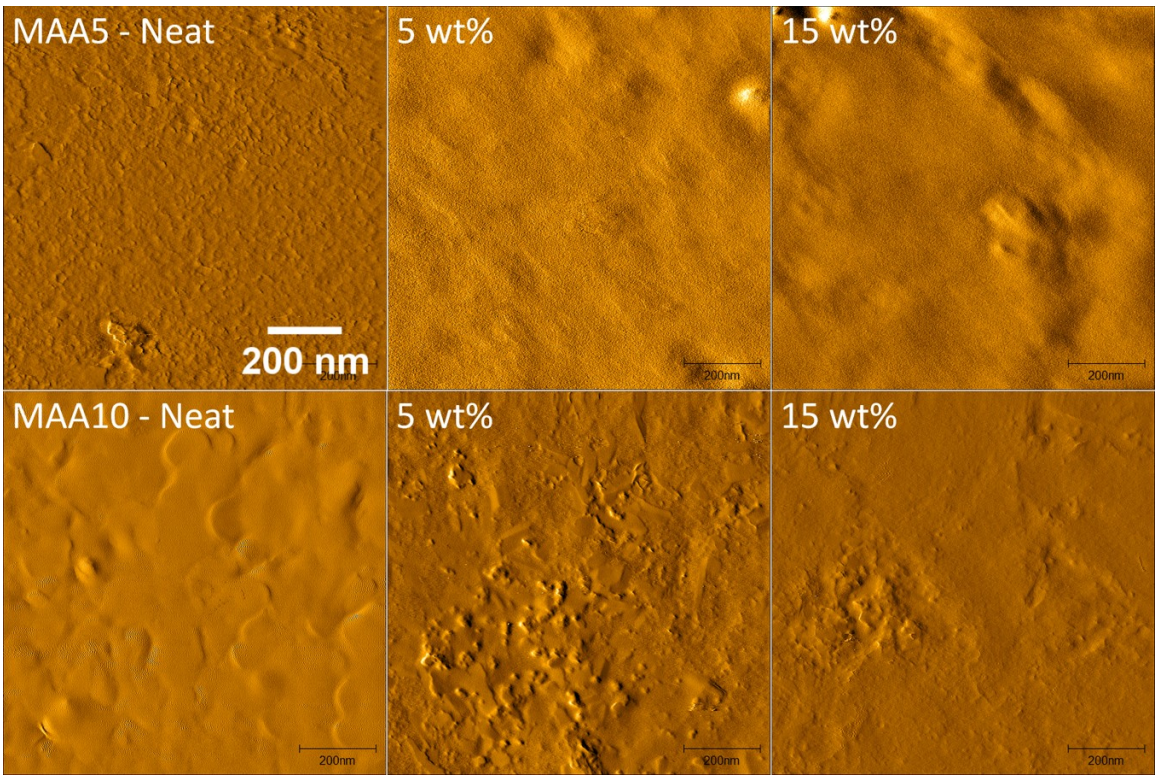

Figure 2.8: AFM amplitude images of neat latex and their CNC-loaded composites: MAA5 (top) and MAA10 (bottom). Scale bar is 200 nm in all images.

The film top surfaces did not show features related to CNC size and shape, suggesting that CNCs were located in the coating bulk. Similar behavior was reported for CNC/styrene-acrylic latex copolymer composites [100]. The negatively charged acrylic particles are unlikely to have CNCs on their surfaces because of electrostatic repulsion. During latex particle coalescence, CNCs are likely to become trapped in interstices between particles,

hindering their migration to the top film surface. Limousin et al. [111] investigated the film formation of CNC/cationic acrylic latex dispersions. Because CNCs electrostatically attached to cationically-modified acrylic particles, CNCs were observed on the surface of coatings in AFM imaging.

SEM was used to confirm the location of the CNCs in the coating cross-section. Similar to the AFM imaging, no features were observed on the top surface of composite films. However, CNCs were embedded in the acrylic matrix in the cryo-fractured cross-sections (Figure 2.9). Small white regions are attributed to aggregates of rod-shaped CNCs since these regions do not exist in the fractured surface of neat latex films. Similar morphology was reported in composites of CNCs with various polymers [112–114]. During the drying and coalescence of acrylic particles, CNCs are confined to interstitial regions, where they concentrate as water evaporates. CNC-CNC aggregation is to be expected because CNCs are forced into close contact as water evaporates and latex coalesces. Compression of the CNC dispersion between latex particles during drying enhances the van der Waals forces and hydrogen bonding between CNCs and causes aggregation in the latex films. The hydrogen bonding between the CNCs and carboxyl groups on the surface of latex particles is also part of the aggregation process. CNCs incorporated into soft hydrophobic styrene butadiene rubber matrices showed a similar microstructure [115] with physically connected CNCs in interstitial space between latex particles.

The diameters of the white regions were measured from SEM to be 47 $\pm$ 21 nm and 43 $\pm$ 16 nm for 5 wt% CNC loaded MAA5 and MAA10 composites, respectively. CNC-loaded MAA5 films with 15 wt% CNC had aggregates having a diameter of 37 $\pm$ 14 nm whereas 15 wt% CNC-loaded MAA10 films had aggregates with 48 $\pm$ 17 nm diameter. The aggregate size did not change significantly with the addition of CNCs; however, the density of the aggregates increased with increasing CNC content. The distance between 100 randomly selected CNC aggregates was measured from SEM images. Aggregates in MAA5 composite films were 403 $\pm$ 72 nm and 236 $\pm$ 122 nm far away from each other for

5 wt% and 15 wt% CNC loadings, respectively. In MAA10 the distance between aggregates was 425 $\pm$ 166 nm with 5 wt% CNC and it dropped to 233 $\pm$ 82 nm with 15 wt% CNC. Not every gap between acrylic particles had CNC confinement, which has been observed in aggregates observed in other CNC-loaded BA/MMA latex films [102].

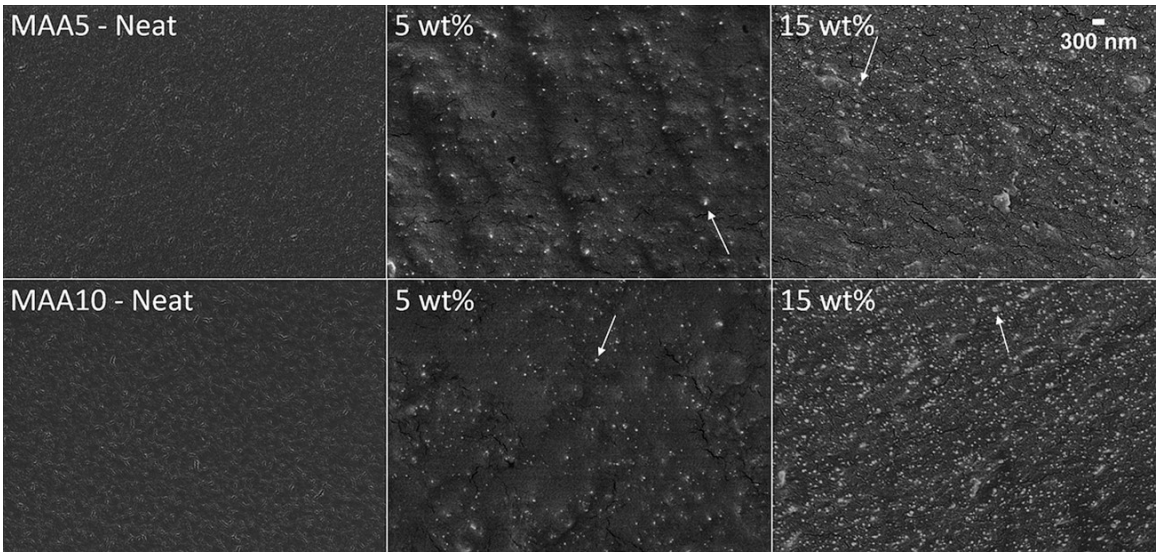

Figure 2.9: SEM images of the cryo-fractured surfaces of MAA5 (top) and MAA10 (bottom) latex films. Scale bar is 300 nm and applies all images. Arrows pointing to white regions representing CNC aggregates.

2.3.3 Film transparency

The UV-Vis transmittance spectra of latex/CNC films over the visible wavelength range of 400-800 nm are shown in Figure 2.10. The transmittance at 550 nm is shown in Table 2.2 and was reduced from 92.1% to 74.3% as CNC loading increased from 0 wt% to 15 wt% for MAA5. Behavior was similar for MAA10/CNC. The optical transmittance depends on the dispersion of CNCs in the dry latex matrix, and these changes are within ranges reported previously. For example, a transmittance of 70% was observed in a butyl methacrylate latex film loaded with 4 wt% CNC, compared to a neat latex transmittance above 95% [116].

Table 2.2: Light transmittance (%) of neat and CNC loaded latex films: a) MAA5, b) MAA10 at 550 nm.

CNC loading (wt%)	Transmittance (%)[a]	
	MAA5	MAA10
0	92.1	95.3
1	91.8	93.1
3	90.2	91.2
5	88.5	89.2
8	82.4	84.4
10	79.6	83.3
15	74.3	72.3

[a]Standard deviation was less than 2% for each measurement.

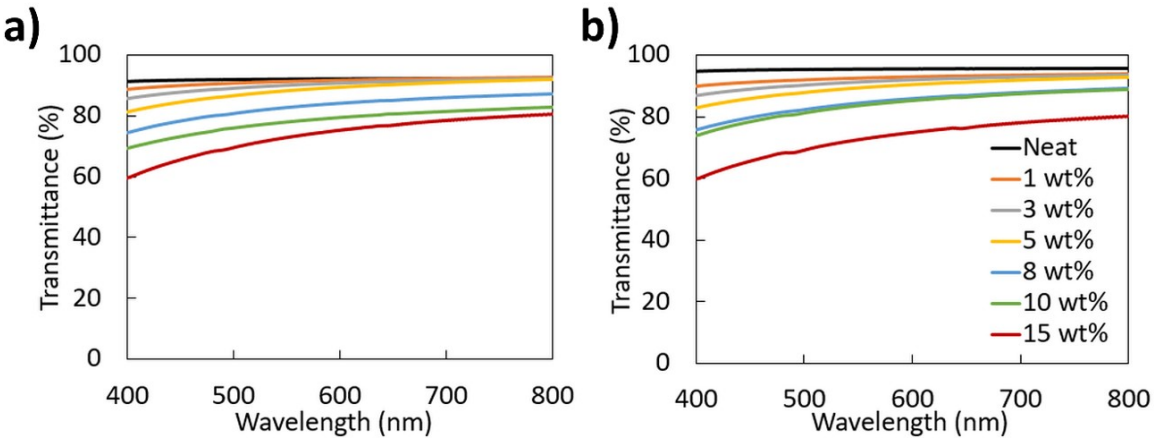

Figure 2.10: Light transmittance spectra of neat and CNC loaded latex films: a) MAA5, b) MAA10.

2.3.4 Water content

Water content and CNC composition in the composite films dried at ambient temperature were determined with TGA, and the results are shown in Figure 2.11. Neat films had a single-step weight loss whereas CNC-loaded (5 and 15 wt%) samples showed a two-step profile. The initial weight loss increased with increasing CNC content. The onset temperature of thermal degradation for CNCs was determined to be around 290 °C from the first weight loss step. Neat latexes began degrading at around 380 °C. However, no significant weight loss was observed at around 100 °C, suggesting that an undetectable

quantity of water was retained. This was further tested by drying the 5 wt% CNC loaded MAA5 and MAA10 latex films at 100 °C for three hours followed by TGA. The results were similar to those obtained after drying at ambient conditions (Figure 2.12), suggesting that the addition of CNCs did not change the water retention behavior.

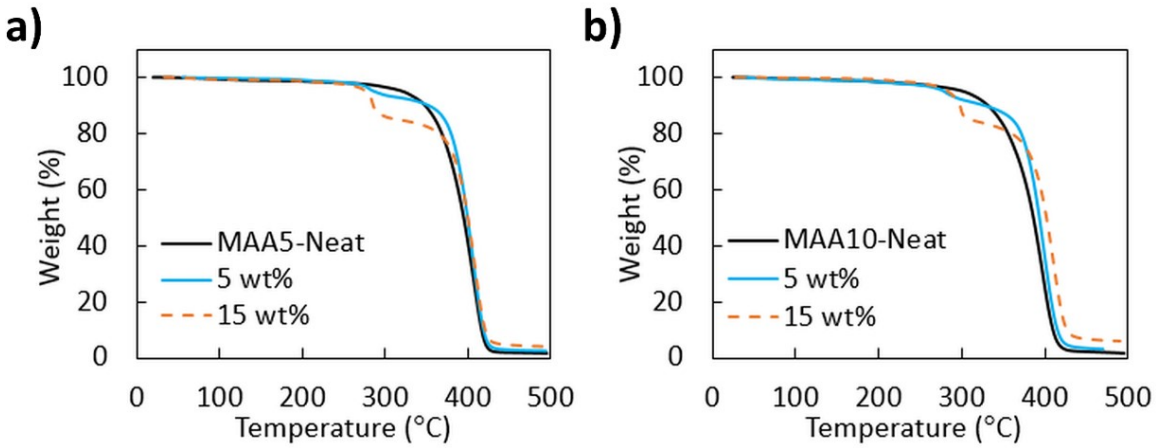

Figure 2.11: TGA weight loss (%) for neat latex films and their CNC loaded composites: a) MAA5, b) MAA10.

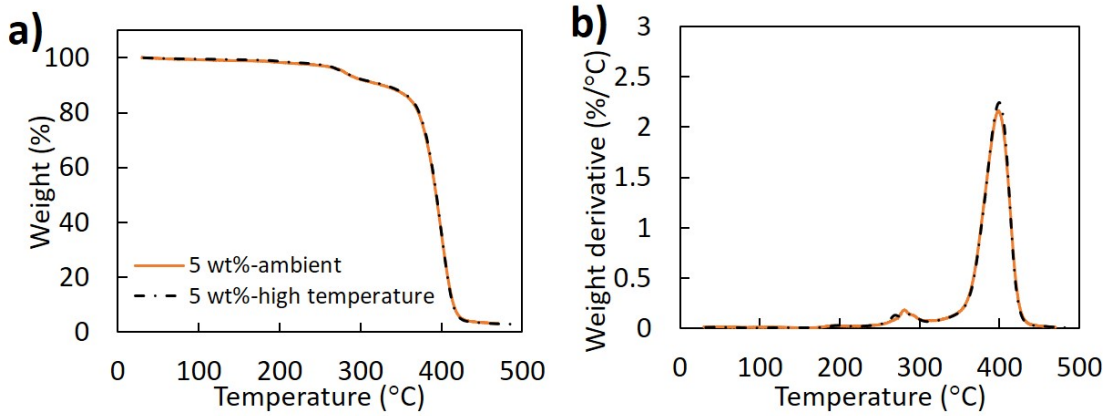

Figure 2.12: Effect of drying temperature on weight loss for water in the films.

To confirm the effect of CNCs on the water content remaining in the films after drying, FTIR spectra were collected from neat and CNC-loaded films. The spectra are shown in Figure 2.13. A higher absorbance at 3000-3600 cm^{-1} corresponding to -OH stretching was observed for the CNC loaded samples. The absorption for -OH could be caused by not only

CNCs but also by water remaining in the films. Similar to the TGA experiments, 5 wt% CNC loaded samples were dried at 100 °C for three hours. The FTIR spectra of films dried at high and ambient temperature were compared by performing paired t-tests (α=0.05). We found no significant difference between the two spectra (Figure A.3) suggesting that the increased intensity of the -OH was due to CNC addition and not increased water content.

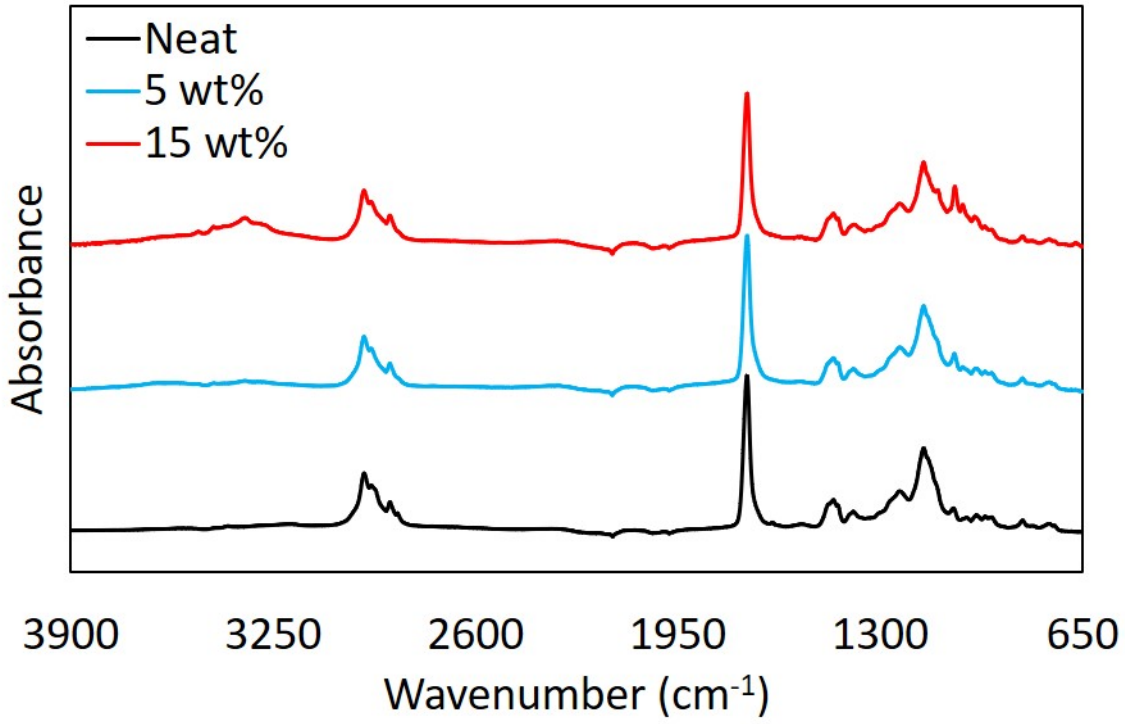

Figure 2.13: ATR-FTIR spectra of neat, 5, and 15 wt% CNC loaded latex films of MAA5.

2.3.5 Mechanical performance

Mechanical property changes due to CNC addition and latex composition were assessed using several methods. We obtained UTS and strain at break from a biaxial tensile test. The uniaxial tensile test provided stress-strain curves, from which we calculated Young's modulus values in addition to UTS and strain at break. Nanoindentation experiments produced force vs. displacement profiles of the composite films from which hardness was obtained. We performed pencil hardness and Koenig pendulum tests as well.

Figure 2.14 shows biaxial tensile testing results of films containing 0-15 wt% CNC. UTS increased with increasing CNC loading, whereas strain at break decreased. UTS was increased from 9 MPa to 16 MPa by loading 15 wt% CNC compared to the neat film. MAA10 composites resulted in higher UTS and lower strain at break values compared to MAA5 composites. We confirmed that dilution of latexes with water in the CNC dispersion did not affect the results of tensile testing (Figure A.4).

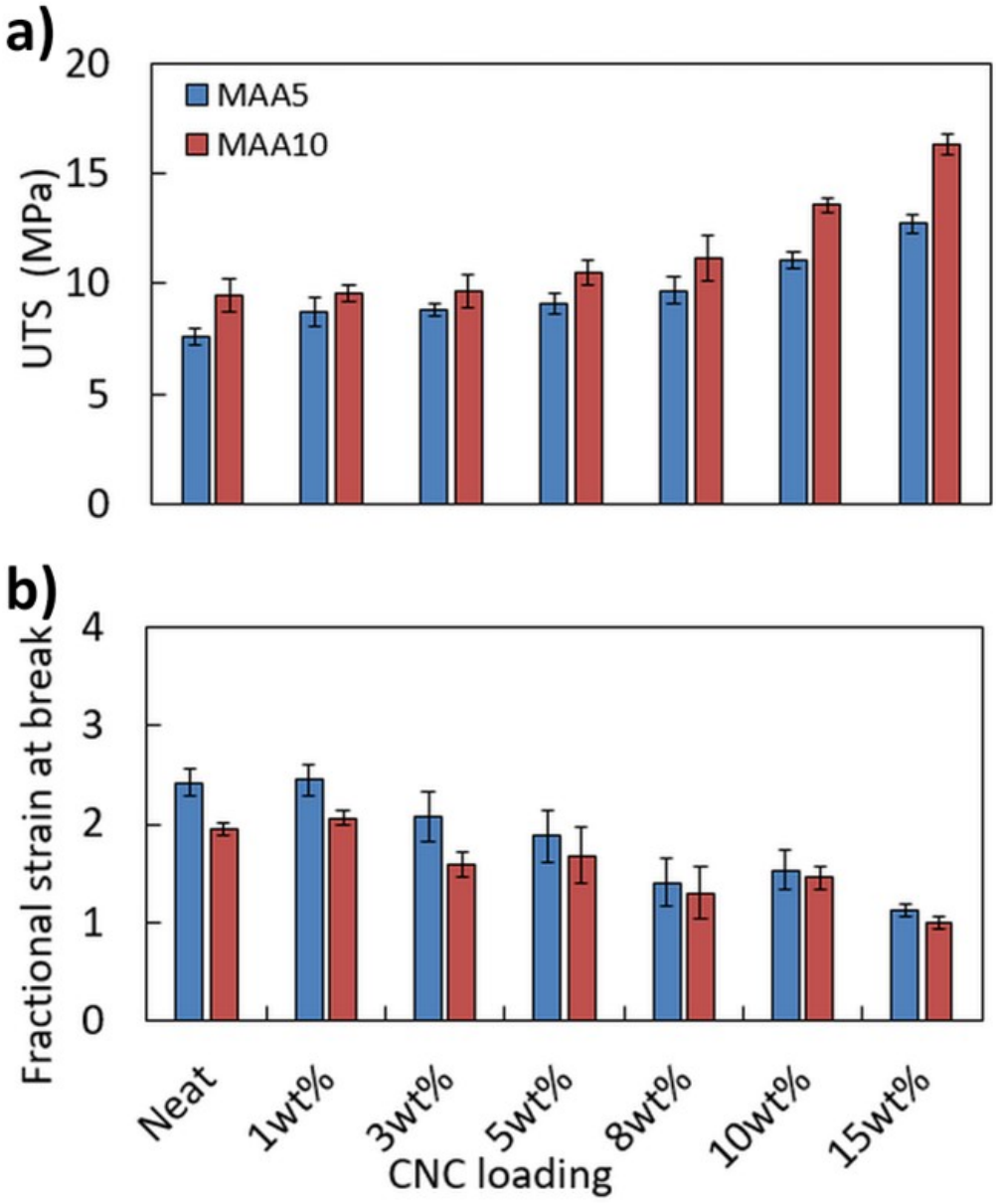

Figure 2.14: Biaxial tensile test results of neat and CNC loaded latex films: a) UTS, b) strain at break.

Figure 2.15 shows strain-stress curves obtained from uniaxial tensile testing and Table A.5 summarizes the calculated modulus values, which increased with the addition of CNCs. Similar to biaxial tensile results, increased CNC loading resulted in decreased strain at break and increased the UTS of the films. MAA5/CNC had slightly higher strain at failure values compared to MAA10/CNC films. The 15 wt% CNC loading increased the modulus by a factor of 30$\times$ and 40$\times$ in MAA5 and MAA10, respectively, relative to neat films. We obtained a Young's modulus $\sim$500 MPa in 15 wt% CNC films, in the range moduli of high T_g binder used commercially [117]. Limousin et al. [102] studied composite latex/CNC films having a morphology similar to this work. Starting with a harder latex prepared with 50 wt% BA and 50 wt% MMA, the modulus increased from 37 $\pm$ 5 MPa in the neat film to 270 $\pm$ 20 MPa when the latex film was loaded with 20 wt% CNC. Further improvement could be expected if CNCs were in situ added during latex synthesis. Dastjerdi et al. [118] observed difference in mechanical performance of the CNC loaded pressure sensitive adhesive (PSA) films when in situ vs blending technique was used for the addition of CNCs. In situ method resulted in greater improvement in the shear resistance, tack and peek strength of the PSA films compared to results obtained from blending method. The difference in the improvements of properties was associated with the better interaction of CNCs with the latex because CNCs were mixed with the latex for a longer time at elevated temperature when in situ loaded.

A higher MAA composition in the latex was associated with slightly enhanced tensile strength and modulus. MAA is a water-soluble monomer carrying a carboxyl group. The distribution of MAA in latexes is sensitive to pH of the aqueous phase, the reactivity ratios for copolymerization, and the polymerization method (batch or semi-continuous) [119]. Depending on pH at polymerization, MAA may be in the particle interior, on the particle surface or in the aqueous phase [120]. Our latexes were synthesized with the aqueous phase at pH=3.5-4. By keeping pH just below the pKa of MAA (4.65), we aimed to distribute carboxyl groups close to the surface of particles, increasing the chance of interaction of MAAs

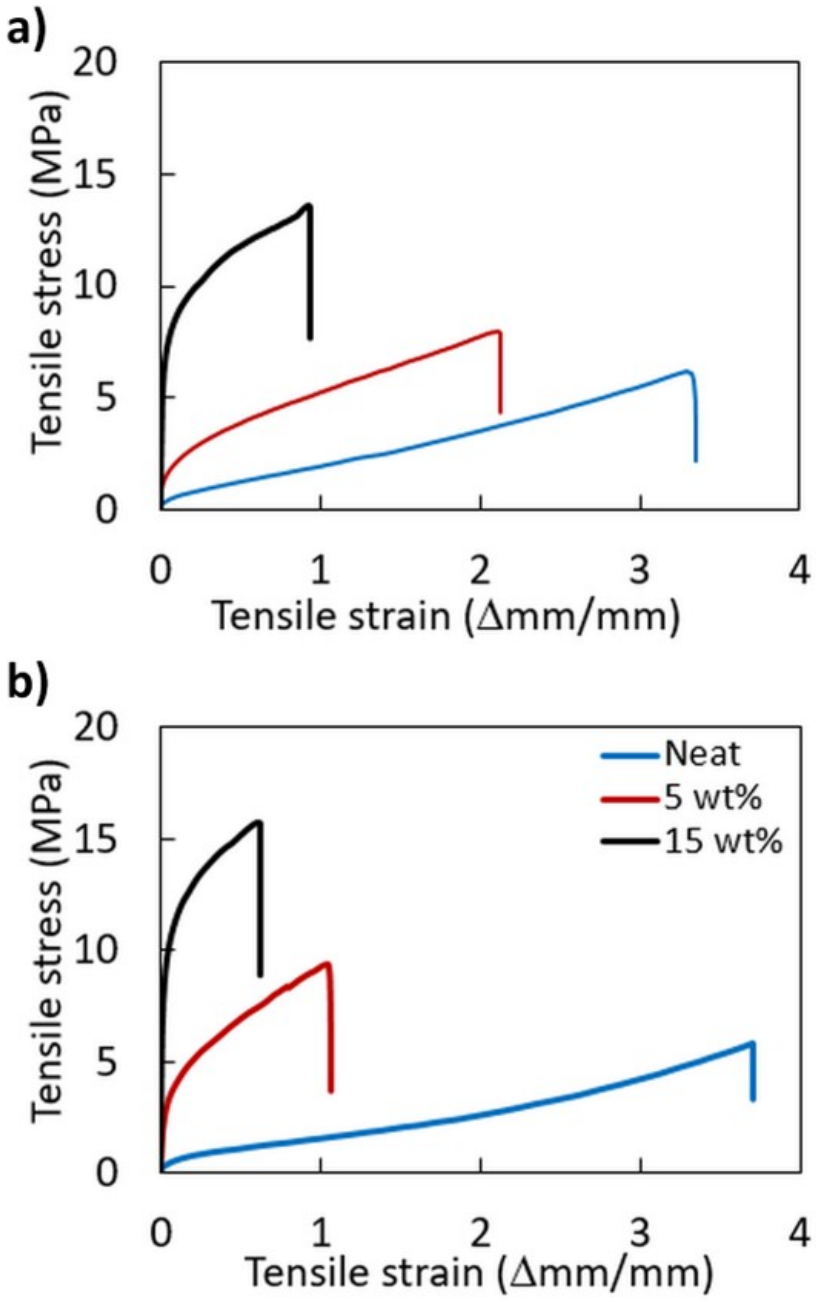

Figure 2.15: Strain-stress curves from the uniaxial tensile test of neat and CNC loaded latex films: a) MAA5 and b) MAA10.

with CNCs. After the polymerization, latexes were neutralized, and carboxyl groups were charged. MAA has various effects on film formation: (a) Charged carboxyl groups assist to the colloidal stability in latexes. The electrostatic stabilization in the latex may promote dispersion of CNCs in the latex. (b) Carboxyl groups provide hydrogen bonding and

ionic dipole interactions between latex particles. Wang et al. [121] studied the pH influence of the wet carboxylated BA latex on molecular interactions in the dry films and, in turn, on their mechanical properties. At a pH of 9, they found that ionic dipolar interactions contribute to the film stiffness and cohesion more than hydrogen bonding. A study by Feng and Winnik [122] proposed that a pH drop in latexes neutralized by ammonium hydroxide during film formation was due to the evaporation of ammonia. The decrease in pH leads to protonation of carboxylate groups on the surface of particles, diminishing the ionic dipolar interactions. Therefore, we expect both mechanisms of hydrogen bonding and ionic dipolar interactions in our latexes. We also expect ammonium evaporation and a pH drop during drying of latexes, decreasing the contribution of ionic dipolar interaction to film strength. (c) Carboxyl groups on the surface of latex particles interact with hydroxyl groups on CNCs. Lu and Hsieh [106] established the existence of hydrogen bonding between acid groups and hydroxyl groups on CNC in poly(acrylic acid)/CNC nanocomposites. (d) Carboxyl groups hold water by forming hydrogen bonding with the trapped water in the film, reducing the effective T_g of polymers called hydroplasticization [123]. We think that the hydroplasticization effect of MAA is limited in our case because BA composition in the latex synthesis is more than 50%, resulting in T_g below ambient film formation temperature.

The loading and unloading force vs. displacement curves from nanoindentation experiments are reported in Figure 2.16. Displacements increased with increasing peak loads in each tested latex film. Since we kept the indentation time constant, peak loads increased with increasing CNC content; however, indentation displacements became smaller even though higher loads were achieved. This result suggests improvement in film hardness with added CNC. Although the negative force values indicated adhesive interaction between the tip and the sample, the film hardness was calculated from the loading curves, which are not affected by the tip-sample adhesion.

Figure 2.17 shows the hardness values of the films obtained from three different tech-

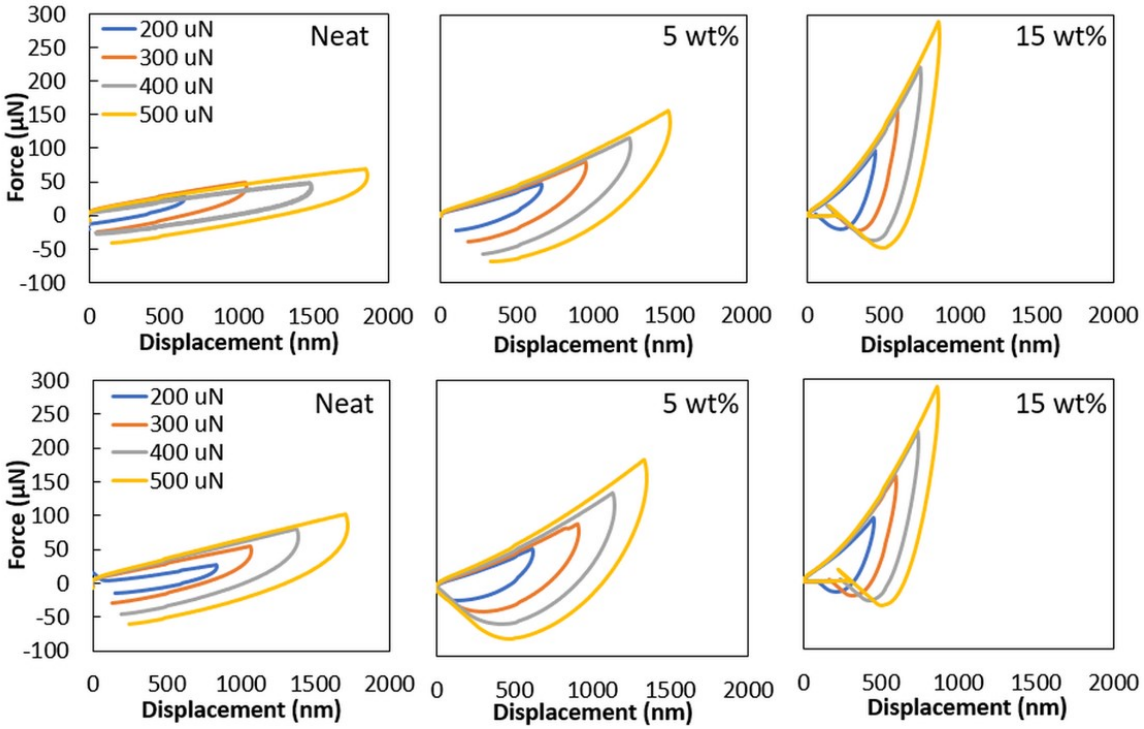

Figure 2.16: Force vs. displacement plots from nanoindentation: MAA5 (top) and MAA10 (bottom) at different loading forces.

niques. In Figure 2.17a, nanoindentation curves showed a significant enhancement in hardness with CNC loading. MAA content did not significantly affect the indentation hardness. The 15 wt% CNC loadings had a hardness 10× over that of neat latex. Abitbol et al. [100] was able to increase the indentation hardness of VOC-containing styrene-acrylic latex coatings 2.5× by loading 9 wt% CNC while the hardness of neat coating was 7 MPa. We obtained the same improvement at a loading of 5 wt% CNC by increasing the hardness from 1.5 MPa to about 3-4 MPa, without use of high T_g acrylic that requires added coalescent.

The pencil hardness of the neat and CNC loaded (5 and 15 wt%) films is shown in Figure 2.17b. Pencil hardness is less quantitative than nanoindentation hardness but is a common industry standard. The highest pencil grade that will neither cut nor scratch the film surface is the scratch hardness. The highest grade that will not cut through the film defines the gauge pencil hardness. All films were scratched by all grades (from softest 6B

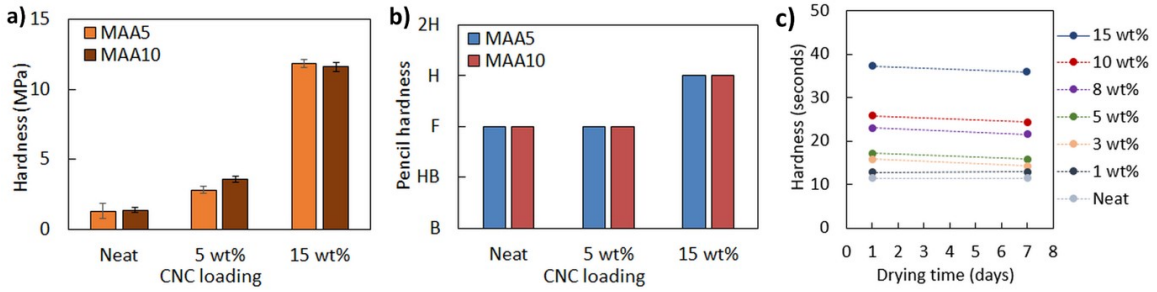

Figure 2.17: Hardness values obtained from a) nanoindentation, b) pencil hardness test, c) Koenig pendulum test.

to hardest 6H). Neat MAA5 and MAA10 latex films, and their 5 wt% CNC loaded films resulted in gauge pencil hardness of F. The 15 wt% CNC loaded films had a gauge pencil hardness of H, an improvement of one pencil grade.

CNC loaded latexes were also tested for the Koenig hardness, which is an industry-standard test for coatings. A typical coalescent-containing hard acrylic film toughens over days, and hardness increases from the 1st to 7th day after the coating application. During this period, coalescent evaporates into the air. A benchmark hard acrylic containing coalescent gives a Koenig hardness of 31 s in the 1st day and 47 s in the 7th day [124]. The Koenig hardness results are given in Figure 2.17c for CNC loaded coalescent-free MAA5 acrylic formulation. CNC loading improved the hardness in the 1st day at all compositions. The addition of 15 wt% CNC into neat MAA5 latex increased the hardness to 37.3 s (Figure 2.17c). No difference was observed between readings of 1st and 7th day in the CNC loaded latexes because no evaporative coalescent was present.

Santos et al. [125] studied the effect of three types of coalescent on MFFT, coalescence and Koenig hardness of acrylic paint formulations. Pure acrylic latex having a MFFT of 17 °C was used. The coalescents were divided into three categories based on VOC content: 100 g/L, 50 g/L, and zero VOC. Coalescents containing 100 g/L VOC were organic solvents that favor the interdiffusion of polymer particles. The 50 g/L and zero VOC coalescents contain solvents with high molecular weights and boiling points. They remain in the latex films after drying and negatively affect the hardness of the coatings. All coalescents re-

sulted in decreased MFFT in a similar manner. Better coalescence was observed in AFM images for latex films containing 50 g/L and zero VOC coalescent. However, zero-VOC coalescent resulted in poor hardness evolution, decreasing the Koenig hardness approximately 50% compared to the latex with 100 g/L VOC. While the zero VOC high molecular weight coalescent plasticizer negatively affected hardness evolution in that work, the approach using soft acrylic with up to 15 wt% CNC loading enhanced the Koenig hardness almost 230% relative to neat films without compromising film coalescence.

The use of CNCs in this work enhanced the mechanical performance of soft latex films to an extent similar to other colloidally-stable, hard nanofillers. However, using CNCs may be more attractive for sustainability because CNCs are renewably-sourced. As a way to assess the benefits of this approach, the results obtained here are compared to literature results with a common hard mineral nanoparticle, silica. Silica nanoparticles have some similarities to CNCs, facilitating this comparison. Both CNCs and silica particles are stiff materials with high surface area and hydroxyl-rich surfaces. Additionally, silica has been frequently used as a reinforcing agent in waterborne latexes. Ramos-Fernández et al. [126] in situ incorporated colloidal silica (7 nm particle size) into the aqueous phase of BA/MMA latexes. Silica nanoparticles were adsorbed on the surface of the latex particles. The 20 wt% silica loading increased nanoindentation modulus to 1.25 GPa from 0.4 GPa (neat film) ($\sim$3$\times$ improvement). Abitbol et al. blended fumed silica (10 nm primary particles) and CNC (110 ± 7 nm $\times$ 7.5 ± 0.5 nm) into a waterborne styrene-acrylic latex separately. The measured hardness of 2-5 wt% CNC loaded films was similar to the hardness of 9 wt% silica loaded film, suggesting more efficient reinforcement with CNCs.

CNCs have low to negligible toxicity based on a recent review [127]. Despite the limited number of studies, CNCs have thus far been found to be non-toxic upon ingestion or contact with skin. The health effects on inhalation and cytotoxicity are less conclusive because of the different physicochemical properties of CNCs from different sources and impurities remaining after their production.

A few life cycle assessment (LCA) studies [128–130] were performed to understand the environmental impacts of nanocellulose production and to guide its industrialization efforts. Energy optimization in CNC production has progressed slowly due to immaturity of the production technology. One challenge in interpreting LCA studies available is that the initial refinement from biomass to pulp containing at least 85 wt% cellulose [131] is done at paper mills, but available LCA studies considers pulp as the starting material. Additionally, $\sim$65% of energy consumption [128] in CNC production after pulping is from producing sulfuric acid used for hydrolysis of cellulose and sodium hydroxide used to neutralize the acid after the hydrolysis. Researchers have been working on techniques [132] to increase the production yield and reducing acid or base used, including recovery of hydrolyzing acid [69], integration of nanocellulose production with pulping processes [133], the AVAP® technology from American Process Inc. [134] and R3™ technology from Blue Goose Biorefineries [135].

2.4 Conclusions

We reinforced coalescent-free BA/MMA/MAA latexes with CNCs by a simple blending method. Due to the high composition of BA in the formulations, the latexes formed uniform films at ambient conditions. All coatings had a MFFT of 0 °C, and T_g lower than MFFT, regardless of CNC loading. SEM imaging suggested that the CNCs were confined to interstitial regions between latex particles, and these collections of CNCs were distributed through the bulk of the film. Film transparencies in the range of 93.1 – 72.3% were obtained in films loaded with 1-15 wt% CNC. CNC loadings significantly enhanced the tensile strength, Young's modulus, and hardness without negatively affecting ambient film formation. We obtained slightly higher tensile strength and Young's modulus measurements in the latex films with higher MAA content. A 10$\times$ improvement was achieved in the nanoindentation hardness with the addition of 15 wt% CNCs. The composite films reached maximum hardness in the first day of drying without coalescent. This work highlights the

remarkable effect of CNC addition on the mechanical performance of coalescent-free latex coatings. The mechanical properties achieved are comparable with the conventional binders that use VOC coalescents with hard acrylic polymers and exceed properties (such as Koenig hardness) of binders that use non-volatile coalescents that remain in the coating. The CNC loaded nanocomposite latexes studied in this work are potential binders useful for the development of zero-VOC waterborne acrylic coatings. The use of CNCs does lead to questions about the interaction of the CNC with other components (beyond the binder) used in commercial formulations. While the scope of this study is focused on the binder itself, it encourages reformulating studies of waterborne acrylic products with CNCs.

CHAPTER 3

ACRYLOYL-MODIFIED CELLULOSE NANOCRYSTALS: EFFECTS OF SUBSTITUTION ON CRYSTALLINITY AND COPOLYMERIZATION WITH ACRYLIC MONOMERS

This chapter demonstrates a framework to functionalize the CNC surface with acryloyl groups and acrylic polymers. The influence of modification reaction was studied to optimize the degree of substitution, crystallinity, and morphology of the CNCs. Also, the copolymerization ability of acryloyl-modified CNCs was verified and the dispersion of polymer-grafted CNCs in the acrylic matrix was assessed (Figure 3.1). Appendix B presents the supporting information for this chapter.

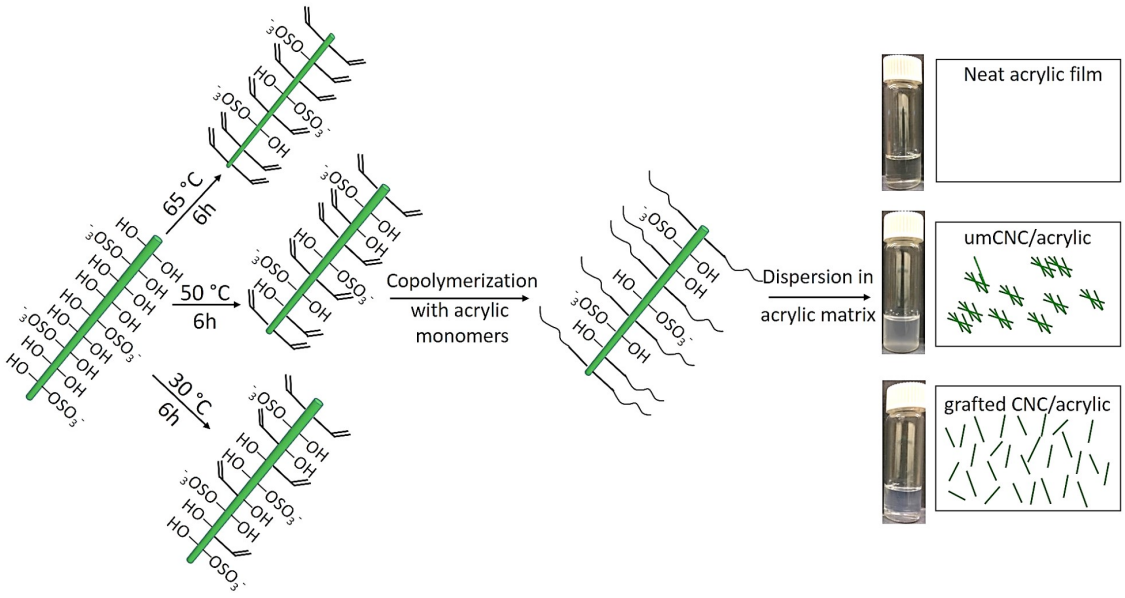

Figure 3.1: Schematic showing CNC functionalization with acryloyl groups at different reaction conditions, polymer-grafted CNCs, and their dispersion performance in the acrylic matrix.

3.1 Introduction

The use of cellulose nanocrystals (CNCs) as a reinforcement material has been of substantial interest in the nanocomposite field because of CNC's renewable precursors, high mechanical properties, ability to be chemically functionalized and low density relative to other hard fillers [49, 50]. CNCs are rigid rod-like particles derived from cellulose, which is a structural component of the cell wall of various plants. Cellulose contains both crystalline and disordered fractions, and CNCs are the crystalline fractions that are typically extracted by sulfuric acid hydrolysis of cellulose fibers. This acid hydrolysis imparts negatively charged sulfate half ester groups to the hydroxyl-rich CNC surface. These charged sulfate groups facilitate obtaining stable aqueous CNC dispersions, lending support to research for inclusion of CNCs in waterborne materials. Many publications [100–102, 136], including our previous work [88], have reported that CNCs enhanced the mechanical performance of waterborne polymers. Recently, Kedzior et al. [136] extensively reviewed the use of nanocellulose in emulsions and heterogeneous water-based polymer systems. The extent of CNC dispersion in the polymer matrix is a limiting factor for effective property enhancement despite the fact that CNCs and water-soluble polymers are each compatible with water [137]. This limiting factor becomes more significant in a hydrophobic polymer system due to the aggregation of CNCs in nonpolar solvents or polymer matrices [137, 138].

Different surface modification methods have been explored to increase the compatibility of CNCs with hydrophobic materials. Chemical modification can take place by attaching small molecules to the CNC surface with various approaches such as urethanization, silylation, amidation, esterification, and acetylation [75]. Among these approaches, urethanization has been used in various chemical modification studies [139–143] due to the high reactivity of isocyanates with various functional groups including amino (-NH_2), hydroxyl (-OH), and carboxylic acid (-COOH) [144]. Abushammala and Mao [145] re-

cently reviewed the use of aliphatic and aromatic mono- and di-isocyanates in the surface modification of cellulose and nanocellulose. Despite the reports on the modification of cellulose going back to the 1960s, isocyanate modification of nanocellulose has been explored only since 2008. The isocyanates most commonly used for nanocellulose modification are phenyl isocyanate, n-octadecyl isocyanate, toluene diisocyanate, diphenylmethane diisocyanate, and hexamethylene diisocyanate. Our research group's previous works [146, 147] also showed that isocyanate functional groups could form a basis for site-selective CNC functionalization. Girouard et al. [146] modified CNCs by using isophorone diisocyante to improve the degree of nanoparticle dispersion in polyurethane-CNC composites. Qu et al. [147] used isocyanatoethyl methacrylate (IEM) for CNC surface modification and reported better dispersion in poly(methyl methacrylate)-CNC composites relative to unmodified CNC (umCNC).

Not only small molecules but also polymers can be attached to the nanoparticle surface, providing another pathway for increasing component compatibility in CNC/polymer composites [148]. Three main approaches to graft polymers on CNC surfaces are *grafting to*, *grafting from* and *grafting through* [149]. *Grafting to* is a method where preformed polymer chains are covalently bound to the surface through reactive end groups while *grafting from* involves the growth of polymer chains initiated from the surface through surface-attached initiator moieties. *Grafting through* is a method consisting of both *grafting to* and *grafting from* principles. In *grafting through*, the chain growth of polymers is initiated in solution and propagation on CNCs can be either by chain growth from the surface-attached monomers or by anchoring of polymer chains formed in the solution. Although the *grafting through* technique is applied in some industrial applications such as adhesion promoters, it is less explored from a scientific point of view. Henze et al. [87] studied mechanistic aspects of *grafting through* by polymerizing polystyrene on silica gel with surface-attached trimethoxysilanes. One conclusion was that a reduced steric hindrance leads to a slight increase in grafting density compared to *grafting to* polymerizations.

According to Eyley et al. [150], researchers rely on elemental analysis to quantify the degree of modification but do not often investigate whether the modification is limited to the surface or occurs on chains beneath the surface, disrupting crystallinity. Among the works with isocyanate-modified CNCs, some studies [151–154] focused on characterization of the polymer nanocomposites prepared with mCNCs and reported the crystallinity of the nanocomposites. Numerous studies[142, 146, 147, 155] explored the crystallinity of mCNC compared to umCNC. However, none of these studies investigated the effects of reaction conditions on the extent of modification and the CNC crystallinity and morphology.

In this work, the CNC surface was modified by IEM molecules via urethanization (Figure 3.2a). IEM is a bifunctional molecule with both isocyanate and vinyl functional groups. The aim was to investigate in detail, with a known CNC modifier, how to achieve optimal surface coverage and to understand the trade-off between degree of substitution and CNC properties like crystallinity. To test the polymerizable functionality of the attached methacrylate groups, acrylic polymers were then grafted via *grafting through* (Figure 3.2b) by using the polymerizable methacrylate groups on modified CNCs (mCNCs). We used butyl acrylate and methyl methacrylate monomers for *grafting through* polymerization because they are two of the most commonly used acrylic monomers in commercial paints and coatings. Beyond demonstrating the functionalization route and copolymerization, we examined the effects of reaction conditions on the degree of modification and the structure of the CNCs, which is necessary to understand the balance between achieving adequate surface modification and maintaining the CNC's structure. Finally, the grafted mCNCs (gmCNC) were incorporated into an acrylic polymer matrix to assess the efficacy of the functionalization scheme on the dispersion and physical properties.

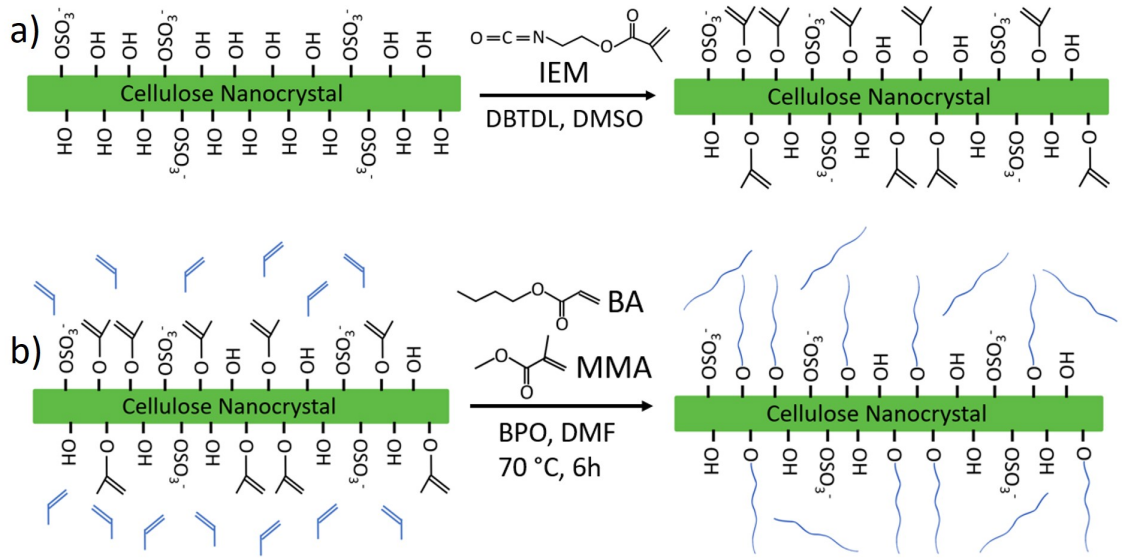

Figure 3.2: Schematic of a) surface modification of CNC, b) copolymerization of mCNC with monomers via *grafting through*.

3.2 Experimental section

3.2.1 Materials

Freeze-dried CNCs produced by sulfuric acid hydrolysis were received from US Forest Service Forest Products Laboratory, Madison, WI. 2-isocyanatoethyl methacrylate (IEM, at >98% purity), dibutyltin dilaurate (DBTDL), toluene (ACS, 99.5%), dimethylformamide (DMF, anhydrous, 99.8%), methanol, tetrahydrofuran (THF) and n-hexane were purchased from Sigma-Aldrich and used as received. Dimethyl sulfoxide (DMSO, extra dry, $\geq$ 99.8%) in the 100 ml AcroSeal™ bottle was purchased from ACROS Organics. Butyl acrylate (BA - >99%) and methacrylic acid (MAA - >99%) were purchased from TCI America. Methyl methacrylate (MMA - 99%), ethyl acrylate (EA - 99%), 2-hydroxyehtyl methacrylate (HEMA - 98%), and benzoyl peroxide (BPO, Luperox® A98), and inhibitor remover column were obtained from Sigma-Aldrich. Acrylic monomers (stabilized with MEHQ) were passed through the inhibitor remover column before the polymerization.

3.2.2 Immobilization of IEM onto CNC

umCNCs were mixed with the anhydrous DMSO at a concentration of 0.01 g/ml in a septum-sealed vial. The mixture was sonicated for 30 min with a 2510 Branson bath sonicator to disperse the CNCs in DMSO. A two-neck round bottom flask with rubber stoppers was submerged in a heated oil bath and the flask was purged by a nitrogen stream for 20 min. The CNC/DMSO dispersion was transferred from the septum-sealed vial to the heated reaction flask by using a syringe and a needle. IEM (0.625 g) and DBTDL (33 μl) were quickly mixed in a separate vial and added dropwise to the stirring CNC/DMSO dispersion. The resulting mixture in the flask was magnetically stirred under a nitrogen flow at a specific temperature and time. We studied three reaction temperatures and different reaction times up to 24 h. These conditions and the sample nomenclature are summarized in Table 3.1. The molar ratio of IEM to anhydroglucose units (AGU) of CNCs was 6.5:1, and the concentration of DBTDL in DMSO was 0.3 wt% in all reactions. After the reaction, the product dispersion was washed with toluene and centrifuged at 3000 rpm for 10 min. The centrifuged mCNCs were redispersed in DMF and vacuum-dried (60 °C - 24 h) for characterization experiments. The same procedure was applied to umCNC as well.

Table 3.1: Nomenclature of mCNC samples synthesized at different reaction temperatures and times.

		Sample name	Temperature	Time
		umCNC	65 °C	24 h
		30C-6h	30 °C	6 h
50C	samples	50C-2h	50 °C	2 h
		50C-6h		6 h
		50C-12h		12 h
		50C-18h		18 h
		50C-24h		24 h
65C	samples	65C-30m	65 °C	30 min
		65C-2h		2 h
		65C-6h		6 h
		65C-18h		18 h

3.2.3 Characterization of CNC samples

ATR-FTIR spectroscopy was performed on vacuum-dried CNCs using a Nicolet 6700 FTIR spectrometer equipped with a diamond crystal single bounce ATR attachment. Spectra were obtained with a resolution of 4 cm^{-1} and using 64 scans at a range of 4000 – 650 cm^{-1}. To compare different reaction conditions, the spectra were normalized at the 1060 cm^{-1} peak associated with the C-O vibration of the third carbon.

XRD analysis of CNC samples was performed by a Panalytical Empyrean XRD with Cu Kα radiation (λ=1.54 A°) with the generator set to 45 kV and 40 mA. To prepare the samples, the mCNC/DMF dispersion was poured onto a zero-background Si plate, and the sample was allowed to dry overnight. The plates were then mounted to the sample holder of the diffractometer. The sample holders were rotated at 16s per revolution during data collection. The XRD patterns were collected at 2θ = 10 - 60° by using a step size of 0.003° and a counting time of 8.67 s per step. The crystallinity percentage (Cr %) was estimated by using the peak deconvolution method [156]. The Cr % was obtained from the ratio of all crystalline peaks' area to the total area in the XRD spectrum. The areas were determined by peak integration.

Water contact angle measurements were carried out with a Ramé-Hart goniometer at room temperature. mCNCs were coated on glass slides and vacuum-dried (60 °C - 24 h). Five deionized water droplets (10 μl) were placed on each sample. The water contact angles were measured 60 s after the water droplets were dispensed.

Thermal stabilities and degradation patterns of CNC samples were studied by TGA (TA instruments Q50) with a heating rate of 10 °C/min. The samples were heated from 25 °C to 600 °C under a flowing nitrogen atmosphere.

To assess the degree of modification, elemental analysis was carried out by Atlantic Microlab (Norcross, GA) for C, H, N, and S contents of the CNC samples. The lab performed analyses by combustion using automatic analyzers. The results were used to calculate the degree of substitution and percent conversion of surface hydroxyls on mCNCs for uretha-

nization reaction.

The morphology of CNCs was imaged by AFM (Bruker Dimension Icon) in tapping mode. CNC/DMF dispersion was diluted to approximately 0.001 wt% and drop-cast on to a piranha cleaned silicon wafer. Height and amplitude images were captured with a probe (HQ:NSC14/No Al-15) that had a resonance frequency of 160 kHz and a force constant of 5 N/m. We analyzed the height images by using Gwyddion software for the size distributions of CNCs. The length and height of 50 isolated particles were measured.

Dispersion tests were performed to study the effect of modification on the CNC dispersion in organic mediums. mCNCs functionalized at a selected condition (65 °C, 30 min) were freeze-dried to make a comparative study with the freeze-dried umCNCs, starting material. The freeze-dried CNCs were mixed with different organic solvents ranging from polar to non-polar (water > methanol > DMF > THF > toluene > hexane) and mixed with different monomers ranging from hydrophilic to hydrophobic (HEMA > MAA > MMA > EA > BA) at a concentration of 1 wt%.

3.2.4 *Grafting through* polymerization of mCNC

Solution polymerization was performed to investigate copolymerization of vinyl groups attached to the mCNC surface with acrylic monomers (BA and MMA). First, umCNC (0.1 g) was reacted with IEM at 50 °C for 2 h. The mCNC purified from the reaction medium was dispersed in DMF (6 g). The mixture was poured into a 50 ml round bottom flask and benzoyl peroxide (5 mg) was dissolved in the mixture as the initiator. Then, BA (1 g) and MMA (1 g) were added to the mixture and the flask was submerged into an oil bath. The flask was purged with a nitrogen flow for 15 min. The temperature of the oil bath was set to 70 °C, and the mixture in the flask was stirred for 6 h for polymerization. After 6 h, the flask was removed from the oil bath and allowed to cool. For comparison, polymerization was performed with umCNC, and a neat BA-MMA copolymer was prepared. Also, we prepared another control sample by mixing the neat BA-MMA polymer solution with the

starting mCNC/DMF mixture with a 1:1 ratio. In order to isolate the reaction products, half of the polymerization solutions were added dropwise to excess methanol (>10× volume) to precipitate the copolymers. The remaining solutions were mixed with toluene and centrifuged at 3000 rpm for 15 min and CNCs were purified from the solution polymers. The copolymers and the purified CNCs were dried at 50 °C for 24 h for the characterizations.

3.2.5 Characterization of copolymers and purified CNCs after copolymerization

The dried copolymers and CNCs were analyzed by using a Nicolet 6700 FTIR spectrometer with a resolution of 4 cm^{-1} and 64 scans of 4000 – 650 cm^{-1}. The samples were sent to Atlantic Microlab for the elemental analysis to calculate the grafting density on mCNC after the copolymerization. We assessed the dispersion performance of gmCNC in the acrylic polymer compared to umCNC. The precipitated copolymers were dissolved in DMF and cast on Teflon substrates for drying at 80 °C for 24 h. We prepared three polymer films: neat BA-MMA copolymer, 6 wt% gmCNC loaded BA-MMA copolymer, and 6 wt% umCNC loaded BA-MMA copolymer. These polymer films were characterized by UV-Vis spectroscopy (Shimadzu UV-1800), PLM (Olympus BX51), HTMECH [107], and nanoindentation (Hysitron triboindenter). UV-Vis spectroscopy was used to assess the light transmission at 550 nm and indicate transparency. Transmittance values were normalized to a film thickness of 100 μm by using the Beer-Lambert law. The HTMECH instrument was used to determine the UTS and strain at break. The HTMECH used a 1.25 mm diameter hemispherical indenter normal to the film plane to puncture the samples at a controlled rate. The films were deformed biaxially while the indenter moved at a speed of 10 mm/s. We performed five measurements per sample. The nanoindenter used a Berkovich diamond indenter in a load-controlled mode to indent the polymer films at room temperature. We performed four indentations per sample and reported the estimated hardness from force vs displacement curves.

The thermal degradation patterns of polymer films were studied by TGA in an anal-

ogous manner as the CNC samples. We performed DSC (TA instruments Q200) under nitrogen to determine glass transition temperatures (T_g) of the polymer films. The samples were first equilibrated at -20 °C and heated to 150 °C at a rate of 10 °C/min. Then, the samples were cooled to -20 °C and heated back to 150 °C at a rate of 10 °C/min. The isothermal steps were for 2 min at the lowest and the highest temperatures. The midpoint T_g was measured from the second heating curve of each sample.

The molecular weight analysis of copolymers was performed by using a gel permeation chromatograph (GPC - Tosoh EcoSEC HLC 8320) equipped with TSKgel SuperHZ-L columns eluting chloroform at a flow rate of 0.45 mL/min at 40 °C. All number-average molecular weights and polydispersity indices were obtained from refractive index chromatograms using PStQuick Mp-M polystyrene standards.

3.3 Results and discussion

3.3.1 Immobilization of IEM onto CNC

The attachment of IEM to the CNC surface was verified by ATR-FTIR spectroscopy (Figure 3.3a), and we assessed the resulting change in the crystallinity of CNCs with XRD (Figure 3.3b). The FTIR spectrum of umCNC had characteristic bands corresponding to hydroxyl stretching (3300 - 3400 cm^{-1}), the C-O stretching of carbons 2, 3 and 6 (1110, 1060 and 1035 cm^{-1}), and C-H stretching (2858 - 2904 cm^{-1}) from -CH_2 groups. New bands appeared in the spectra of mCNC samples. The peak at 1710 cm^{-1} was due to urethane and carbonyl groups on the attached IEMs. The band at 1600 - 1700 cm^{-1} was associated with C=C stretching due to the pendant alkene from the surface of mCNCs.

Similar changes were observed in the spectra of all mCNC samples compared to the spectrum of umCNC (Figure 3.3a). When the reaction temperature was increased, the mCNCs had lower absorbance of hydroxyl groups, higher urethane-related peaks (1400 - 1600 cm^{-1}) and higher C=C stretching (1600 - 1700 cm^{-1}) relative to the absorbance of umCNC. The increase in absorbance of these specific peaks suggested a higher degree of

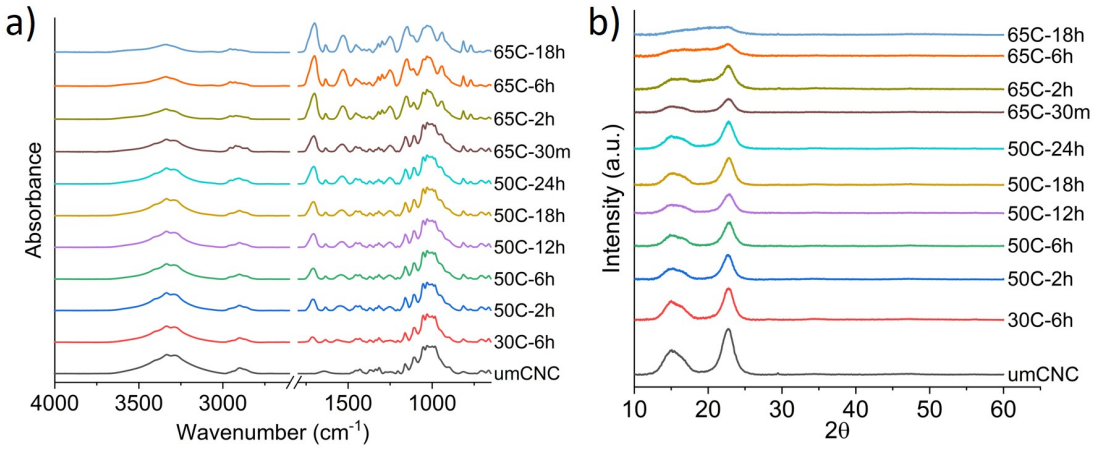

Figure 3.3: a) FTIR spectra and b) XRD patterns of all CNC samples.

IEM attachment to the CNC. Unlike the reaction temperature, reaction time did not result in noticeable differences between the spectra of 50C mCNCs. However, 65C-2h clearly had higher peaks than 65C-30m in the bands associated with the attachment of IEM.

The crystallinity of CNCs was characterized by XRD analysis. All samples, except 65C-2h, 65C-6h and 65C-18h, had well-defined peaks of the monoclinic unit cell for cellulose I_β, assigned to the $(1\bar{1}0)$, (110), and (200) at $2\theta \cong 22.5°$, 14°, and 17°, respectively. However, the XRD pattern of the 65C mCNC samples with long reaction times showed noticeable peak broadening compared to other samples, suggesting changes in the morphology of CNCs. As a control, the umCNC was kept in the same high-temperature reaction environment (65 °C, 24 h), but without IEM, and the umCNC crystallinity was not affected by the long solvent exposure at 65 °C. Therefore, the peak broadening was attributed to changes in the crystallite disorder or size due to the reaction between IEM with hydroxyls on CNCs at 65 °C. Furthermore, we checked the presence of cellulose II in the CNCs by deconvoluting XRD patterns for $2\theta \cong 20°$, in which cellulose II shows the characteristic diffraction peak for the (110) plane [157]. Fitting results showed a peak at $2\theta \cong 20°$ for only 65C-2h, 65C-6h, and 65C-18h mCNC samples, suggesting the presence of cellulose II (Figure 3.4). This result could be attributed to the severe reaction conditions. Cellulose I can partially dissolve and recrystallize as more thermodynamically favorable structure of

cellulose II in certain conditions such as in mercerization when cellulose is exposed to high concentrations of NaOH [71, 158].

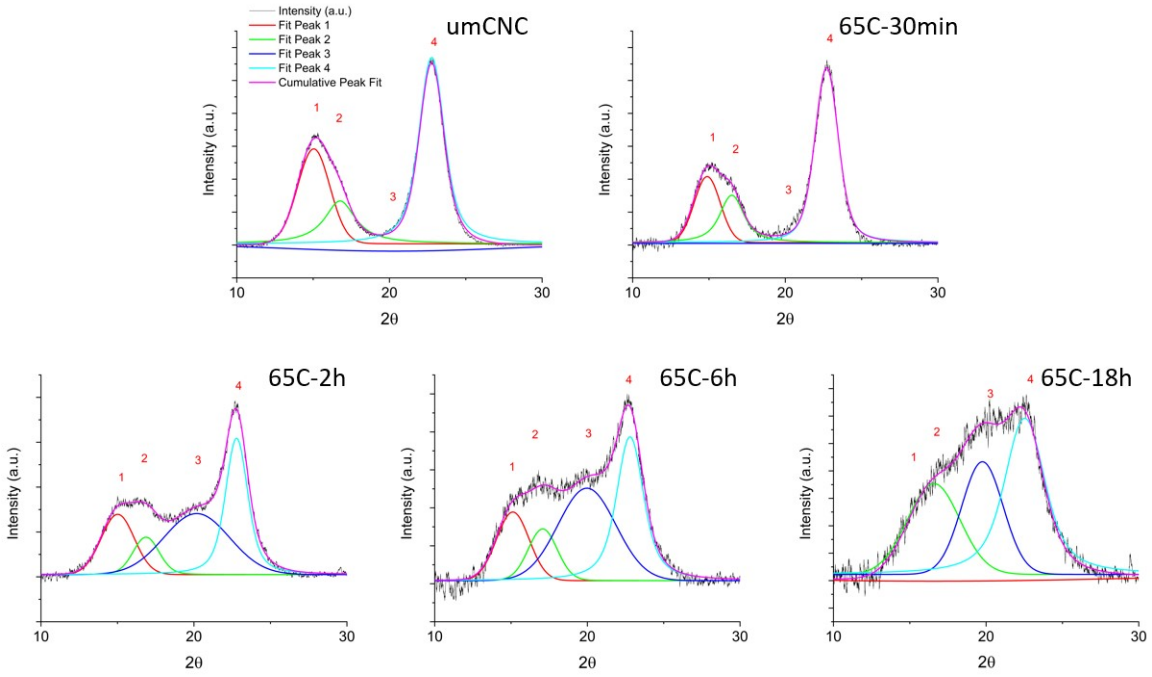

Figure 3.4: Deconvolution of peaks selected at $2\theta \cong 14°$, 17°, 20°, and 22.5° for umCNC and mCNCs synthesized at 65 °C.

To quantitatively assess the change in the degree of modifications in mCNCs, elemental analyses were performed for all samples. Since the nitrogen (N) content was only associated with the IEM groups chemically attached to the CNCs, we used this information to track the IEM content. Figure 3.5a shows the N wt% in the samples. As FTIR results suggested, IEM content increased with increasing reaction temperature. 30C-6h had 1.28 wt% N, whereas 50C-6h and 65C-6h had 2.16 wt% and 5.46 wt% N, respectively. N wt% in mCNCs synthesized at 50 °C slightly increased from 1.89 wt% to 2.47 wt% with increasing reaction time. The increase in N content of the 65C samples with increasing time was more evident compared to the 50C samples.

The water contact angle on films prepared from modified particles was used as an indicator of the extent of surface modification. Figure 3.5a shows the measurements of water contact angle on umCNC and mCNCs. We expected reduced hydrophilicity in mCNCs

relative to umCNC since a portion of hydroxyl groups on the CNCs was reacted with IEM. All mCNCs have a contact angle less than 90°; however, these values were higher than the contact angle of umCNC (33 ± 2°). Water contact angles of mCNCs increased with increasing IEM content. We measured the contact angle 43 ± 1° on 30C-6h, 60 ± 3° on 50C-6h, and 75 ± 2° on 65C-6h. The angles ranged from 56° to 72° in 50C samples with increasing reaction time, whereas the range of 65C samples was from 74° to 78°.

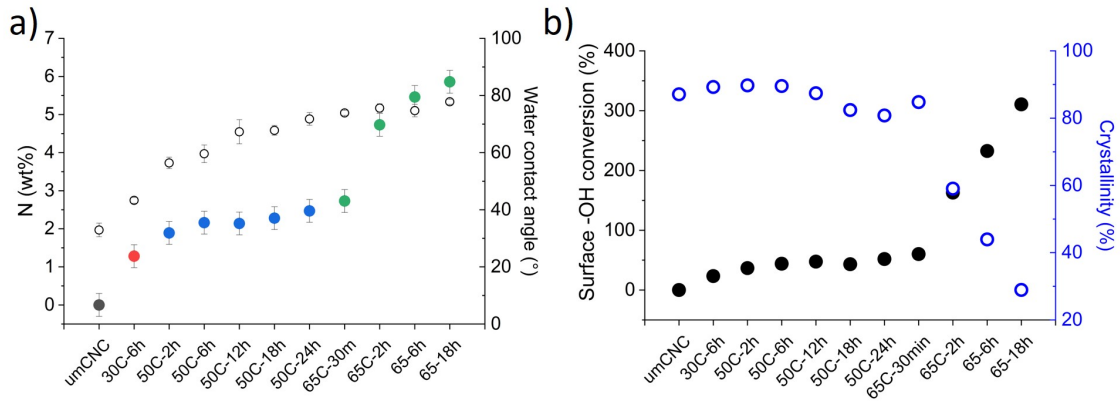

Figure 3.5: (a) fraction of nitrogen, N wt% (unmodified:, 30 °C:, 50 °C:, 65 °C:), and water contact angle measurements () of umCNC and mCNCs prepared at different modification temperatures and reaction times; (b) surface hydroxyl conversion (●) and crystallinity percentage estimated from XRD patterns of umCNC and mCNC samples (○).

The percentage of surface hydroxyls reacted with IEM was estimated using the C, H, N, and S wt% obtained from elemental analysis (see the calculation section in Appendix B). The results are plotted along with the estimated crystallinity percentages of umCNC and mCNCs obtained from XRD patterns (Figure 3.5b) to better understand the relation between the degree of modification and crystallinity of mCNCs. Both 30C and 50C mCNCs maintained a crystallinity similar to umCNCs (87%); however, the crystallinity percentage of 65C samples was significantly reduced for long reaction times (2, 6, and 18 h). The hydroxyl conversions for these samples were estimated to be above 100%, suggesting the penetration of the reaction inside the crystal structure (below the umCNC surface), consistent with the crystallinity percentage calculations. 65C-30m had 84% crystallinity and the highest degree of surface modification corresponding to 60.1 ± 6.6% of surface hydroxyls

reacted. According to Eyley et al. [150], it is unlikely to achieve a surface hydroxyl conversion above 66.6% due to the reduced reactivity of the secondary hydroxyl group at carbon 3. The 65C-30m sample reached nearly to this limit (60.1%), and the modification apparently exceeded the surface groups for longer reaction times explored at 65 °C, resulting in % surface –OH modification exceeding 100%.

Among the previous publications involving isocyanates for CNC modification, many studies [139, 142, 146, 155] reported no significant change in the crystallinity of CNCs after the modification. Morelli et al. [155] and Siqueira et al. [139, 142] modified CNCs by using octadecyl isocyanate (OI) with a reaction in toluene at 110 °C for 30 min. The crystallinity indices reported were within 80-96% determined by the peak intensity method from the XRD patterns. These works calculated the overall (often termed *bulk*) degree of substitution, DS, which is the number of hydroxyl groups modified per AGU in the mCNCs. Siqueira et al. [139, 142] found DS less than 0.10, whereas Morelli et al. [155] estimated DS as 0.23. Girouard et al. [146] modified CNCs by using isophorone diisocyanate with a reaction in DMSO at 60 °C overnight. They determined the crystallinity of CNCs as 66% by NMR spectroscopy and the reported DS is 0.51. The bulk DS in this work (Table B.1) ranges from 0.17 (30C-2h) to 0.45 (65C-30m) for surface modifications and becomes larger than 1 for the highest temperature and longest reaction times where the modifications extended beyond the surface. On the other hand, a few of the isocyanate studies [147, 159] showed a reduction of the crystallinity index in the treated CNCs, determined from XRD measurements. Espino-Pérez et al. [159] used OI to modify the CNCs with a reaction in toluene at 110 °C for 30 min. They observed a decrease from 87% to 74% and did not report the DS. Qu et al. [147] used IEM for the CNC modification with a reaction in DMSO at 60 °C for 2 h. The crystallinity index decreased from 91% to 76% after the modification with the bulk DS = 0.10. Overall, it is not straightforward to draw a conclusion about the relation between the DS and change in the crystallinity of CNCs after isocyanate modification from review of prior literature. To better understand this relation, we studied

the extent of reaction for a specific isocyanate modifier as a function of reaction temperature and time. In summary, we observed that crystallinity of the native CNCs was maintained when the modifications were limited to the CNC surface only. The crystallinity decreased when the extent of substitution indicated that subsurface –OH groups were reacted.

The thermal degradation behavior of CNCs was characterized by TGA. Figure 3.6 displays the weight loss curves of mCNCs synthesized at different temperatures with 6 h reaction time in comparison to umCNC. The initial weight loss in all samples ($<$ 8 wt%) at 25 – 120 °C is associated with the evaporation of the residual solvent. The next weight loss event in umCNC, with an onset temperature of 240 °C, is related to the degradation of the outer layer of the CNC with sulfate groups. The subsequent degradation at 290 – 500 °C corresponds to the slower breakdown of the crystal interior [160]. We observed the onset degradation temperature of mCNCs (278 – 283 °C) to be higher than that of umCNC, possibly due to the urethane linkages and higher C=C bond energy from the IEM on the mCNC surface. Urethane linkages formed between CNC and IEM in mCNCs degrade at around 300 °C [161]. Thus, the mCNCs had higher thermal stability than the umCNC. A similar observation was reported by Gwon et al. [143] when CNCs were modified with toluene diisocyanate and by Girouard et al. [146] when CNCs were modified with isophorone diisocyanate. In both 30C-6h and 50C-6h mCNCs, the last weight loss at 360 – 400 °C was ascribed to the degradation of the CNC interior, similar to the degradation of umCNC. However, the highest temperature weight loss event of 65C-6h was distinct, degrading faster compared to other samples. The change in the degradation rate may be related to the less ordered regions in 65C-6h mCNC, resulting from to the high degree of IEM modification. 65C-6h resulted in less mass residue (14.5 wt%) at 600 °C compared to the other samples. The mass residue was similar for the other CNCs at 30.5 wt% for umCNC, 30.8 wt% for 30C-6h, and 28.4 wt% for 50C-6h. Weight loss curves of other samples are provided in Figure 3.7. We did not observe significant changes in the weight loss profiles of both 50C and 65C samples when reaction time (2, 6, and 18 h) was compared.

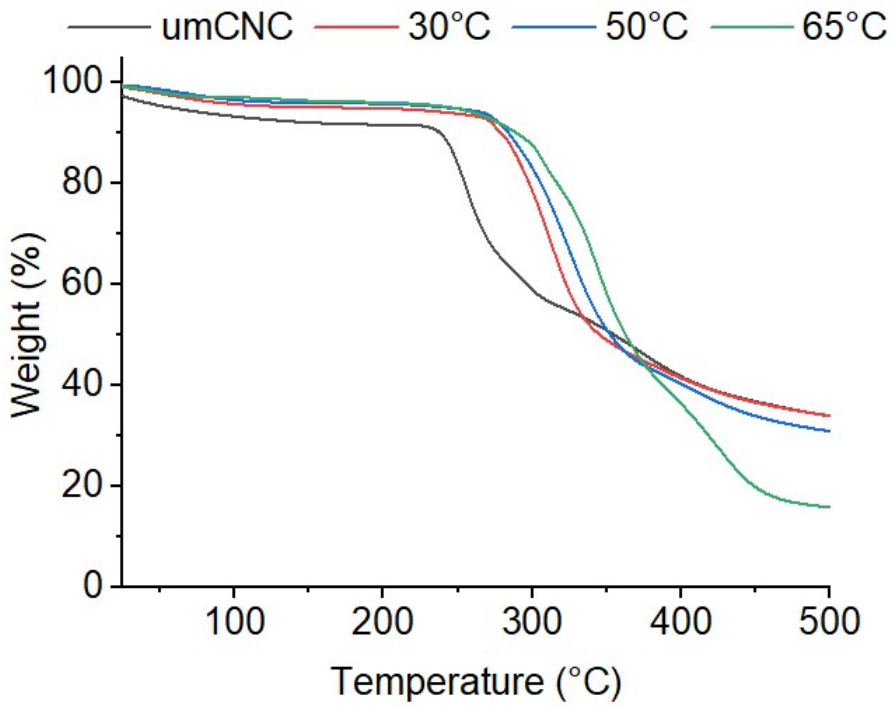

Figure 3.6: Weight loss curves of umCNC and mCNCs synthesized with 6 h reaction time at different temperatures.

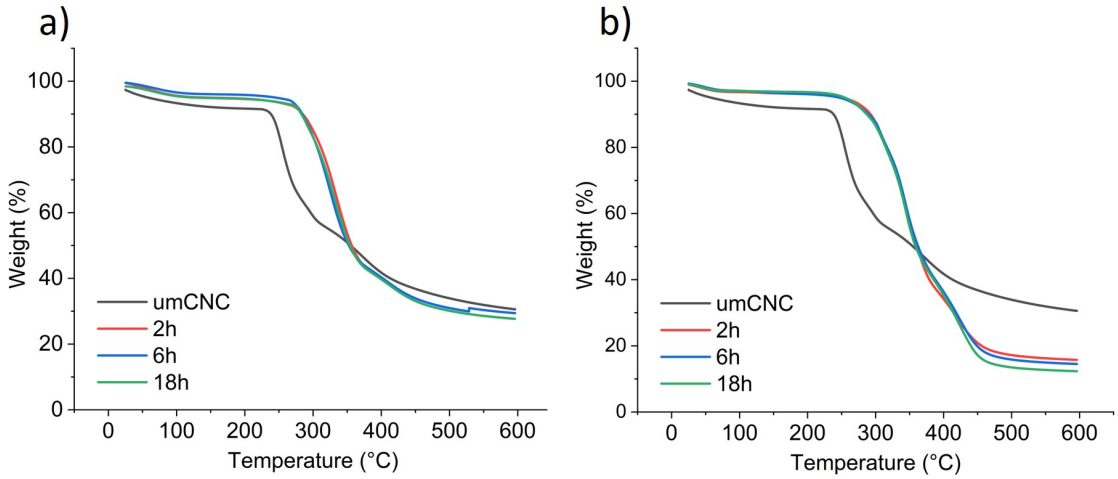

Figure 3.7: Weight loss curves of umCNC and mCNC samples synthesized at a) 50 °C and b) 65 °C as a function of reaction time.

We characterized the morphology of umCNC, 30C-6h, 50C-6h, and 65C-6h by AFM. The AFM amplitude images of CNCs are shown in Figure 3.8 with the average length (L) and height (H) measured from the images. The related particle size distributions are

provided in Figure 3.9. There was no noticeable difference between the dimensions of umCNC and mCNC-30C-6h. As the reaction temperature was increased, mCNCs became slightly shorter and thinner.

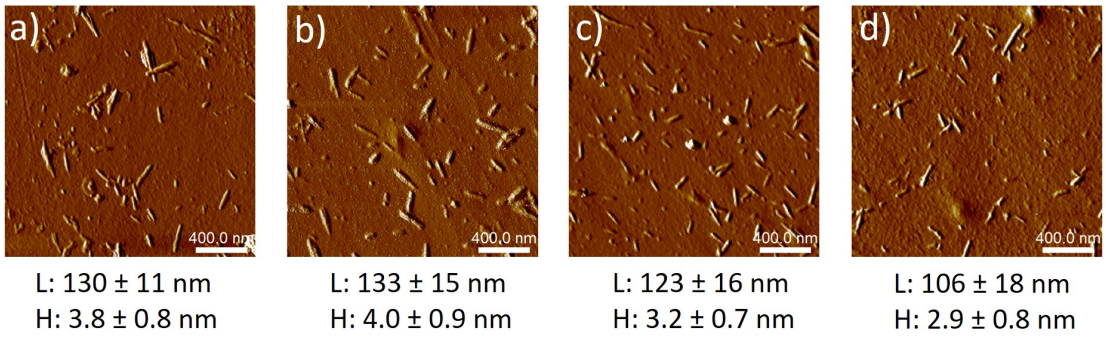

Figure 3.8: AFM amplitude images of a) umCNC and mCNCs synthesized with 6 h reaction time at b) 30 °C, c) 50 °C, d) 65 °C.

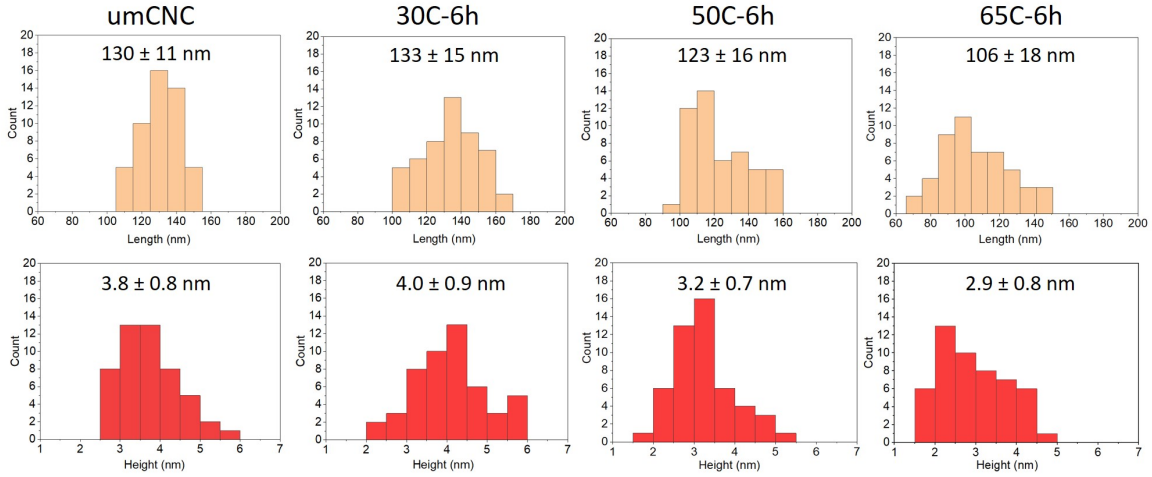

Figure 3.9: Length (top row) and height (bottom row) distributions of umCNC and mCNCs synthesized with 6 h reaction time at b) 30 °C, c) 50 °C, d) 65 °C.

We performed visual dispersion tests with freeze-dried umCNC and 65C-30m to evaluate the effect of the modification on the dispersion of CNCs in organic environments. The photographs of freeze-dried CNCs and their 1 wt% dispersions in the organic solvents are given in Figure 3.10. While umCNC dispersion with water and methanol remained stable during the observation time (18 h), mCNCs precipitated from water and methanol, leaving the solvent visually clear. Both umCNC and mCNC showed sedimentation in solvents less

polar than water and methanol: DMF, THF, toluene, and hexane. Figure 3.11 shows the dispersion of freeze-dried CNCs (1 wt%) in monomers that have different hydrophobicity. While umCNC precipitated in all monomers, mCNC dispersed well with HEMA and MAA, indicating the increase of mCNC's hydrophobicity. mCNC was partially dispersible in MMA and showed sedimentation in EA and BA.

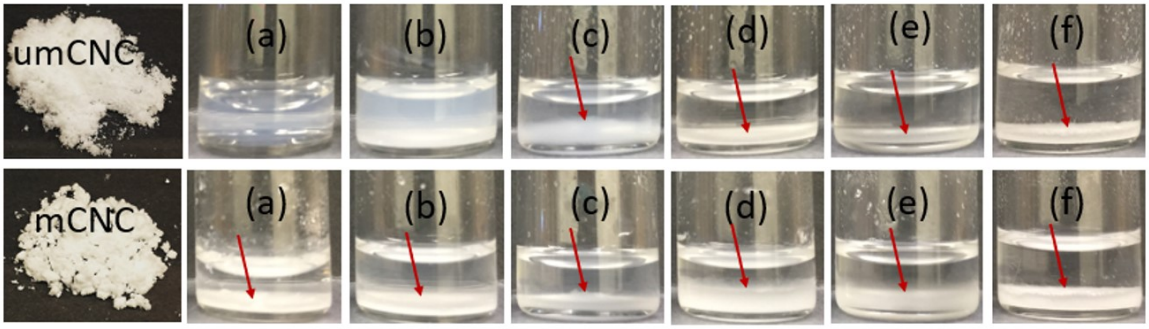

Figure 3.10: Photographs of 1 wt% dispersions of freeze-dried umCNC (top) and mCNC (bottom) in different solvents: (a) water, (b) methanol, (c) DMF, (d) THF, (e) toluene, (f) hexane. Photos were taken after overnight resting.

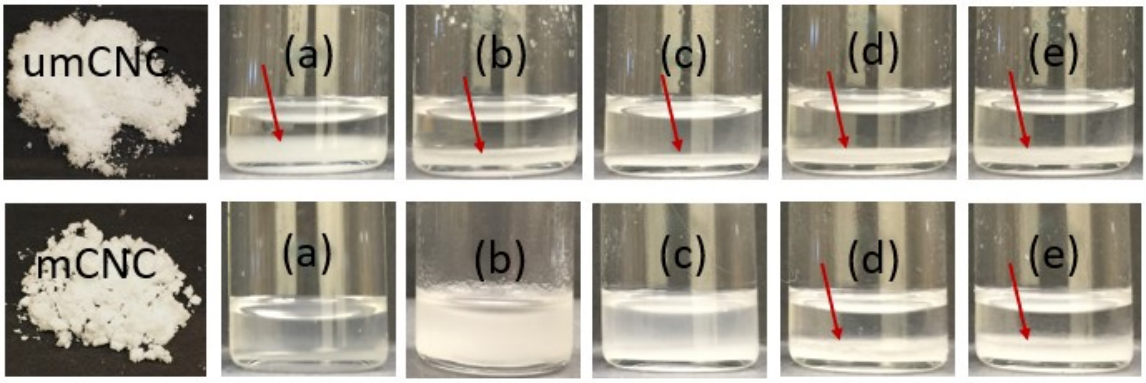

Figure 3.11: Photographs of 1 wt% dispersions of freeze-dried umCNC (top) and mCNC (bottom) in different monomers: (a) HEMA, (b) MAA, (c) MMA, (d) EA, (e) BA. Photos were taken after overnight resting.

3.3.2 *Grafting through* polymerization of mCNC

The 50C-2h mCNC sample was used for in situ solution polymerization with BA and MMA. We produced neat BA/MMA polymer, neat polymer-mCNC blend, and CNC/BA/

MMA copolymers from in situ polymerization with umCNC or mCNC. The CNCs were purified from the free polymers in the produced polymer solutions and were analyzed by FTIR and TGA.

The spectrum of purified umCNC in Figure 3.13a was similar to umCNC before the polymerization, consistent with the lack of free-radical polymerizable groups on the umCNC (Figure 3.12a). The spectrum of purified mCNC was consistent with the spectrum scanned before blending with the neat polymer (Figure 3.12b). We compared the chemical structure of mCNC separated from the blend sample and the gmCNC separated from mCNC/BA/MMA copolymer to assess grafting on mCNC. The mCNC showed C=C stretching at 1600 - 1700 cm^{-1} and carbonyl absorbance at 1700 cm^{-1} (highlighted in Figure 3.13a), whereas gmCNC did not have C=C stretching and displayed a higher carbonyl peak compared to the mCNC carbonyl absorbance. This comparison indicated the success of copolymerization between mCNC and acrylic monomers.

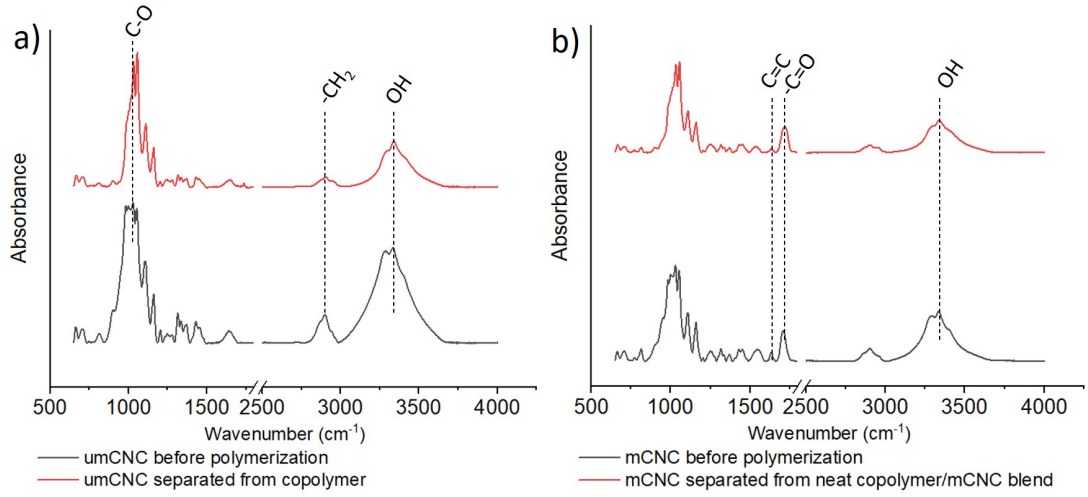

Figure 3.12: FTIR spectra of CNCs before and after the polymerization: a) umCNC and b) mCNC.

In Figure 3.13b, TGA results of the purified CNCs also indicated successful polymer grafting on the mCNC. Weight loss curves of the umCNC and mCNC were consistent with the previous TGA results in Figure 3.6. The degradation of gmCNC had a two-step weight

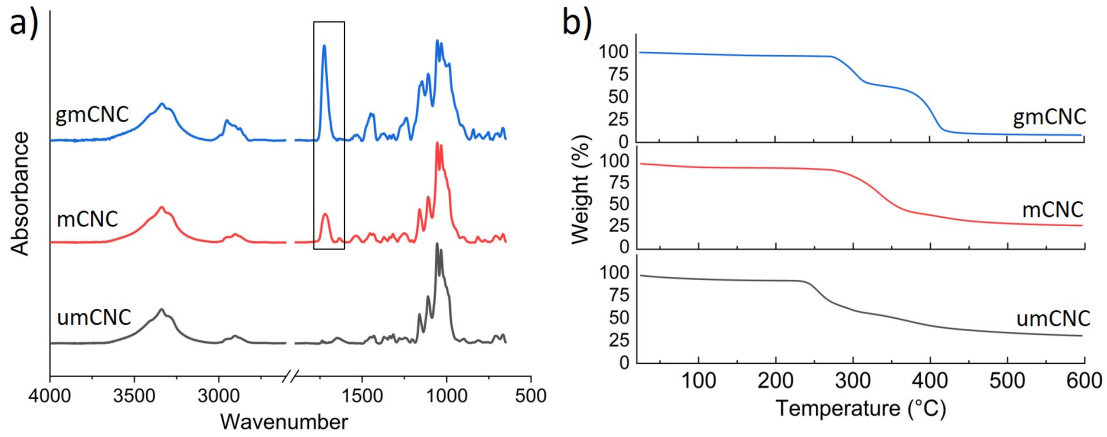

Figure 3.13: a) FTIR spectra and b) TGA weight loss of CNCs purified from the polymerization solution.

loss. The first step was associated with the cellulose component. The second step was due to the degradation of the polymer attached to CNC, as it began around 320 °C, close to the degradation onset of the neat polymer. We determined the amount of grafted BA/MMA polymer content to be 57.8 wt% of gmCNC, and the weight ratio of polymer to mCNC was 1.34.

The results of elemental analysis in Table 3.2 further confirmed the copolymerization of monomer functional groups carried by IEM on mCNC. N wt% in mCNC represents IEM attached to the CNC surface. The amount of IEM attached to the surface of CNC was determined to be 1.82 μmol/m^2. N percent composition was lower, and C composition was higher in gmCNC relative to mCNC due to the content of grafted polymers composed of C, H, and O. We determined the composition of MMA and BA in the grafted polymer as 45 wt% and 55 wt%, respectively, by using the elemental analysis results (in calculation section in Appendix B). The number average molecular weight (M_n) of attached polymer chains was calculated as $\sim$1110 g/mol based on the protocol reported by Zhang et al. [162] without chain cleavage. By using the polymer content obtained from TGA and the M_n we estimated, the grafting density was calculated around 0.47 chains/nm^2. Calculation of grafting density is given in Appendix B. Kedzior et al. [148] extensively reviewed

the existing literature of polymer-grafted CNC synthesis. According to the tables summarizing different grafting studied, the reported grafting densities are in the range of 0.02 – 4 chains/nm^2, depending on the grafting method, crosslinker chemistry, polymerization method, and parameters. The grafting densities obtained from *grafting through* polymerizations are similar to the densities obtained from *grafting to* technique, but usually lower than the densities achieved in *grafting from* method [87].

Table 3.2: Elemental weight percentage composition of the purified CNCs from the copolymers.

	Elements wt% $\pm$ 0.3 wt%				
	C	H	N	S	O [a]
umCNC	41.7	6.2	0	1.02	51.1
mCNC	44.2	6.1	1.7	0.96	46.9
gmCNC	52.8	7.3	0.7	0.38	38.9

[a]Values are the calculated content by subtracting the sum of C, H, N, and S from 100%.

3.3.3 Dispersion of CNCs in the acrylic polymer matrix

To assess the dispersion of gmCNC in the acrylic polymer matrix compared to umCNC, we dissolved the precipitated polymers from solution polymerizations in DMF and cast three acrylic (BA/MMA) polymer films: (1) neat acrylic polymer, (2) umCNC/acrylic, and (3) gmCNC/acrylic copolymer. The characterization results of the free polymers such as composition, molecular weight, polydispersity and T_g are given in Table B.2.

Figure 3.15a shows the photographs of polymer solutions (5 wt%) and Figure 3.15b shows their cast films. The concentration of CNC in the dry polymer was adjusted to be 6 wt% (surface polymers in gmCNC were not included in this concentration) and confirmed by TGA (Figure 3.14). The polymer solution containing umCNC looked hazy compared to neat and gmCNC/acrylic polymer solutions (Figure 3.15a). This observation was supported by the light transmittance measurement of the resulting films in Figure 3.15c. The umCNC/acrylic film has a lower light transmittance compared to other films, suggesting

less homogeneous dispersion of umCNC relative to gmCNC in the acrylic polymer matrix. PLM images of the polymer films shown in Figure 3.15d confirmed that grafting on the CNC enhanced the dispersion of the particles in the acrylic polymer. While gmCNC/acrylic shows almost no birefringence as the neat polymer, the umCNC/acrylic film has a birefringence due to the aggregation of umCNCs.

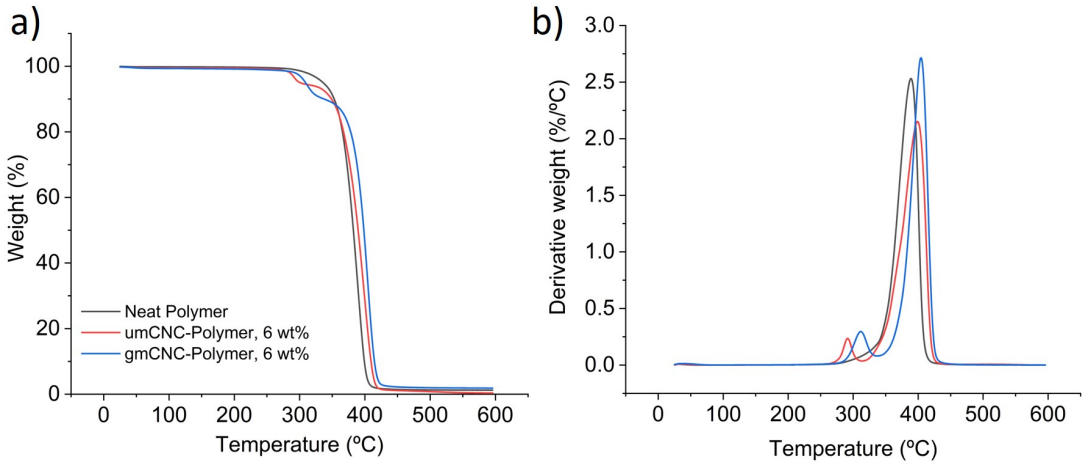

Figure 3.14: a) weight loss and b) derivative weight loss curves of neat acrylic and CNC/acrylic polymer films.

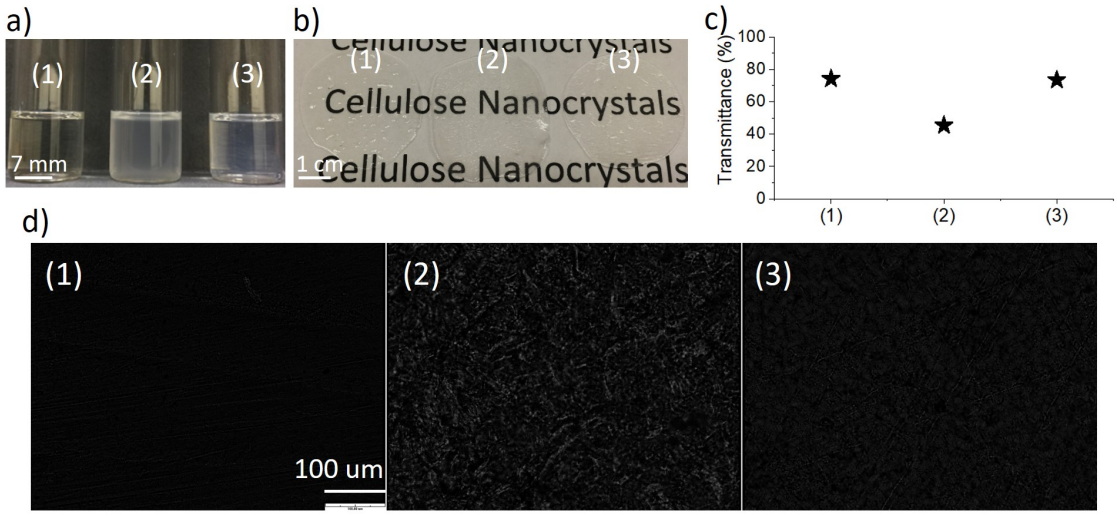

Figure 3.15: a) photographs of dissolved copolymers (5 wt%) in DMF, b) solution-cast films from polymer/DMF solutions, c) light transmittance of the polymer films at 550 nm, d) PLM images of the films.

We characterized the strength and hardness of the polymer films to understand how the extent of CNC dispersion in the polymer matrix influences the reinforcement performance of the CNC. The increased dispersion of the gmCNC in the acrylic polymer was associated with enhanced UTS and hardness compared to the umCNC/acrylic films (Figure 3.16). The gmCNC improved the tensile strength of the neat polymer films from 6.9 $\pm$ 1.0 MPa to 13.8 $\pm$ 1.2 MPa, whereas umCNC did not result in a significant difference (t-test with α=0.05) in the tensile strength. The indentation hardness of the neat film was enhanced by gmCNC from 36.1 $\pm$ 6 MPa to 55.3 $\pm$ 5 MPa, whereas umCNC did not influence the hardness. However, the addition of umCNC and mCNC both decreased the strain at break to about 42% and 31%, respectively, from the strain of neat polymer film, 80%.

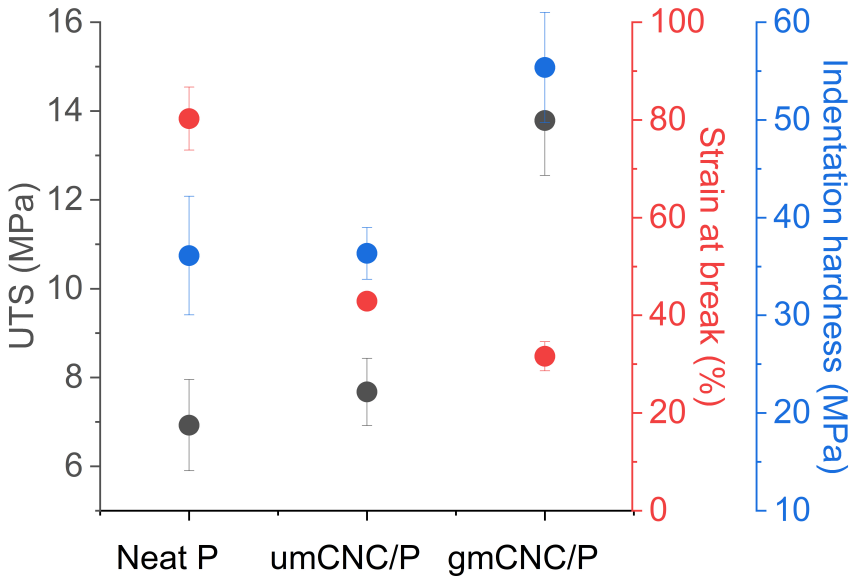

Figure 3.16: ● - UTS (MPa), ● - strain at break (%) and ● - nanoindentation hardness (MPa) of copolymer films.

While the decrease in elongation was expected for the composites relative to the neat polymer, the decrease in the elongation value for the composite containing the gmCNCs relative to the composite containing umCNCs was unexpected since the dispersion of CNCs was expected to be more homogeneous after modification. However, the values of T_g sug-

gested that the polymer network was stiffer with the addition of gmCNC, which would lead to a more brittle response, and the effects may be enhanced because the values of T_g were close to ambient temperature. The T_g of the composite containing the gmCNCs was slightly higher than the other materials. We measured the T_g of the neat acrylic film as 26 $\pm$ 1 °C. The umCNC/acrylic film and gmCNC/acrylic films resulted in T_g as 27 $\pm$ 1 °C and 29 $\pm$ 1 °C, respectively (Table B.2). The property trends observed here have also been reported in previous studies [163, 164]. Zhang et al. [163] grafted CNCs with poly(methyl methacrylate) (PMMA) and added them into the copolymer of poly(butyl and methyl acrylate) (PBA-co-PMMA) solution in THF. The mechanical testing of their solvent-cast films showed that loading 10 wt% grafted CNC improved the tensile strength of the neat acrylic film (2.6 MPa) to around 8.2 MPa; however, the strain at break was reduced from about 2100% to 754%. When 10 wt% umCNC was loaded, the strain at break was slightly higher (1100%) compared to the loading of grafted CNC; however, no noticeable change was observed in the tensile strength of (PBA-co-PMMA) films. Yu et al. [164] functionalized the CNCs with an initiator and grafted (PBA-co-PMMA) onto the surface of CNCs by surface-initiated atom transfer radical polymerization (SI-ATRP). The team prepared composite films of (PBA-co-PMMA) matrix containing (PBA-co-PMMA)-grafted CNCs and performed mechanical testing. When the concentration of CNC in the acrylic matrix was 2.15 wt%, the tensile strength increased to around 11.4 MPa from 5.5 MPa of neat (PBA-co-PMMA) film, whereas the strain at break decreased with the loading of grafted CNC from 760% (in neat film) to approximately 295%. Overall, polymer grafting enhanced compatibility between CNCs and the acrylic matrix and affected the network structure, resulting in improvement of the tensile strength and hardness of the acrylic film relative to neat and umCNC-loaded films.

3.4 Conclusions

The surface of CNCs was successfully modified via a urethanization route by using a difunctional molecule carrying isocyanate and a vinyl (acrylic) monomer functional groups, IEM. We studied the effects of urethanization temperature and time on the degree of modification, crystallinity and morphology of the CNCs. The results showed that the degree of modification is a strong and increasing function of reaction temperature over the range studied. On the other hand, the reaction time at 50 °C rendered only a slight improvement in the degree of modification by IEM over the time range studied. However, the combination of the highest temperature (65 °C) and longest time of reaction altered the crystal morphology resulting in shorter, thinner, and less crystalline CNCs. The shortest time of reaction (30 min) at 65 °C resulted in surface hydroxyl conversion of 60.1 $\pm$ 6% and crystallinity of 84%. This study revealed that tuning the extent of modification and crystallinity in mCNCs can be achieved by varying reaction conditions. Via this approach, one can determine a modification reaction condition resulting in a mCNC having a specific degree of modification, hydrophilicity and crystallinity. These results can inspire researchers working on CNC modifications with various modifiers to optimize modification procedures.

The successful copolymerization of vinyl groups on mCNC was confirmed with FTIR and TGA. We determined the amount of grafted polymer on the mCNC as 57.8 wt% and the grafting density was estimated around 0.47 chains/nm^2. The gmCNC dispersed better in a BA/MMA copolymer matrix compared to umCNC, as observed with light transmittance measurement and PLM. The better dispersion of gmCNC resulted in approximately 100% improvement in the tensile strength and about 53% enhancement in the hardness of the acrylic films, whereas the umCNCs resulted in improvements to tensile strength and hardness of only 12% and 0.7% relative to the neat acrylic polymer, respectively. This study demonstrated a versatile modification scheme that can be used with various monomers for polymer grafting applications to increase compatibility with polymer matrices. The results

from different reaction temperature and time conditions showed the tunability of the vinyl groups on the mCNC and consequently the grafted polymer. Having control of the degree of modification allows adjusting the hydroxyl content remaining on mCNCs and gmCNCs. Overall, the modification technique presented here can be useful guide for future studies investigating the incorporation of CNCs into polymer matrices.

CHAPTER 4

ENCAPSULATION OF CELLULOSE NANOCRYSTALS INTO ACRYLIC LATEX PARTICLES VIA MINIEMULSION POLYMERIZATION

This chapter explores the incorporation of CNCs into the polymer phase of latex via miniemulsion polymerization. Unmodified, acryloyl-modified and acrylic polymer-grafted CNCs were introduced into butyl acrylate and methyl methacrylate monomers to be used in the monomer phase of miniemulsion polymerization (Figure 4.1). Appendix C presents the supporting information for this chapter.

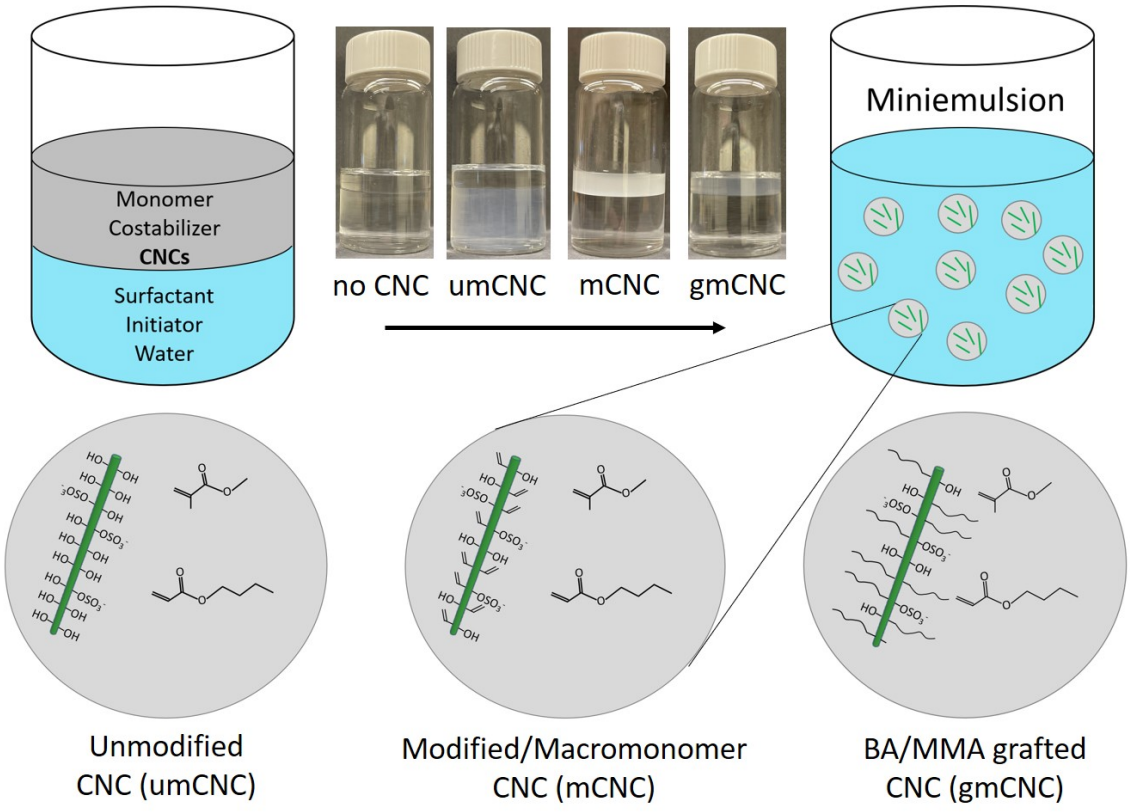

Figure 4.1: Schematic showing the preparation of miniemulsions with different types of CNCs (unmodified, modified, and polymer-grafted).

4.1 Introduction

Polymer colloids are essential precursors used in various industrial applications. These colloid systems have been used in the paper, leather, and construction industries and in applications for printing inks, coatings (decorative, protective, automotive), and adhesives [165]. Interest in the research and applications of waterborne polymer colloids has increased in the last decades, as opposed to traditional solventborne technologies, since market and regulatory trends are moving more towards eco-friendly materials [166].

An aqueous polymer colloid or a latex is a dispersion of submicron polymer particles in water. The most commonly used method to produce latexes is conventional emulsion polymerization. Emulsion polymerization is a heterogeneous free radical polymerization where the monomer is initially contained in droplets stabilized by a colloidal stabilizer (typically surfactant) in water. Surfactants used above the critical micelle concentration (CMC) stabilize the monomer droplets ($\sim$10 μm) and also form micelles ($\sim$10 nm) in the aqueous phase [167]. Emulsion polymerization employs monomers having a slight water solubility and a water-soluble initiator to initiate the polymerization in the aqueous phase. Monomers diffuse from relatively larger monomer droplets to the aqueous phase to supply the polymerization that occurs in the continuous aqueous phase (homogeneous nucleation), in monomer-swollen micelles (micellar nucleation), or (very slightly) in the monomer droplets (droplet nucleation).

Miniemulsion polymerization is another route to synthesize latexes. Both conventional emulsion polymerization and miniemulsion polymerization result in polymer particles ranging from 50 to 500 nm; however, the mechanism for particle growth differs. Miniemulsions contain smaller ($<$1 μm) monomer droplets obtained by a high shear emulsification step and use of a costabilizer to prevent Ostwald ripening. A low surfactant concentration is used so that no micelles form in the aqueous phase after the emulsification step. Reducing the droplet sizes increases the surface area for polymerization, enabling

droplet nucleation to become the dominant mechanism for the growth of particles. The identity of droplets is maintained with an effective surfactant and costabilizer system during the polymerization. Whereas surfactants stabilize droplets against coalescence as in emulsion polymerization, costabilizer (e.g., a long chain alkane or alcohol) retards monomer diffusion from small to large droplets (Ostwald ripening) in miniemulsions [168].

Miniemulsion polymerization is a favorable process for the encapsulation of small molecules and solids (fillers) in a polymer matrix to produce latexes with hybrid polymer particles [169]. Unlike in emulsion polymerization, the droplets act as *nanoreactors* for the polymerization, promoting the homogeneous distribution of fillers in the polymer particles. The droplet size can be controlled with the surfactant/costabilizer system, and the size is not affected by the polymerization parameters [170]. Research interest in producing latexes containing hybrid particles has been increased since the early 2000s. The benefit offered by encapsulation processes varies depending on the nature of encapsulated material and the requirements of the application. Organic or inorganic materials have been incorporated into polymeric particles, for example, to protect the material from the environment, or to prevent the material from agglomerating in the continuous phase, or to inhibit the aggregation of the material during film formation, providing homogeneous distribution of the filler over the polymer film. Furthermore, in biomedical applications, encapsulation allows control over the release of drugs and curing agents [171].

Many researchers have studied the miniemulsion technique to encapsulate inorganic nanoparticles, including carbon nanotubes [172], carbon black [173], silica [174, 175], titanium dioxide [176], iron oxide [177], and clay platelets [178]. Organic materials such as dyes and functional organic molecules have been encapsulated via miniemulsion polymerization [179]. Many of the nanoparticle classes studied for encapsulation are hydrophilic. Therefore, surface functionalization has been performed for the hydrophilic nanoparticles to decrease their hydrophilicity and increase compatibility with monomers before the miniemulsification step.

Recently, an organic reinforcing phase that has attracted attention for encapsulation is cellulose nanocrystals (CNCs). CNCs are stiff nanomaterials derived from cellulose present in the cell wall of various plants. CNCs with the abundance of hydroxyl groups are typically extracted by sulfuric acid hydrolysis of cellulose fibers. Due to their renewable nature, crystallinity and high specific strength, CNCs have been incorporated into latexes to enhance the mechanical properties of the resulting films after the film formation of polymer particles [88, 102]. However, because of their hydrophilicity, CNCs have been added to the aqueous phase of latexes, and are either remain in the aqueous phase or adsorb on the surface of the particles. When CNCs are added to the aqueous phase of latex, CNC aggregates form in the polymer matrix, after the latex particles coalesce around the CNCs during film formation [88, 102]. Encapsulating CNCs inside the latex particles could alleviate CNC aggregation in the polymer film (Figure 4.2) and improve the mechanical properties.

With this idea, only two publications reported incorporating CNCs into polymer particles through emulsion or miniemulsion methods. The first study, by Kedzior et al. [180], demonstrated that surface-functionalized CNCs could be encapsulated inside poly(methyl methacrylate) (PMMA) latex particles. CNCs were grafted with poly(butyl acrylate) (PBA) by using surface-initiated atom transfer radical polymerization (SI-ATRP) and dispersed in methyl methacrylate (MMA) before the polymerization. The team performed a miniemulsion polymerization without using a costabilizer. The absence of costabilizer may shift the particle growth mechanism from that of miniemulsion polymerization to microsuspension polymerization. The second study, by Yu et al. [181], functionalized CNCs with a silane coupling agent to integrate them into an acrylic pressure sensitive adhesive (PSA) system. A semi-continuous seeding emulsion polymerization was performed, and CNCs were found mainly anchored on the surface of acrylic particles. The resulting particle morphology improved the tack and peel strength of PSAs compared to the addition of native CNCs.

In this work, we explored the incorporation of surface functionalized CNCs into poly(BA-

MMA) copolymer latex particles with a miniemulsion polymerization technique. We modified the CNC surface by using isocyanatoethyl methacrylate (IEM) molecules and grafted poly(BA-MMA) copolymer via a *grafting through* [182] approach. We identified the challenges in encapsulating CNCs inside acrylic polymer particles and assessed the limitations of this encapsulating approach.

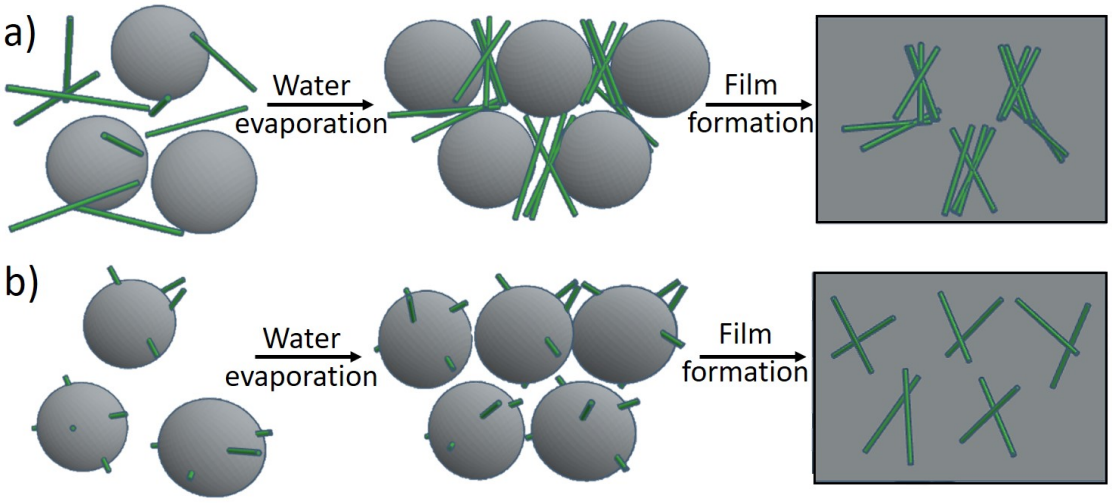

Figure 4.2: Film formation process of waterborne polymeric particles with CNC located a) in the aqueous phase b) inside the latex particles.

4.2 Experimental section

4.2.1 Materials

Freeze-dried CNCs (with 1.06 wt% sulfur) from the US Forest Service Forest Products Laboratory, Madison, WI were used as received. Dimethyl sulfoxide (DMSO, extra dry, $\geq$ 99.8%) was supplied in the 100 ml AcroSeal™ bottle from ACROS Organics. 2-isocyanatoethyl methacrylate (IEM, at >98% purity), dibutyltin dilaurate (DBTDL), methyl methacrylate (MMA - 99%, stabilized with MEHQ), benzoyl peroxide (BPO, Luperox® A98), inhibitor remover column, toluene (ACS, 99.5%), dimethylformamide (DMF, anhydrous, 99.8%), potassium persulfate (KPS, ACS reagent, $\geq$ 99%), sodium bicarbonate (ACS reagent, $\geq$ 99.7%), and hexadecane (HD - ReagentPlus®, 99%) were purchased from

Sigma-Aldrich. Butyl acrylate (BA - >99%, stabilized with MEHQ) was obtained from TCI America. Sodium dodecyl benzene sulfonate (SDBS, POLYSTEP® A-16-22) was provided by Dow Coating Materials, The Dow Chemical Company, Collegeville, PA. Methyl methacrylate and butyl acrylate were passed through an inhibitor remover column (filled with basic alumina) before the polymerization.

4.2.2 Preparation of modified CNC (mCNC)

A sample of 0.1 g of unmodified CNCs (umCNCs) was mixed with 11 g anhydrous DMSO in a septum-sealed vial. The vial was clamped inside a bath sonicator (2510 Branson), and the mixture was sonicated for 30 min to promote the dispersion of umCNCs in DMSO. An empty two-neck round bottom flask was equipped with a magnetic stirrer, rubber stoppers, and needles punched through rubber septa on two necks. Then, the flask was submerged in an oil bath at 65 °C and a nitrogen stream was purged through the flask for 20 min to flush out oxygen. The bath-sonicated umCNC/DMSO dispersion was transferred from the septum-sealed vial to the heated reaction flask by using a syringe and a needle. In a separate vial, IEM and DBTDL were mixed and quickly added dropwise to the stirring umCNC/DMSO dispersion. The concentrations of IEM and DBTDL in DMSO were 5.7 wt% and 0.3 wt%, respectively. The mixture of umCNC/DMSO/IEM/DBTDL was magnetically stirred at 65 °C for 30 min under a nitrogen flow. The product dispersion was first mixed with toluene and centrifuged at 3000 rpm for 10 min to precipitate the modified CNC (mCNC). Then, the precipitated mCNC was mixed with acetone and centrifuged at 3000 rpm for 10 min (repeated 2 times) for purification. The collected mCNC was flash-frozen in liquid nitrogen and dried through lyophilization (Labconco FreeZone 4.5 L, with pressure $<$ 0.2 mbar, -55 °C of coil temperature) for 2 days.

4.2.3 Preparation of polymer-grafted modified CNC (gmCNC)

The mCNC was produced with the procedure explained in the previous section. Before the lyophilization step, the precipitated mCNC from the reaction medium was dispersed in 6 g of DMF. The mixture was transferred into a 50 ml round bottom flask. Benzoyl peroxide (5 mg) as the initiator, BA (1 g) and MMA (1 g) were added to the mixture. The flask was submerged into an oil bath and purged with a nitrogen flow for 15 min to remove oxygen. To facilitate polymerization, the mixture in the flask was stirred for 6 h in an oil bath at 70 °C. After the polymerization, the product solution in the flask were mixed with toluene and centrifuged to remove the free polymer in the solution. The polymer-grafted mCNCs (gmCNCs) settled to the bottom of the centrifuge tube because of density difference between gmCNC and free polymer in toluene. The purified gmCNC was recovered from the centrifuge tubes and dried in vacuum at 70 °C for 24 h.

4.2.4 Preparation of acrylic latexes

Controlling the particle size of the latex

Acrylic latexes were synthesized via miniemulsion polymerization. Aqueous and monomer phases of the miniemulsion were prepared based on the recipe given in Table 4.1. The monomer phase consisted of BA/MMA monomers and HD (the most common costabilizer in miniemulsion polymerization). For the aqueous phase, sodium carbonate (10 mM) and SDBS surfactant were mixed with ultra-pure water. To control the particle size in the latex as a function of surfactant concentration, neat latexes were prepared by using different amounts of SDBS in the aqueous phase. The initiator solution was prepared by dissolving the specified amount of KPS (10 mM) in 0.8 g ultra-pure water. The monomer phase was added to the aqueous phase, and the mixture was stirred for 20 min for pre-emulsification. Then, the mixture was ultrasonicated by using a probe sonicator (Q500, QSonica Ultrasonic Processor with a maximum power of 500 W) at 60% amplitude for 3 min in an ice bath.

The miniemulsion was transferred to a 25 ml two-neck round bottom flask equipped with a magnetic stir bar. The flask was submerged in an oil bath and sealed with a condenser and a rubber septum. A nitrogen gas flow was given through the rubber septum, and the condenser was connected to a recirculating bath (VWR) with a coolant temperature set to 2 °C (Figure 4.3). The miniemulsion in the flask was bubbled and flushed with nitrogen gas flow for 10 min with the oil bath at ambient temperature. The oil bath temperature was set to 70 °C and the polymerization was allowed to progress for 7 h after injecting the initiator solution.

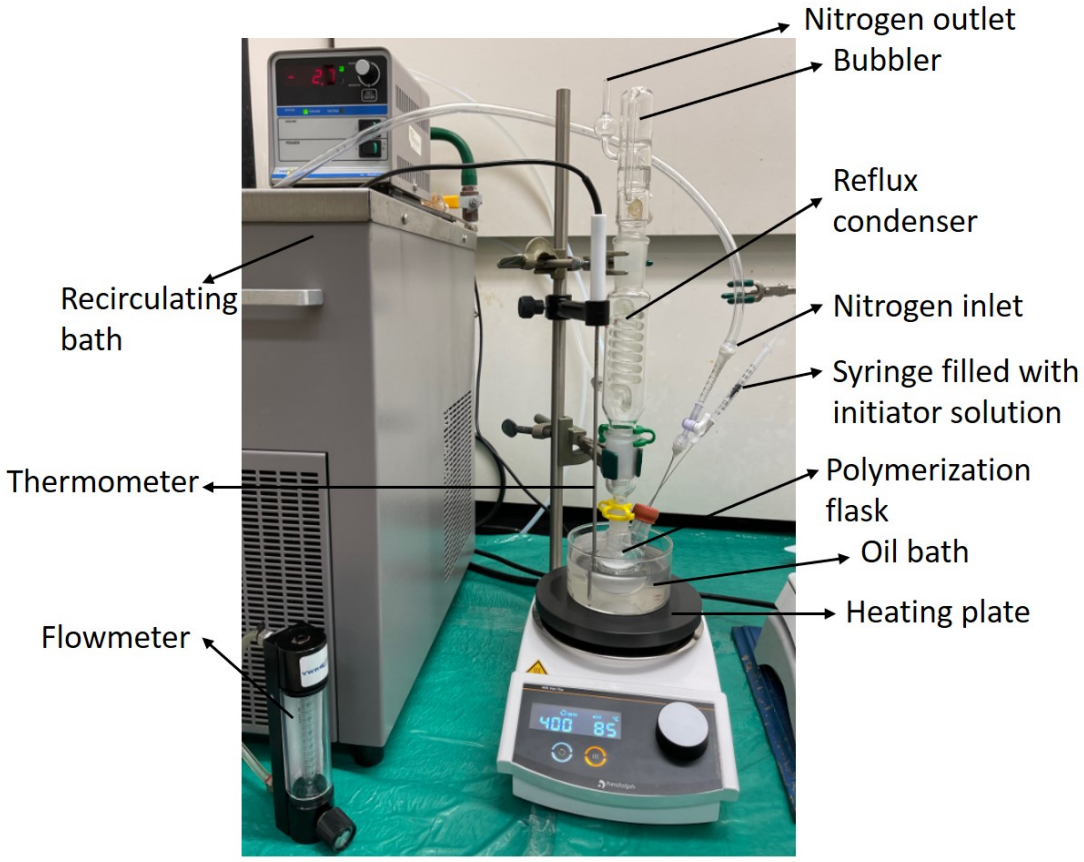

Figure 4.3: Set-up for miniemulsion polymerization.

Table 4.1: Recipe for the miniemulsion polymerization of BA/MMA latexes.

	Components	Mass and Concentration
Monomer phase	BA	1 g
	MMA	1 g
	HD	0.08 g
Aqueous phase	Water	8 g
	SDBS (10 wt% aqueous solution)	0.1 – 0.9 g (0.81 – 7.28 mM)
	KPS	0.02 g (10 mM)
	Sodium bicarbonate	Same as KPS

Incorporating CNCs into the latex

The miniemulsion polymerization procedure stated above was used with some changes to synthesize the latexes with CNCs. First, CNCs (umCNC, mCNC, or gmCNC) were dispersed in the monomer phase as either 0.5 wt% or 1 wt% of total monomer mass. Second, two different surfactant concentrations (0.81 mM and 2.42 mM) were selected to synthesize the latexes since these surfactant concentrations resulted in latex particle sizes larger than the average length of CNCs. Third, we increased the initiator concentration and polymerization temperature and decreased the polymerization time in order to improve the monomer conversion and minimize the coagulation. Also, the initiator solution was injected in two steps. Both the concentration of KPS and sodium carbonate were 20 mM in the aqueous phase instead of 10 mM. Half of the initiator solution was injected when the oil bath reached 85 °C and polymerization was allowed to proceed for an hour. Then, the rest of the initiator solution was injected, and polymerization was carried out for two more hours. Neat latexes were also synthesized with the same polymerization conditions for comparison. After the polymerization, the latexes were passed through a 200-mesh strainer. The latex coagulation was collected and dried for weight measurement. PTFE evaporating dishes having a diameter of 38 mm were used to cast the latex films (Figure C.1). 1.5 ml latex was added to the dish and vacuum-dried at 70 °C for 24 h. The thickness of the latex films was 200 $\pm$ 50 μm.

4.2.5 Characterization

The solid content of the latexes was determined gravimetrically, and monomer conversions were calculated by using equation (4.1) where C is the measured monomer conversion, $S_{measured}$ is the measured percent solids in the latex, $S_{non-polymer}$ is the percent non-polymer solids calculated from the recipe, and S_{100} is the percent total solids calculated from the recipe assuming 100% conversion.

$$C(\%) = 100 \times \frac{S_{measured} - S_{non-polymer}}{S_{100} - S_{non-polymer}} \tag{4.1}$$

The pH of the latexes was measured by using a Mettler Toledo Seven2Go pH/mV meter equipped with Semi-Micro L pH electrode.

Zeta potential and average particle size of latexes were measured by using a Malvern Zetasizer Nano ZS90. The latexes were diluted with DI water to 0.025 wt% for both zeta potential and size measurements. The average of three measurements was reported.

A Ramé-Hart goniometer was used to perform water contact angle measurements of CNC samples and surface tension measurements of the latexes. For contact angle samples, 1 wt% suspensions of umCNC, mCNC and gmCNC were prepared in DMSO, and the CNC suspensions were drop-cast on glass slides and vacuum-dried (60 °C - 24 h). Five deionized water droplets (10 μl) were placed on each sample. The water contact angles were measured 60 s after the water droplets were dispensed. For surface tension measurements, 1 ml of latex was withdrawn by using a microsyringe with a stainless-steel needle. The microsyringe was mounted to the instruments and surface tension was measured from a pendant drop of the latex.

ATR-FTIR spectroscopy was performed on CNC samples and latex films. A Nicolet 6700 FTIR spectrometer equipped with a diamond crystal single bound ATR attachment was used to obtain spectra with a resolution of 4 cm^{-1} and 64 scans at a range of 4000 – 650 cm^{-1}. The spectra were normalized at the 1060 cm^{-1} peak associated with the C-O vibration

of the third carbon.

Elemental analysis was carried out by Atlantic Microlab (Norcross, GA) with combustion method using automatic analyzers. C, H, N and S contents of the CNC samples and the latex samples were analyzed. The results were used to calculate the degree of substitution of IEM in mCNC, grafting density, and the copolymer composition of the grafted polymer in gmCNC.

TGA (Q50, TA Instruments) was performed for thermal stabilities and degradation patterns of CNC samples. The samples were heated from 25 °C to 600 °C under nitrogen atmosphere with a heating rate of 10 °C/min.

The morphology of CNCs and latex particles were imaged by AFM (Bruker Dimension Icon) in tapping mode. umCNC and mCNC dispersions in DMSO at a concentration of 1 wt% were diluted to approximately 0.001 wt% and drop-cast onto a piranha etched silicon wafer. A probe (HQ:NSC14/No Al-15) with a resonance frequency of 160 kHz and a force constant of 5 N/m was used to capture the images. We used Gwyddion software to analyze the height images for the size distributions of CNCs. The length and height of 50 isolated particles were measured.

Partition tests were performed to study the preference of CNCs to aqueous phase or monomer phase. Monomer/water mixtures were prepared in 7 ml glass vials. The monomer — water ratio was 1:4 as used in miniemulsion polymerizations. Monomers containing 50 wt% BA and 50 wt% MMA were mixed with different types of CNCs (umCNC, mCNC, and gmCNC) at a concentration of 1 wt% in separate vials. DI water was added to the monomer mixtures and partition of CNCs was observed during 24 h as compared to the case where we mixed only monomers with water as a reference.

We conducted DSC (Discovery DSC, TA instruments) under a nitrogen gas purge to determine glass transition temperatures (T_g) of the latex films. The samples were first equilibrated at -20 °C and followed by a heat/cool/heat cycle with a heating/cooling rate of 10 °C/min between -20 °C and 150 °C. The isothermal steps were applied for 2 min at the

top and the bottom temperatures. The midpoint T_g was measured from the second heating curve of each sample. We performed three measurements per sample and reported average values with the standard deviations.

The viscosity of the latexes was measured at room temperature with a Physica MCR 501 (Anton Paar) rheometer. The CP40 cone at a 100 s^{-1} shear rate was used in the measurement.

The latex films were tested with the HTMECH instrument [107] to determine the ultimate tensile strength (UTS) and strain at break. The films were deformed biaxially with a 1.25 mm diameter hemispherical indenter normal to the film plane at a speed of 10 mm/s until rupture occurred. We performed five measurements per sample and presented average values with the standard deviations.

Dynamic mechanical analysis (DMA – Mettler Toledo DMA/SDTA861) was performed to determine the storage and loss moduli of the latex films. Latex samples were cut into rectangular samples about 20 mm long and 3 mm wide. The testing length was 9 mm, and the samples were tested in tension at room temperature within the linear response region of strain. The moduli of the samples were analyzed using a frequency sweep method from 0.1 to 100 Hz.

4.3 Results and discussion

4.3.1 Characterization of CNCs

The surface functionalization of mCNC and gmCNC was confirmed by ATR-FTIR spectroscopy (Figure 4.4a), water contact angle measurements (Figure 4.4b), elemental analysis, and TGA (Figure 4.5). In Figure 4.4a, FTIR spectra of the CNC samples displayed absorbances at the bands characteristic of cellulose [109]. The wide peak at 3000-3700 cm^{-1} corresponded to stretching vibration bands of the hydroxyl bonds of the hydroxyl groups. The peak at 2900 cm^{-1} was associated with the stretching vibration of C-H bond, whereas the peaks at 1110 cm^{-1}, 1060 cm^{-1}, and 1035 cm^{-1} showed the absorbances due to

the vibrations of the C-O bond of carbons 2, 3, and 6. The spectra of mCNC and gmCNC overall kept the identity of the CNC spectra but showed new peaks and changes in the intensities of some absorbances. In the spectrum of mCNC, new peaks at around 1700 cm^{-1} and 1630 cm^{-1} corresponded to C=O and C=C groups, implying the attachment of IEM molecules to the surface of CNCs. Also, mCNC displayed a lower hydroxyl absorbance compared to umCNC. The changes in the spectrum of gmCNC compared to the spectrum of mCNC verified the grafting of BA and MMA monomers. We noted higher absorbances for C=O group at 1700 cm^{-1} and C-O group at 1140 cm^{-1} due to ester groups in the acrylic polymer grafts. Also, the absorbance at 2900 cm^{-1} for alkane C-H stretching was higher in the spectra of gmCNC because of C-H bonds in the attached polymer chains. Furthermore, we did not observe the peak at 1630 cm^{-1} due to C=C.

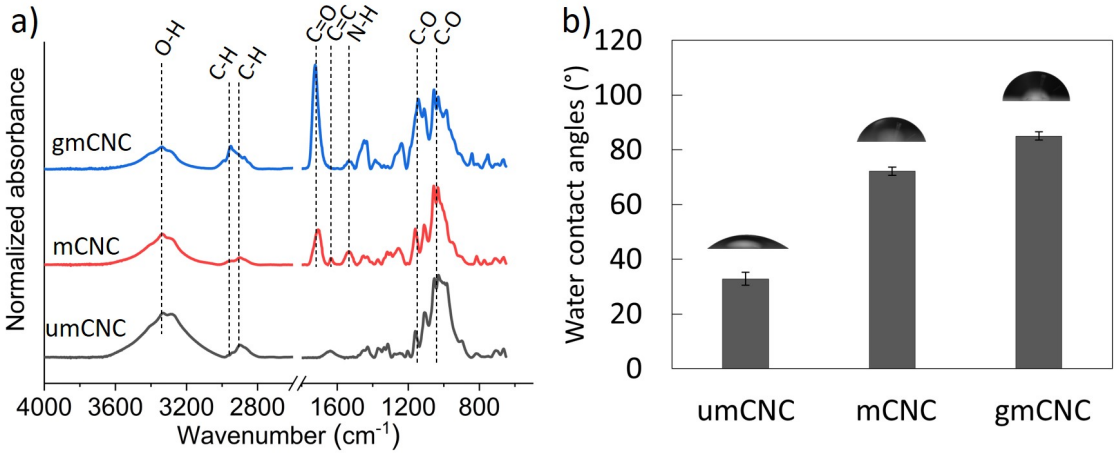

Figure 4.4: a) FTIR spectra and b) water contact angle measurements of umCNC, mCNC, and gmCNC.

The water contact angles measured on the CNC films were used to assess the changes in the hydrophilicity of CNCs after the surface modifications. Figure 4.4b shows the water contact angles on umCNC, mCNC, and gmCNC films. mCNC has reduced hydrophilicity with a contact angle of $72 \pm 1°$ compared to umCNC with a contact angle of $33 \pm 2°$. This change was expected since the portion of the surface hydroxyls on umCNC reacted with IEM and formed urethane linkages. The water contact angle of gmCNC was measured as

85 $\pm$ 2°, higher than the contact angle of mCNC. The further reduction in hydrophilicity of the gmCNC indicates the presence of grafted hydrophobic polymer on the surface of mCNCs.

In Figure 4.5, weight loss curves and derivative weight loss curves of CNCs also suggested the success of both surface functionalization on mCNC and gmCNC. The umCNC lost weight in two major steps. The outer layer of umCNCs with sulfate groups began to degrade around 270 °C and this event was followed by the slower degradation of the crystal interior. The mCNC began to lose weight at around 295 °C, later than the degradation onset of umCNCs. The onset of degradation for mCNCs increased due to covalently attached IEM molecules on the surface CNCs, which was consistent with previous isocyanate modification reports [146, 147]. The mCNC had an additional degradation event in the temperature range of 310-370 °C likely due to the urethane linkages formed between CNC and IEM in the mCNC. The gmCNC degraded in two steps. First, the CNC began to degrade because of low thermal stability of CNCs compared to the grafted acrylic polymer. The subsequent weight loss was attributed to the degradation of the polymer attached to CNC beginning around 330 °C, close to previously reported degradation temperatures of the poly(BA/MMA) copolymer. The weight loss curve of gmCNC was used to estimate

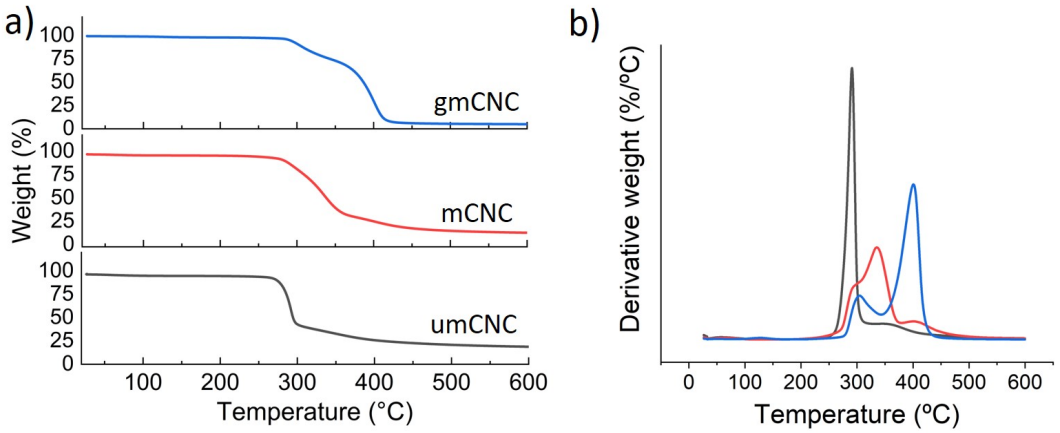

Figure 4.5: a) weight loss curves and b) derivative weight loss curves of umCNC, mCNC, and gmCNC.

the relative wt% of CNC and the attached polymer in the gmCNC. The grafted BA/MMA polymer content was found to be approximately 70 wt%, as shown in Figure C.2.

Elemental analysis of CNC samples resulted in further confirmation of the surface modifications in mCNC and gmCNC. The results of the elemental analysis are given in Table 4.2. As expected, the umCNC contained no nitrogen (N). In the surface modification of CNC, an IEM molecule forms a urethane linkage containing one N. Therefore, the measured 2.9 wt% N in mCNC and 0.7 wt% N in gmCNC indicate the presence of IEM in the functionalized CNCs. The gmCNC has a lower N composition, a higher C, and a higher H composition compared to mCNC, consistent with the C, H, and O contents added by the grafted polymer chains.

Table 4.2: Elemental weight percentage composition of umCNC, mCNC, and gmCNC.

	Elements wt% $\pm$ 0.3 wt%				
	C	H	N	S	O[a]
umCNC	40.6	6.2	0	1.1	52.1
mCNC	45.4	6.1	2.9	0.9	44.7
gmCNC	56.5	7.7	0.7	0.3	34.8

[a]Values are the calculated content by subtracting the sum of C, H, N, and S from 100%.

We obtained information about the degree of IEM modification and the grafted polymer by using the results of elemental analysis and the dimensions of the CNCs used in this work. The details of the calculations are given in the calculation section of Appendix C. The percent of surface hydroxyls of CNCs reacted with IEM was estimated to be around 65%, corresponding to nearly the limit of maximum surface modification possible [150]. Moreover, the composition of MMA and BA in the grafted polymer was determined as 65 wt% and 35 wt%, respectively. We estimated the number average molecular weight (M_n) of attached polymer chains as $\sim$1600 g/mol by following the protocol reported by Zhang et al. [162], without chain cleavage. The grafting density was found to be 0.39 chains/nm^2 by using the estimated M_n and the polymer content obtained from TGA.

The morphologies of umCNC, mCNC and gmCNC were characterized by AFM. Figure 4.6 shows the AFM amplitude images of umCNC, mCNC, and gmCNC. The distributions of the CNC dimensions (length and height) are given in Figure 4.7. We compared size distributions of umCNC-mCNC and mCNC-gmCNC by using a t-test with α=0.05. The length difference between umCNC and mCNC was significant, whereas their heights were

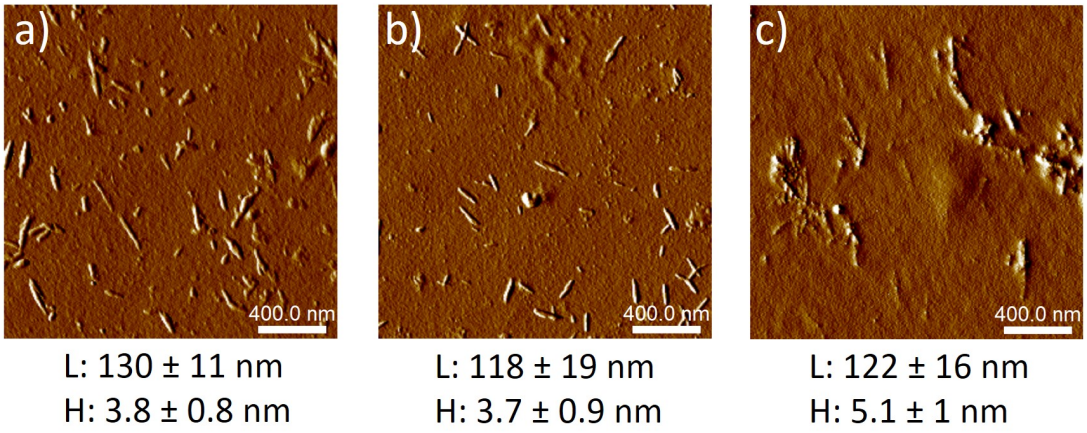

Figure 4.6: AFM amplitude images of a) umCNC, b) mCNC, and c) gmCNC.

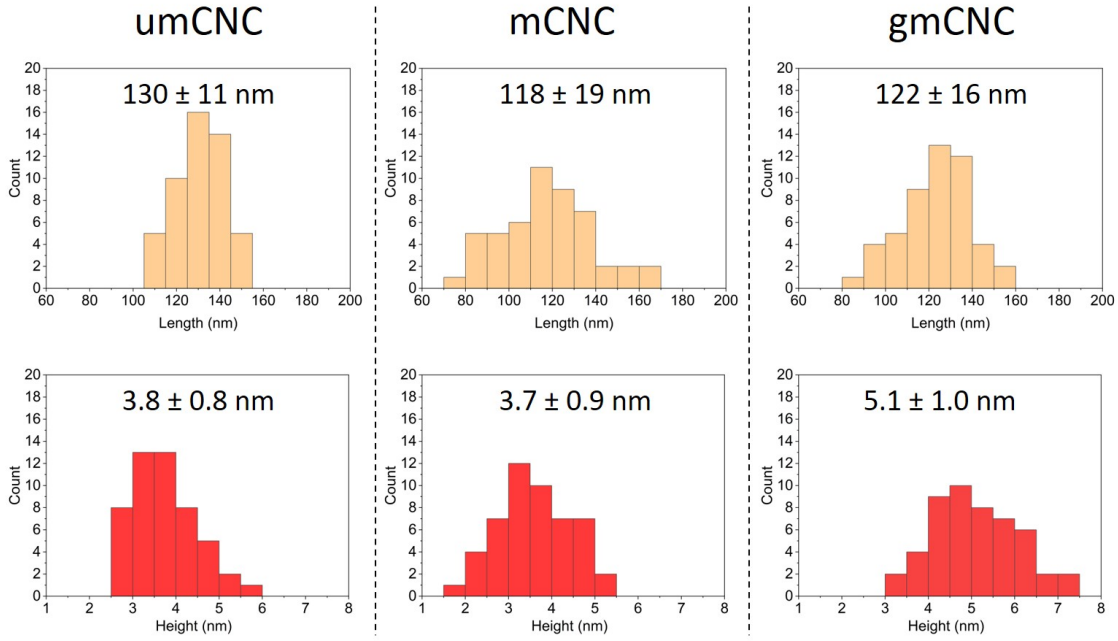

Figure 4.7: Length (top row) and height (bottom row) distributions of umCNC, mCNC, and gmCNC.

found to be similar. On the other hand, the difference in the lengths of mCNC and gmCNC was insignificant; however, the average height of gmCNC statistically increased relative to mCNC due to the polymer chains on the surface of gmCNCs.

The dispersion of CNCs in the monomer phase of the miniemulsion is crucial to maintaining the CNCs inside the monomer droplets during the polymerization. We first investigated the stability of CNCs in the mixture of BA and MMA. Then, we performed partition tests to assess the preference of CNCs for aqueous or monomer phases in a miniemulsion. BA/MMA monomer mixtures containing 1 wt% CNCs were prepared, and water was added to CNC/monomer dispersions. The monomer-to-water ratio was 1:4 as in our miniemulsion

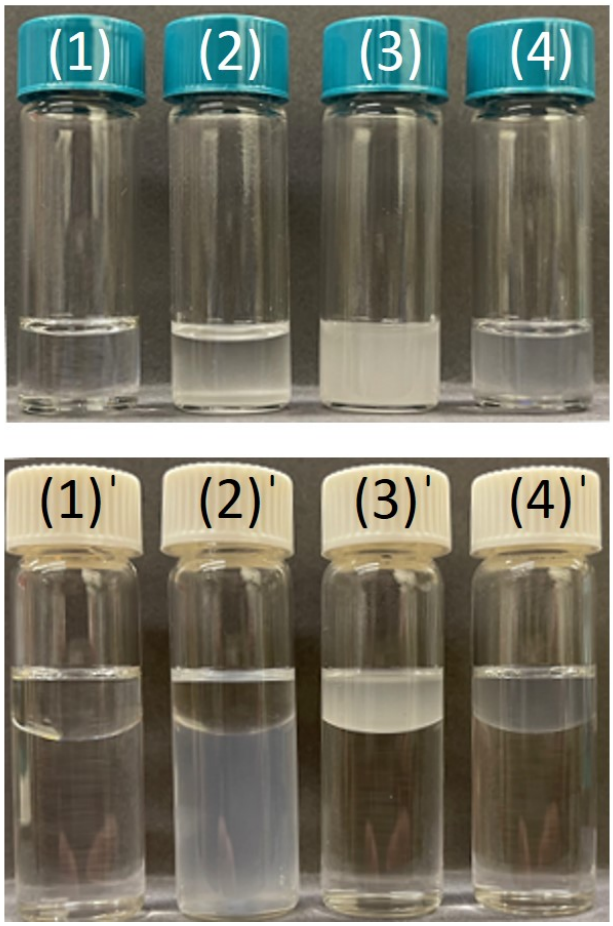

Figure 4.8: Photographic images of 50 wt% BA – 50 wt% MMA monomer mixture with (1) no CNCs, (2) 1 wt% umCNCs, (3) 1 wt% mCNCs, (4) 1 wt% gmCNCs and vials with a prime symbol, $(\,)'$, corresponding water (bottom)-monomer (top) phases.

procedure and we prepared a monomer mixture with no CNCs added as a control. The top picture in Figure 4.8 shows the vials containing monomer mixtures. While the monomer mixture with no CNC added was a clear liquid, the mCNC and gmCNC in the monomer mixture resulted in cloudy dispersions. However, the umCNC was not compatible enough with the monomer mixture to form a dispersion and quickly settled to the bottom of the vial. The dispersion stability of mCNC and gmCNC was compared by watching the vials

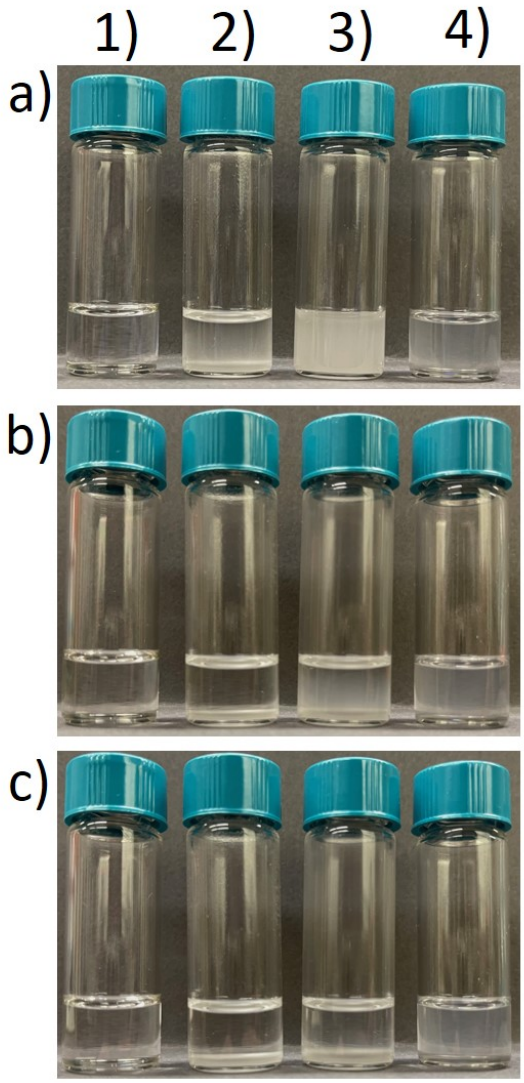

Figure 4.9: Photographic images of 50 wt% BA – 50 wt% MMA monomer mixture with 1) no CNCs, 2) 1 wt% umCNCs, 3) 1 wt% mCNCs, 4) 1 wt% gmCNCs. The pictures were taken after resting a) 5 min, b) 5 h, and c) 24 h.

over time to see if any sedimentation occurs. The mCNC began to settle to the bottom of the vial after 5 h, and the aggregates of mCNC sedimented after 24 h (Figure 4.9). We did not observe any sedimentation in the gmCNC/monomer dispersion after 24 h. The bottom picture in Figure 4.8 shows the vials containing monomer-water phases. The picture was taken 15 min after mixing, allowing CNCs to partition to their preferred phase. The phase of neat monomer mixture was on top of the water phase in the first vial. Whereas umCNCs preferred to migrate into water phase in the second vial, both mCNC and gmCNC partitioned to the monomer phase. The clarity of water phases suggests that the majority of mCNC and gmCNC remained in the monomer mixture.

4.3.2 Miniemulsion polymerization

Controlling the particle size of the latex

Miniemulsions with the neat BA/MMA monomer mixture were prepared by using different amounts of surfactants to control the particle diameter of the latex. Table 4.3 summarizes the characteristics of the produced latexes, including particle size, surface tension, coagulum percent, monomer conversion, and pH. We maintained the pH of the latexes in the range of 8-9 by using sodium bicarbonate in conjunction with the potassium persulfate initiator. The average particle size of the latexes ranged from 106 to 290 nm. Overall, a lower amount of surfactant led to a larger particle size and a higher surface tension.

Table 4.3: Effects of the variation in the surfactant concentration on the characteristics of the latexes.

Surfactant concentration (mM)	Average particle size (nm)	Surface tension (mN/m)	Coagulum (%)	Monomer conversion (%)	pH
0.81	290 ± 4	62.6 ± 0.08	4.40	79.0	8.42
1.61	205 ± 3	61.6 ± 0.06	2.44	85.4	8.37
3.23	144 ± 4	59.8 ± 0.08	1.96	89.7	8.44
4.85	121 ± 2	58.6 ± 0.04	1.45	91.3	8.46
7.28	106 ± 3	55.4 ± 0.04	1.15	92.4	8.76

An equilibrium exists among the surfactant molecules in latex/air surface, in micelles, in bulk aqueous phase, and surfactants adsorbed at particle interfaces. Therefore, a higher surface tension measured at the water/air interface of the latex indicates a lower concentration of surfactant present in the aqueous phase. Surface tension measurements ranged from 55 to 62 mN/m, higher than the surface tension measured at CMC of SDBS (35 mN/m in Figure C.3). This result indicates that no micelles were present in any of the latexes and the surface coverages of the particles were incomplete. The surface tension increased with decreasing surfactant concentration, as expected. The surface coverage is decreasing with decreasing surfactant content and increasing particle size; the less surface coverage, the more particles are prone to coagulation [183]. Also, large particles more tend to coagulate due to Stokes law settling. Therefore, we observed an increasing amount of coagulum with decreasing surfactant concentration. Based on the monomer conversion calculations, slower polymerization occurred when a lower surfactant concentration was used. This was expected because less surfactant results in a smaller number of monomer droplets that are larger in size and consequently a slower polymerization [184].

Incorporating CNCs into the latex

We selected two different surfactant concentrations (0.81 mM and 2.42 mM) to be used in the latex recipes including CNCs in order to obtain particle sizes larger than the length of the CNCs. The latexes were denoted as L-X-Y-Z where X represents the concentration of the surfactant (mM) and Y stands for the type of CNCs used in the preparation of latexes while Z is for the CNC loading. Table 4.4 provides the properties of the synthesized latexes such as surface tension, coagulum percent, monomer conversion, pH, and viscosity and also lists the T_g of the resulting latex films.

The pH of all latexes was maintained within the same range (pH=7-8). The surface tensions of latexes containing less surfactant were slightly higher than the latexes with higher surfactant concentration. The latexes prepared with mCNCs (L-0.81-mCNC-1 wt%, L-

2.42-mCNC-1 wt%, and L-2.42-mCNC-0.5 wt%) had a lower surface tension (45 – 48 mN/m) relative to the surface tension of the rest of the samples, ranging from 53 to 55 mN/m. The mechanism causing the decrease in the surface tension is not well-understood. We expect mCNCs concentrated in the monomer/water interface during polymerization based on the observation from the partition tests over time. The mCNCs concentrated in the interface may cause the desorption of some surfactant molecules from the surface of latex particles to the aqueous phase during polymerization. The latexes with higher surfactant concentration (2.42 mM) resulted in slightly higher monomer conversions compared to the latexes with a lower surfactant concentration (0.81 mM). This result was anticipated due to the smaller droplet sizes expected in the latexes prepared with a higher surfactant concentration. However, the monomer conversions were slightly lower when we include CNCs in the latex synthesis compared to the conversions obtained in the neat latexes. This result may be associated with the possibility of CNCs swollen by some portion of monomers. The swollen CNCs may take some monomer molecules away from the polymerization, resulting in a lower conversion.

Table 4.4: Summary of latex properties and T_g of the resulting latex films.

Latex samples	ST[a] (mN/m)	Coagulum (%)	MC[b] (%)	pH	Viscosity (cp)	T_g (°C)
L-0.81-Neat	55.9	2.92	88.5	7.86	1.74	22 ± 0.4
L-0.81-umCNC-1 wt%	54.6 ± 0.7	2.41	86.7	7.46	7.87	21 ± 1.5
L-0.81-mCNC-1 wt%	47.9 ± 0.6	3.04	83.2	7.73	1.6	18 ± 0.3
L-0.81-gmCNC-1 wt%	54.6 ± 0.4	3.18	83.5	7.6	1.63	20 ± 0.7
L-2.42-Neat	54.7 ± 0.4	2.19	90.3	7.54	1.76	22 ± 0.3
L-2.42-umCNC-1 wt%	53.1 ± 0.8	2.08	88.1	7.71	7.01	21 ± 1.3
L-2.42-umCNC-0.5 wt%	53.7 ± 0.2	3.05	87.9	7.88	3.17	22 ± 0.4
L-2.42-mCNC-1 wt%	45.4 ± 0.4	2.7	84.7	7.73	1.65	19 ± 0.6
L-2.42-mCNC-0.5 wt%	45.3 ± 0.2	2.17	85.3	7.77	1.65	21 ± 1.2
L-2.42-gmCNC-1 wt%	53.2 ± 0.4	3.17	85.3	7.81	1.72	20 ± 1.0
L-2.42-gmCNC-0.5 wt%	52.9 ± 0.5	3.3	86.9	7.79	1.6	20 ± 1.4

[a]Surface tension (mN/m).
[b]Monomer conversion (%).

We obtained latex coagulum levels ranging from 2.1 to 3.3% of total solid content with no notable differences between samples. The latex films and the coagula were characterized by ATR-FTIR and the spectra of the samples were given in Figure 4.10. While the spectra of all latex films show the same fingerprint, the coagula obtained from the latexes with mCNCs were different. The coagula of L-0.81-mCNC-1 wt%, L-2.42-mCNC-1 wt%, and L-2.42-mCNC-0.5 wt% exhibited some of the characteristic peaks of CNC; for example, hydroxyl stretching at 3000-3700 cm^{-1}. Also, we observed the peaks at 1060 cm^{-1} and 1035 cm^{-1} corresponding to the C-O bond of carbons 3 and 6 of the CNC. These peaks suggested the tendency of mCNCs to concentrate in the coagulum during the polymerization. The presence of mCNCs in the coagula was further verified by elemental analysis.

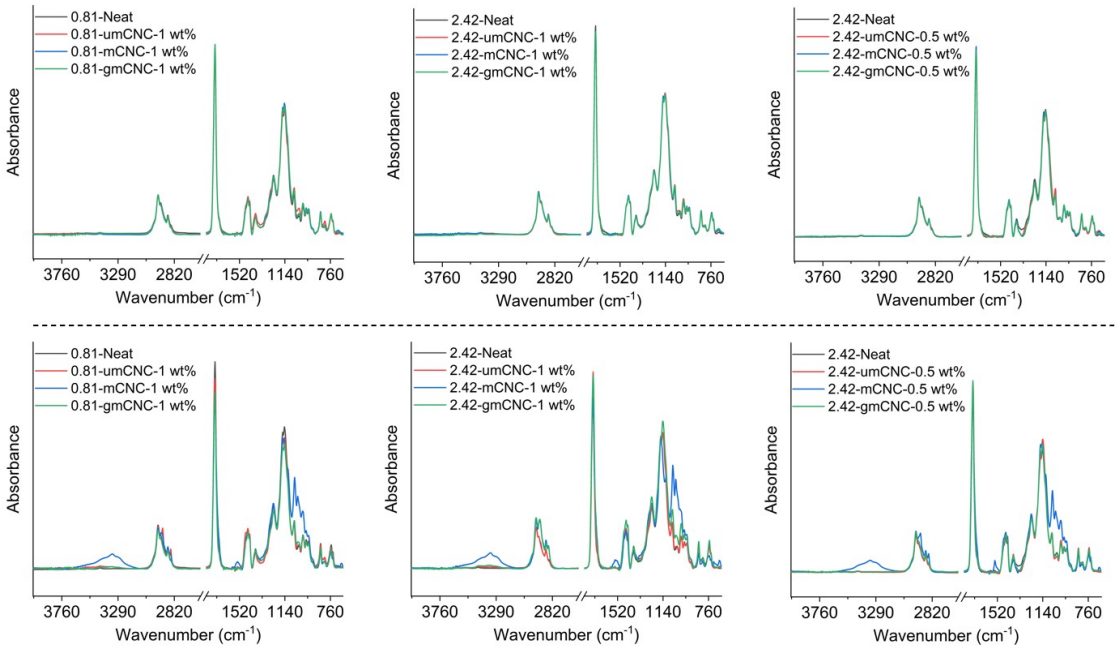

Figure 4.10: FTIR spectra of latex films (top row) and the related latex coagula (bottom row).

In Table C.1, the results of the elemental analysis were provided for carbon (C), hydrogen (H) and nitrogen (N) in all latex films and coagula. Samples were dominantly comprised of C, H, and O because of the elemental composition of the latexes (copolymer of MMA-$C_5H_8O_2$ and BA-$C_7H_{12}O_2$). The mCNC and gmCNC contained N because of the

NCO moiety of IEM attached to CNCs. However, no N content was detected in any latex film. We did not expect N in L-Neat and L-umCNC samples and the N would be only 0.03 wt% and 0.006 wt% for 1 wt% mCNC and 1 wt% gmCNC loaded latexes, respectively, by assuming a homogeneous distribution of CNCs within the latex system. These expected N contents in L-mCNC and L-gmCNC samples are significantly lower than the detection uncertainty ($\pm$ 0.3 wt%) of the method used in the elemental analysis. On the other hand, the coagulum of L-0.81-mCNC-1 wt%, L-2.42-mCNC-1 wt%, and L-2.42-mCNC-0.5 wt% contained 0.95 wt%, 0.75 wt% and 0.5 wt% N, respectively. Consistent with the mCNC loadings, N wt% detected in the coagulum of L-2.42-mCNC-0.5 wt% was lower than the N in the coagulum of L-2.42-mCNC-1 wt%. When we assumed the coagulation of all mCNCs, the N content in the coagulum would be approximately 1 wt% N for 1 wt% mCNC-added latexes. These numbers indicated that nearly all mCNCs coagulated at the end of the polymerization, and the latex had almost no mCNC. For 1 wt% gmCNC-added latex coagulum, the N content in the coagulum was calculated as 0.21 wt% by assuming the coagulation of all loaded gmCNCs. Therefore, N content in the coagula of L-0.81-gmCNC-1 wt%, L-2.42-gmCNC-1 wt%, and L-2.42-gmCNC-0.5 wt% may not be detectable due to the sensitivity of the elemental analysis technique.

Overall, both the results of FTIR and elemental analysis showed the presence of mCNCs in the coagulum of the latexes prepared with mCNC. However, we could neither confirm nor contest the presence of gmCNCs in the coagula of the latexes synthesized with gmCNC because of the sensitivity of the techniques used.

Table 4.4 also shows the viscosity measurement of the latexes. The viscosities of latexes prepared with umCNC (L-0.81-umCNC-1 wt%, L-2.42-umCNC-1 wt%, and L-2.42-umCNC-0.5 wt%) were substantially higher when compared to the rest of the samples having similar viscosities. This result can be associated with the shear thinning nature of CNCs and the presence of a higher concentration of dispersed entities (particles and CNCs), suggesting the existence of umCNCs in the aqueous phase.

T_g of latex films is an important property to understand the difference in the polymer segmental mobilities and copolymer-filler interactions. We measured T_g of the latex films in the range of 18 to 22 °C. This range of T_g values can result from the small changes in the coagulum percentages and monomer conversions. Polymer composition is impacted by monomer conversion because of the difference in reactivities of the two monomers used. BA is more reactive than MMA (r_{BA}=2.55 and r_{MMA}=0.36) [185] and a variation in the polymer composition (composition drift) is expected due to the batch process used. Therefore, it is difficult to draw a clear conclusion about the effect of the CNC type and loading on polymer mobility. However, we observed slightly lower T_g in the latex films prepared with mCNC (found to be statistically different from other latex films by t-test with α=0.05). The mCNCs can play a role in the composition drift because the vinyl groups on the surface of mCNCs are available for polymerization with a portion of monomers. IEMs on the surface of mCNC tend to react more favorably with MMA than BA (r_{IEM}=1.19 and r_{MMA}=0.84; r_{IEM}=2.50 and r_{MMA}=0.40) [186]. Therefore, the unreacted BA composition remaining for latex synthesis increases while the mCNCs coagulated, lowering the T_g of the resulting latex film.

Figure 4.11 shows the measurements of average particle size and zeta potential of all latexes. The hydrodynamic diameters measured in all latexes (Figure 4.11a) were in the range of 186 – 430 nm, with polydispersity indexes less than 0.1. As expected, the latexes with a lower surfactant concentration had larger particle sizes compared to the average sizes obtained in the case of high surfactant concentration. For both surfactant concentrations, the size of L-umCNC and L-mCNC increased with increasing CNC loading; however, the size of L-0.81-gmCNC decreased and the size of L-2.42-gmCNC remained unchanged with increasing CNC loading. Elmabrouk et al. [187] previously observed an increase in the particle size of poly(styrene-co-hexylacrylate) latex particles when umCNCs were loaded to the aqueous phase via miniemulsion polymerization. The result was attributed to particle agglomeration driven by umCNCs during the polymerization.

Figure 4.11b displays the zeta potential measurements. The zeta potentials of all latexes were negative due to the anionic surfactants at the surface of latex particles. Also, all measured zeta potentials were more negative than -40 mV, indicating good colloidal stability. In general, the zeta potential of L-Neat and L-gmCNC had an insignificant difference (by t-test with α=0.05), whereas the zeta potential of L-mCNC and L-umCNC were less negative compared to L-Neat and L-gmCNC.

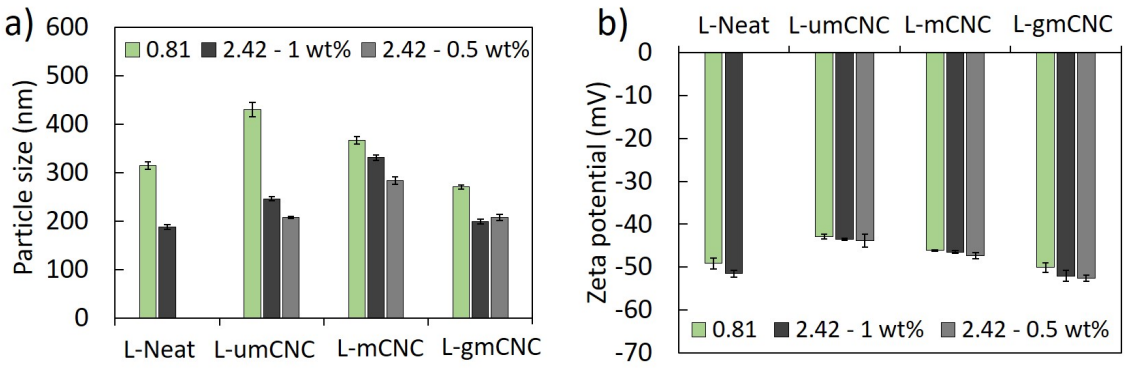

Figure 4.11: a) average particle size and b) zeta potential of acrylic latexes.

The latex particles were imaged by AFM to analyze the particle morphologies in the latexes and to identify the location of the CNCs. AFM amplitude images of the latex particles are given in Figure 4.12. In some images, latex particles are partially coalesced due to the fact that the T_g of the polymers is close to the ambient temperature. As expected, we observed only spherical polymer particles in the neat latex samples (Figure 4.12a and 4.12e). Regardless of the surfactant concentration used, latexes prepared with umCNC contained rod-like CNCs outside the latex particles (Figure 4.12b and 4.12f) even though umCNCs were initially incorporated into the monomer phase. We did not observe any rod-like particles in L-0.81-mCNC-1 wt% and L-2.42-mCNC-1 wt% (Figure 4.12c and 4.12g), supporting our conclusion from the previous characterization about the presence of mCNCs in the coagula, not in the latex. Figure 4.12d and Figure 4.12h show the particle morphologies of latexes prepared with gmCNC (L-0.81-gmCNC-1 wt% and L-2.42-gmCNC-1 wt%). The gmCNCs were not observed in the outside of the latex particles, unlike umC-

NCs. We recognized faint rod-like features on/in the particles of L-0.81-gmCNC-1 wt% and L-2.42-gmCNC-1 wt%, suggesting the presence of gmCNCs partially on the outside or buried inside the acrylic particles. To better demonstrate the particle morphology observed in gmCNC-added latex samples, Figure 4.13 displays AFM height, amplitude, and phase images of the region marked with a white square in Figure 4.12h. In the phase image, Figure 4.13c, rod-like features have a light color similar to the hard substrate, compared to the darker color of the polymer particles. This observation supports the interpretation that hard gmCNCs are located on the surface of latex particles.

Mechanical testing of the final latex films was performed by a biaxial film tensile test (HTMECH) and DMA. We obtained tensile strength and strain at break from HTMECH, and the results are shown in Figure 4.14. The tensile strength and strain at break values of all latex films were not statistically different from each other (by t-test with α=0.05). The tensile strength of the latex films was around 6-7 MPa, while the strain at break was about 250%.

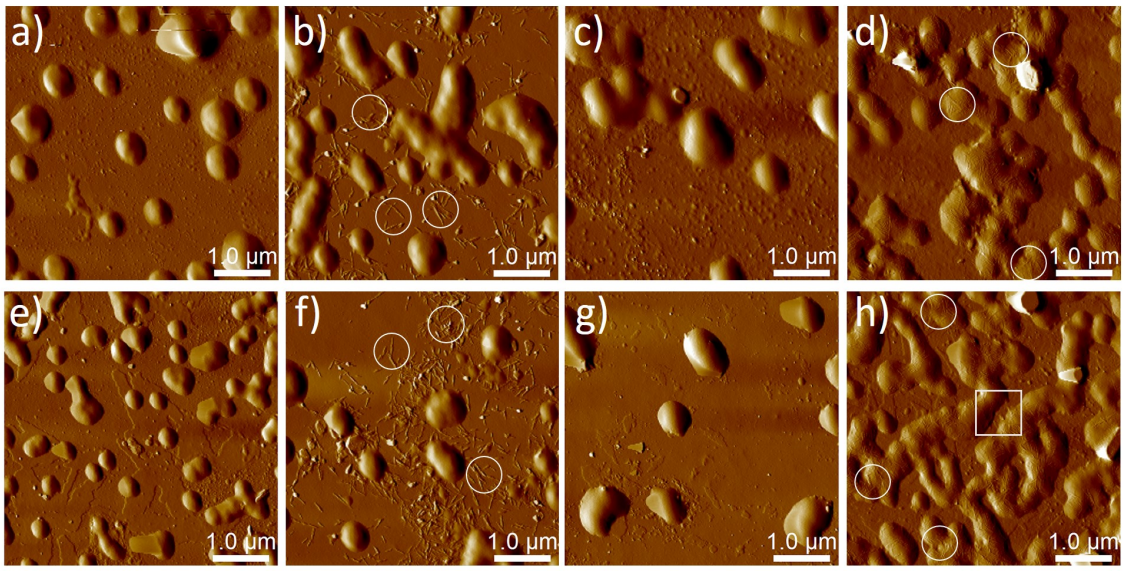

Figure 4.12: AFM amplitude images of particle morphology in the latexes: a) L-0.81-Neat, b) L-0.81-umCNC-1 wt%, c) L-0.81-mCNC-1 wt%, d) L-0.81-gmCNC-1 wt%, e) L-2.42-Neat, f) L-2.42-umCNC-1 wt%, g) L-2.42-mCNC-1 wt%, and h) L-2.42-gmCNC-1 wt%. Circles show CNCs outside and inside the latex particles. The square region is shown in Figure 4.13.

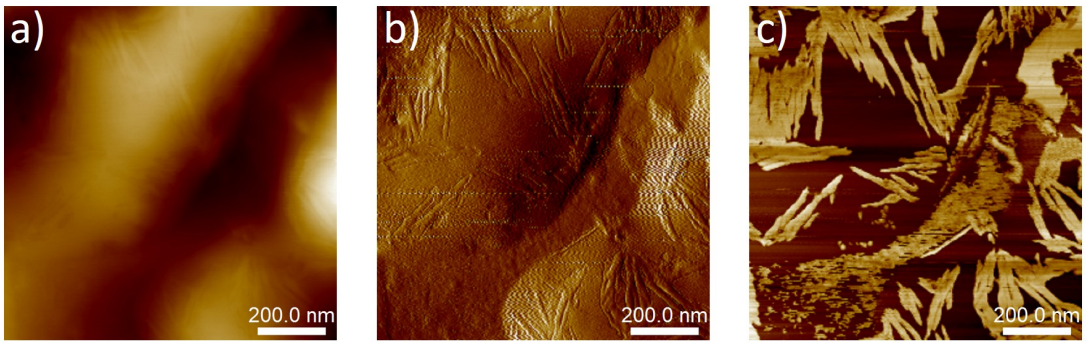

Figure 4.13: AFM images (a: height, b: amplitude, and c: phase) of L-2.42-gmCNC-1 wt% with 1 μm scan size showing the region marked with a white square in Figure 4.12h.

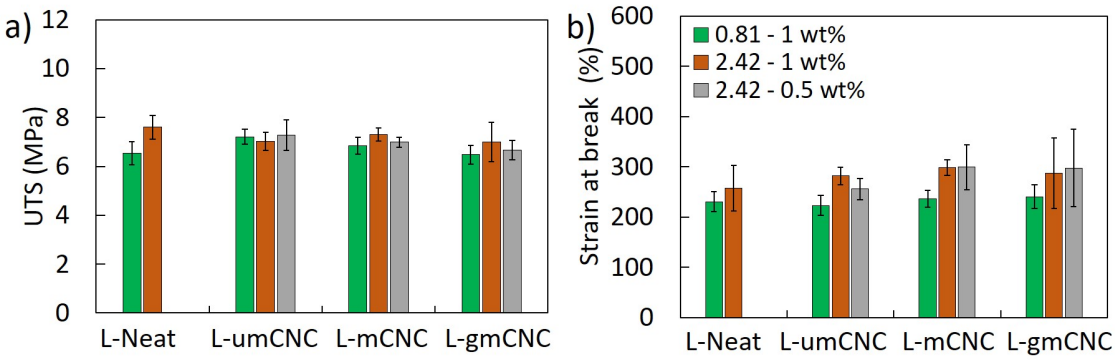

Figure 4.14: a) UTS and b) strain at break of the latex films.

Dynamic oscillatory frequency tests were performed at room temperature to understand the impact of CNC type or concentration on the moduli of the latex films. The storage modulus measurements are given in Figure 4.15. The loss modulus and tanδ are provided in Table C.2. The storage moduli of L-2.42-umCNC-0.5 wt% and L-2.42-umCNC-1 wt% were slightly higher than the moduli of L-2.42-Neat, whereas the moduli of L-2.42-mCNC and L-2.42-gmCNC samples (both 0.5 wt% and 1 wt%) were slightly lower than the moduli of L-2.42-Neat. For example, at 1 Hz, the modulus of L-2.42-Neat was 54 MPa, while the moduli of L-2.42-umCNC-1 wt%, L-2.42-mCNC-1 wt%, and L-2.42-gmCNC-1 wt% were 69 MPa, 40 MPa, and 44 MPa, respectively. These slight changes in the modulus values may not necessarily be a function of CNC type because minor differences in the T_g of the related latex films (Table 4.4) could affect the storage moduli. Also, CNC concen-

tration did not remain at 1 wt% loading in all latex films. For example, mCNC coagulated during polymerization and could not be incorporated into the latex films. In addition, the encapsulation efficiency of gmCNCs is unknown, although they appear to be present in the particles in Figures 4.12 and 4.13. Because of these factors affecting the moduli and the proximity of the measured values, it is difficult to draw conclusions about the differences between samples.

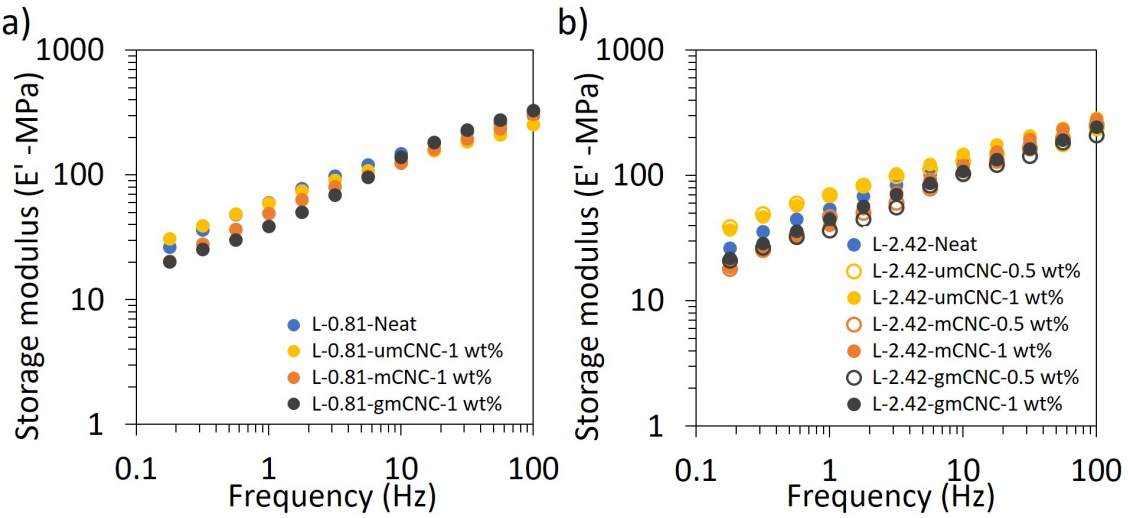

Figure 4.15: Storage modulus (MPa) of a) L-0.81 and b) L-2.42 samples with different CNC types and loadings as a function of frequency (in the linear regime at 25 °C).

In general, the mechanical properties in the CNC loaded latex films were not markedly different from those of the neat latex films. This outcome was expected for the latexes prepared with mCNCs because mCNCs were mostly detected in the coagula and not in the latex. The outcome was also expected for the latex films prepared with umCNC due to the tendency of CNCs in the aqueous phase to aggregate during film formation, thus reducing their effectiveness [88]. However, we were expecting improvement in the mechanical properties of gmCNC-added samples because the encapsulation of the filler is anticipated to result in a more homogeneous distribution of the filler in the polymer matrix [188, 189] (see Figure 4.2). The inability to enhance the mechanical properties has several possible explanations. The encapsulation or the incorporation efficiency of gmCNCs inside the la-

tex particles may not be enough to enhance the mechanical performance of the resulting films, or 1 wt% loading may not be sufficient to improve the mechanical properties of our latex films. If the neat film were softer, a 1 wt% loading might make a difference in the mechanical properties. For example, Yu et al. [181] measured the shear moduli (G' and G'') of CNC loaded (1 wt%) acrylic PSAs (either outside or inside the polymer particles) as a function of frequency by using a rheometer. The reinforcing effect of CNCs was observed where the G' values of all PSAs were lower than 0.3 MPa. In fact, the CNC loadings with gmCNCs are not truly 1 wt% because gmCNC is only 30 wt% CNC and 70 wt% polymer by mass. A higher content of CNC may advance the mechanical performance of the latex films; however, we observed significant coagulation (coagulum $>$ 10 wt%) when 3 wt% gmCNC loading was incorporated into the monomer phase of miniemulsion. This result may be associated with the increased viscosity of the monomer phase with increasing CNC content. Increasing viscosity of the monomer phase limits the ability to form small droplets under fixed shear, preventing generation of a miniemulsion [189].

4.4 Conclusions

We incorporated different types of CNCs (umCNC, mCNC, and gmCNC) into the monomer phase containing acrylic monomers (BA and MMA) and performed a miniemulsion polymerization. The hydrophobicity of umCNC was increased by modifying the CNC surface. The mCNCs were obtained by using difunctional IEM molecules via urethanization. The pendant vinyl groups on the surface of mCNCs were then used to graft copolymer chains of BA and MMA, producing gmCNCs. Miniemulsion polymerizations containing CNCs (0-1 wt%) resulted in colloidally stable latexes with minimal coagulation. This study emphasizes how the compatibility of CNCs with the monomer phase is essential for a successful encapsulation. The surface chemistry of CNCs influenced the location of CNCs (either aqueous or monomer phase). The umCNCs migrated to the aqueous phase even though they are added into the monomer phase and were found to be located outside the latex par-

ticles. The mCNCs were found in the latex coagulum, suggesting that they did not possess long-term stability in either the aqueous or monomer phase. The gmCNCs were more compatible with acrylic monomers relative to mCNCs. AFM images of gmCNC-added samples showed rod-like features well-attached to the surfaces of the polymer particles, suggesting the presence of gmCNCs in or on the polymer latex particles. However, no major changes were observed in the mechanical performance of the latexes prepared with different types of CNCs relative to neat latex. The high amount of polymer (70 wt%) in the gmCNCs reducing the actual loading of CNC and limited CNC loading below 1 wt% may be factors affecting the inability to improve the mechanical properties of the latex films. This work encourages the study of the optimization of polymer grafting and CNC/monomer compatibility to better understand the effect of the encapsulation process on mechanical properties. Overall, we believe that the knowledge provided here will be helpful for researchers who work on the incorporation of organic nanoparticles similar to CNCs into the latex particles.

CHAPTER 5
CONCLUSION

This chapter summarizes major contributions and conclusions from this dissertation and presents recommendations for future research directions.

5.1 Summary and conclusions

This dissertation provides a methodology for incorporating CNCs into different phases of polymer latexes: aqueous (Chapter 2) and polymer phases (Chapter 4). The effects of CNC location on the film formation and mechanical properties of latexes were investigated. CNCs required surface modification to incorporate them into the polymer phase of latex because of their hydrophilic nature; therefore, a versatile surface modification scheme for CNCs was developed (Chapter 3). The three specific objectives outlined in Chapter 1 were achieved and the results were discussed in each main chapter.

In Chapter 2, CNCs were incorporated into the aqueous phase of acrylic latex via a post-blending method. Relative to other papers that have reported the use of CNCs in the aqueous phase, the novelty in this study is the use of CNCs to enable a binder system with zero added VOC coalescent. Unlike other papers in this field, we have evaluated the VOC content quantitatively and shown that we can reproduce mechanical performance of VOC-containing binders without use of VOC, while maintaining ambient film formation. CNCs were blended with two types of BA/MMA/MAA latexes prepared by emulsion polymerization. The -COOH functional groups were introduced to the surface of latex particles and two latexes used had 5 wt% and 10 wt% MAA content, respectively. CNC addition increased the viscosity of latexes; however, their addition did not influence the colloidal stability. The nanocomposite latexes formed uniform films at ambient conditions and the addition of CNCs did not affect the T_g and MFFT of the latex films. While CNCs were

not spotted on the surface of the films, homogeneous distribution of nanoaggregates ($<$ 50 nm in diameter) by CNCs were observed in the cross-section of the films, suggesting the confinement of CNCs to interstitial regions between latex particles during drying. CNC loadings significantly enhanced the tensile strength, Young's modulus, and hardness of the latex films without negatively affecting ambient film formation. The latex with higher MAA content resulted in slightly higher tensile strength and modulus in the films. The mechanical properties achieved in this approach are comparable with the conventional hard binders. This chapter highlighted the potential of CNC to be used as an aqueous additive in the acrylic binders and encouraged further investigations for reformulating waterborne acrylic products with CNCs.

In Chapter 3, a reproducible urethanization procedure was developed to modify the surface of CNCs. Various modes of surface modification are available in literature to improve compatibility between CNCs and polymer matrices. However, what is often missing from papers in this field is an optimization of the degree of substitution of the CNC modifier and, importantly, the effects of the modification on CNC crystallinity. Most papers do not report the effects of increasingly aggressive modification on CNC crystallinity, but these are important considerations in translating to applications. IEM, an isocyanate molecule carrying an acryloyl group, was used to modify the CNC surface via urethanization, making the CNC a macromonomer with pendant acryloyl groups on its surface. This study provides a new insight to the field, by using a known CNC modifier, IEM, optimization of its degree of substitution on CNCs and developing an understanding of the interplay between degree of substitution and CNC crystallinity. We investigated the effect of modification conditions such as reaction time and temperature on the degree of modification, crystallinity, and morphology of the CNCs. The hydrophilicity of CNCs decreased with increasing surface functionalization. The degree of modification was primarily affected by the reaction temperature. However, the severe reaction conditions (the highest temperature and long reaction times) decreased the dimensions and the crystallinity of CNCs.

This study demonstrates a tunable modification scheme by varying the reaction conditions and helps to determine the optimum condition for the desired application. Moreover, the copolymerization ability of macromonomer CNCs (modified CNCs) was tested with BA and MMA monomers via the grafting through technique. The successful copolymerization was verified by FTIR, TGA, and elemental analysis characterizations. Compared to umCNCs, polymer-grafted CNCs dispersed more homogeneously in the BA/MMA acrylic matrix and improved the tensile strength and the film hardness. This study expands the use of CNCs by offering a versatile modification route and macromonomer functionality. Polymer grafting can also be adjusted by tuning the macromonomer functional groups with the urethanization reaction scheme. Grafting other vinyl monomers or other polymer matrices for dispersion of grafted CNCs can also be explored.

In Chapter 4, CNCs were incorporated into the polymer phase of latex. This study explored encapsulation of CNCs into polymer particles via miniemulsion polymerization. The novelties in this study are use of classical miniemulsion procedure including costabilizer and comparison of macromonomer to polymer-grafted CNCs for the encapsulation. First, different types of CNCs (unmodified, modified/macromonomer, and polymer-grafted) were prepared and the functionalized CNCs were characterized for their size, morphology, and the degree of functionalization. Partition tests were performed to evaluate the preference of CNCs to water or monomer phases of miniemulsion. The umCNCs partition to the water phase, whereas the functionalized CNCs preferred the monomer phase. Before performing miniemulsion polymerizations with CNCs, a polymerization scheme was developed with only monomers (50 wt% BA and 50 wt% MMA) to control the size of latex particles by changing surfactant concentration. Two surfactant concentrations resulting in a latex particle size larger than the length of CNCs were selected to incorporate the CNCs (1 wt%). The latex properties, particle morphology and mechanical properties of the latex films were investigated. All latexes were colloidally stable with minimal coagulations (2-3 wt%). The polymer-grafted CNCs were spotted as partially embedded in the latex parti-

cles, whereas umCNCs were located outside the latex particles and modified (non-grafted) CNCs were lost to the coagula of latexes during the polymerization. This comparison highlights the importance of the compatibility of CNCs with the monomer phase to enable the partition of CNCs into the polymer phase in miniemulsion. No improvement in the mechanical properties of latex films was observed with the addition of CNCs. The inability to improve the mechanical properties of the latex films may be due to the high amount of polymer grafting (70 wt%) on CNCs and limited CNC loading below 1 wt%. This result aroused interest to understand how the optimization of polymer grafting would affect the reinforcement potential of CNCs.

Altogether, these three main chapters demonstrate the techniques developed to incorporate CNCs into acrylic latex systems. Incorporating CNCs into the polymer phase of latex was more challenging than the CNC addition into the aqueous latex phase. Table 5.1 compares the aqueous phase approach in Chapter 2 with the encapsulation approach in Chapter 4 in various aspects such as the technique used to produce latexes, monomers used in the monomer phase, the functionalization of CNCs, pros/cons of each approach, and the resulting effect on the mechanical properties of the latex films. For the aqueous phase approach, simplicity of the method and no need for CNC modification were the benefits. Significant improvement in the mechanical properties of the latex films was observed despite the nano-aggregates by CNCs in the bulk of the film. In the encapsulation approach, MAA was not included in the monomer phase due to the differences in the mechanism of miniemulsion polymerization relative to the emulsion polymerization. The encapsulation approach is anticipated to result in a more homogeneous distribution of the filler in the polymer matrix. However, the CNC loading is limited by 1 wt% and the methods to characterize the CNCs inside the latex particles are not well-established. The mechanical properties in the CNC loaded latex films were not markedly different from those of the neat latex films, although we identified the gmCNC as a part of the polymer phase. The results led to more questions and research directions that need to be investigated. When the limita-

tions of each incorporation approach are compared to the resulting mechanical performance of the latex films, the results from the aqueous phase approach are more encouraging further studies in industry for CNC use in waterborne coatings to address the *film formation dilemma*. The addition of CNCs into latex binders will require reformulation studies with the other components in the commercial formulations for a specific coating application. On the other hand, the encapsulation approach is in early stages in research and requires additional investigation in order to make a fair comparison to the aqueous phase approach. Overall, the information presented in this dissertation will facilitate the development of commercial latex binders containing CNCs towards more environmentally friendly waterborne coatings. The findings are expected to guide researchers in the paint, coating, and cosmetic industries.

Table 5.1: Comparison of aqueous phase approach to encapsulation approach for incorporating CNCs into the acrylic latex system.

	Chapter 2 Aqueous phase approach	Chapter 4 Encapsulation approach
Technique to produce latexes	Emulsion polymerization	Miniemulsion polymerization
Monomers used	BA, MMA, and MAA	BA and MMA
CNCs added	Unmodified	Modified
Pros	- Simplicity of the preparation of composite latexes - CNC loadings up to 15 wt%	- Promising to mitigate the CNC aggregations in the dried latex film
Cons	- Aggregation of umCNCs in the latex films	- Difficulty in characterization of CNCs inside the latex particles - Limited CNC loading (1 wt%)
Mechanical properties	Significant improvement observed in the CNC loaded latex films	No markable difference observed in the CNC loaded latex films

5.2 Recommendations for future work

The sections below suggest a few possible research directions for future work.

5.2.1 Using modified CNCs in the aqueous phase of latex to mitigate the aggregation in the latex films

Chapter 2 demonstrated significant improvements in the mechanical properties of latex films with the addition of CNCs into the aqueous phase of latex. The simplicity of the preparation of composite latexes is a benefit when expanding this study to industry. However, the mechanical performance of latex films could be further improved if the presence of nanosized CNC aggregates found in the polymer matrix was eliminated or reduced. One alternative approach to mitigate the CNC aggregations could be using lightly modified CNCs in the aqueous phase. Modification of CNCs can be optimized to reduce the CNC-CNC interactions in water and, at the same time to keep them still hydrophilic enough to enable

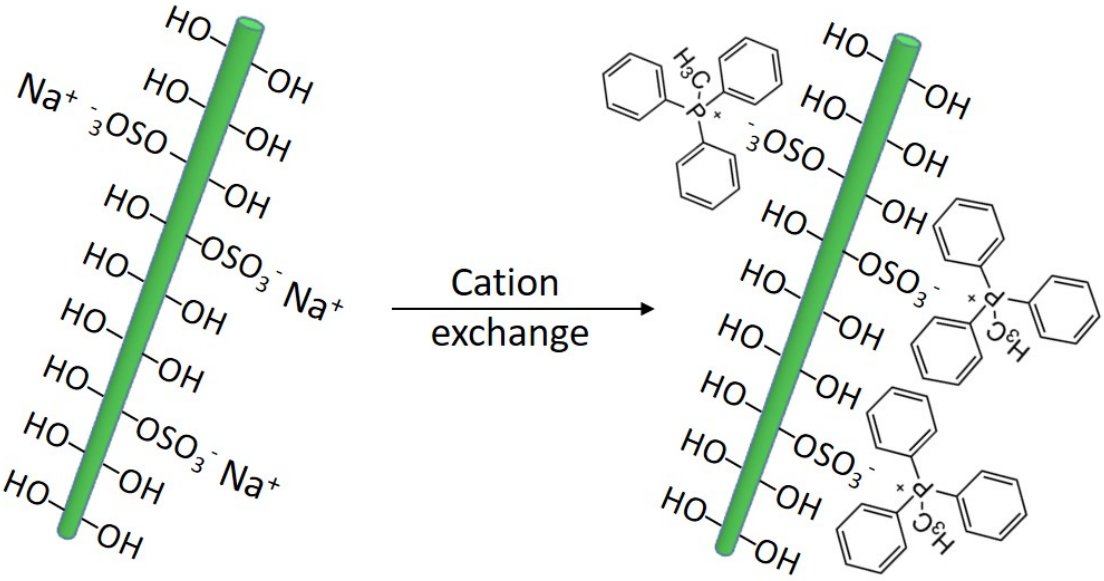

Figure 5.1: Schematic showing the replacement of Na counter ions with methyl triphenyl phosphonium.

their dispersion in water. For example, Fox et al. [190] modified the CNC surface by replacing counter ions (Na^+) of sulfate half ester groups with more hydrophobic cations (Figure 5.1). The aggregate size of CNCs was reduced at least an order of magnitude in epoxy and polystyrene composites by using ion exchanged CNCs. This improvement was associated with the reduced van der Waals and hydrogen bonding interactions due to the increased distance between CNC surfaces. Investigating different surface modification techniques for CNCs in the aqueous phase could be an interesting study to reduce the self-interaction of CNCs and promote the mechanical strength in the latex films.

5.2.2 Optimization of the degree and type of polymer grafted on CNCs

Chapter 3 comparatively analyzed the dispersion state of unmodified and polymer-grafted CNCs in acrylic polymer matrix (section 3.3.3). The polymer-grafted CNCs dispersed better in acrylic polymer matrix than umCNCs, resulting in an enhancement in the tensile strength and hardness of the acrylic films. However, this was a case study to demonstrate the effect of polymer grafting on the CNC dispersion in the polymer matrix. For optimum CNC dispersion and mechanical improvement, the amount of grafted polymer on the CNC could be tailored by further studying the reaction parameters of grafting (solution polymerization) such as initiator concentration, monomer concentration, polymerization time, and temperature (Figure 5.2). Moreover, other polymers could be investigated for grafting to optimize the CNC dispersion in the acrylic matrix. The incorporation of polymer-grafted CNCs into the acrylic particles in Chapter 4 (section 4.3.2) did not significantly differ in the mechanical properties of the latex films. One reason preventing the improvement may be the high amount of polymer grafting ($\sim$70 wt%) in the CNCs. Understanding the relationship between the degree of polymer grafting and the resulting mechanical properties is essential to use the reinforcement ability of CNCs effectively. Other than experimental work, molecular simulations may be helpful to understand the influence of the degree of grafting on the interactions of the polymer-grafted CNC with the bulk polymer. The re-

sults from this optimization study would be helpful to better determine the amount/type of polymer grafts on CNCs to be used in the monomer phase of the miniemulsion technique demonstrated in Chapter 4 for promoting the mechanical properties of the resulting latex films.

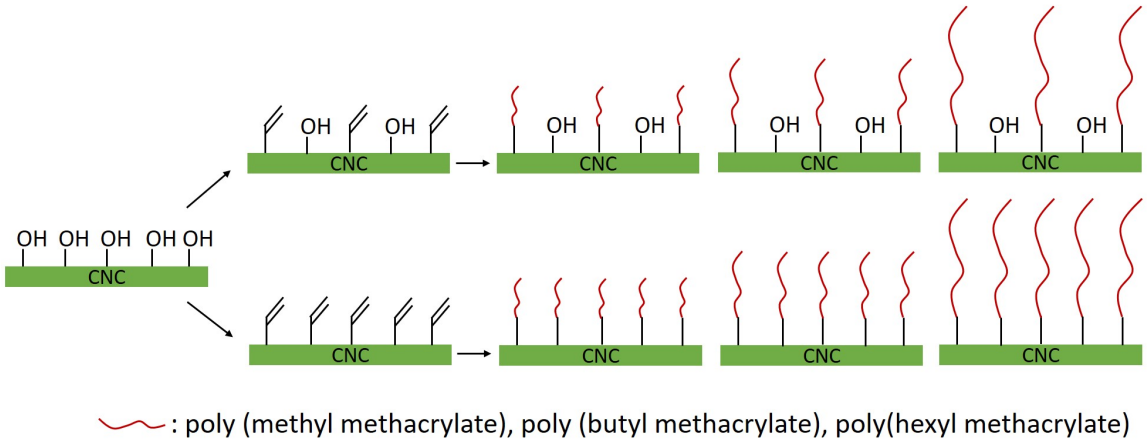

Figure 5.2: Schematic showing different polymer graft lengths and densities on CNCs. Three polymers having different hydrophobicity are suggested.

5.2.3 Developing characterization methods for CNCs inside the polymer particles

Characterization of the encapsulated CNCs within the polymer matrix is important to understand the structure-property relationship in the latex films. However, direct observation of the CNCs within the three-dimensional polymer particles is challenging. Also, spectroscopic methods are very limited because of low CNC loadings used in the miniemulsion approach. Therefore, developing an alternate characterization technique is necessary to better evaluate the morphology of particles and the encapsulation efficiency of the loaded CNCs, encouraging future research on the encapsulation technique.

Appendices

APPENDIX A

SUPPORTING INFORMATION FOR CHAPTER 2

Table A.1: The results from VOC analysis of MAA10 latex.

Compounds	Concentration (ppm)
Methanol	0
Ethanol	16.3
Acetaldehyde	0
Isopropanol	0
t-Butanol	0
1-Propanol	6.7
Acetonitrile	0
Methyl Acetate	0
1-Butanol	272.1
Ethyl acetate	0
Methyl ethyl ketone	18.2
Methyl isobutyrate	0
Ethyl acrylate	0
Methyl methacrylate	0
Toluene	0
Ethyl propionate	0
Ethylene glycol diethyl ether	1
Butyl ether	134
Ethyl benzene	0
Methyl isobutyl ketone	0
p-Xylene	0
m-Xylene	0
Butyl acetate	26.6
o-Xylene	0
Syrene	0
Butyl acrylate	10.7
Butyl propionate	36.1
Butyl methacrylate	0
Butyl butyrate	0
Benzaldehyde	6.9
Ethylhexyl acetate	38.4
2-Ethylhexyl acrylate	0

Table A.2: Formulation of emulsion polymerization to produce latexes.

Components	% with respect to monomer
Monomers	100
Sodium Lauryl Sulfate (SLS)	1
Sodium Carbonate	0.4
Ammonium Persulfate	0.5
Water	150

Polymerization took place in a 5 L, four-necked round bottom flask equipped with a paddle stirrer, a thermometer, N_2 inlet, and a reflux condenser by using semi-continuous emulsion polymerization procedure.

Table A.3: The amount of CNC dispersion added to 15 g base latex and the resulting solid content in the blends.

Samples	Solid content (wt%)[a]	CNC dispersion (g)[b]
CNC dispersion	5.5	-
MAA5-neat	39.4	0
1 wt%	37.1	1.09
3 wt%	33.3	3.29
5 wt%	30.1	5.67
8 wt%	26.4	9.34
10 wt%	24.4	11.96
15 wt%	20.5	18.96
MAA10-neat	39.4	0
1 wt%	37.1	1.09
3 wt%	33.3	3.29
5 wt%	30.1	5.67
8 wt%	26.4	9.34
10 wt%	24.4	11.96
15 wt%	20.5	18.96

[a]The solid content of composite latexes after mixing with cellulose dispersion.
[b]The amount of CNC dispersion added to 15 g latex to prepare the composite latexes.

Table A.4: pH, average particle size and zeta potential measurements of CNC dispersion and latex/CNC composite blends.

Samples	pH	z-average (nm)	Zeta potential (mV $\pm$ SD[a])
CNC dispersion	6.10	114 $\pm$ 2	-46.9 $\pm$ 19.3
MAA5-neat	8.18	117 $\pm$ 2	-44.1 $\pm$ 18.1
1 wt%	8.15	114 $\pm$ 3	-46.5 $\pm$ 16.3
3 wt%	8.10	117 $\pm$ 1	-46.3 $\pm$ 15.0
5 wt%	8.17	118 $\pm$ 2	-47.9 $\pm$ 13.4
8 wt%	8.23	118 $\pm$ 3	-47.1 $\pm$ 17.6
10 wt%	8.24	118 $\pm$ 3	-47.2 $\pm$ 17.1
15 wt%	8.03	116 $\pm$ 3	-45.2 $\pm$ 14.4
MAA10-neat	7.37	116 $\pm$ 1	-47.7 $\pm$ 15.2
1 wt%	7.34	115 $\pm$ 2	-48.8 $\pm$ 15.2
3 wt%	7.32	116 $\pm$ 3	-49.8 $\pm$ 17.1
5 wt%	7.29	116 $\pm$ 3	-49.7 $\pm$ 17.3
8 wt%	7.27	115 $\pm$ 2	-48.3 $\pm$ 13.6
10 wt%	7.31	117 $\pm$ 3	-49.8 $\pm$ 15.5
15 wt%	7.23	119 $\pm$ 2	-49.4 $\pm$ 14.8

[a]SD: Standard deviation in the zeta potential distribution.

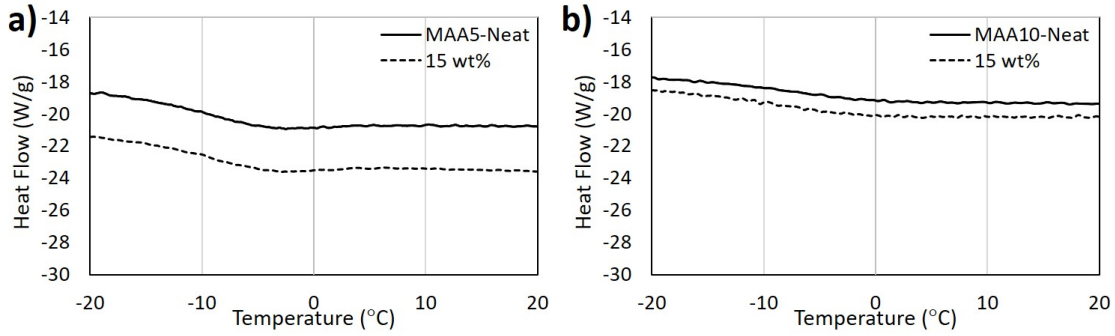

Figure A.1: DSC heat flow curves pointing glass transition temperatures of latexes: a) MAA5 and b) MAA10.

The theoretical T_g for the latexes, calculated using the Flory-Fox equation [191] from T_g and mass fraction of the homopolymers (polyBA, polyMMA, and polyMAA), were -6.8 °C (MAA5) and -10.5 °C (MAA10), similar to those obtained from DSC.

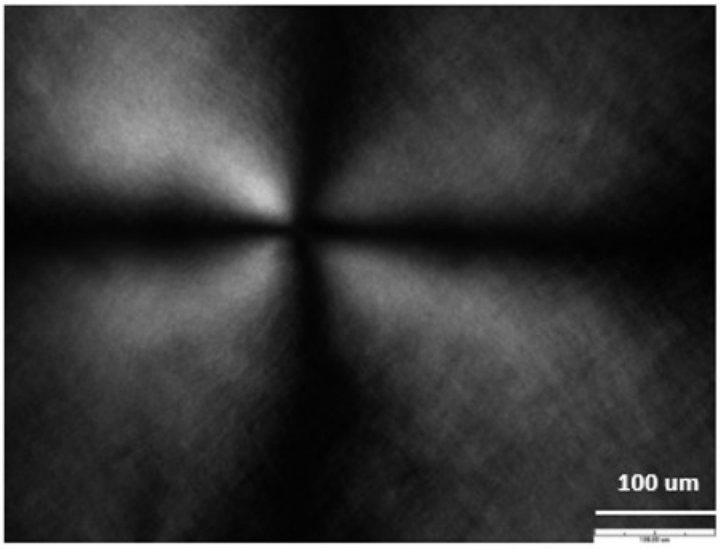

Figure A.2: Example of a Maltese cross pattern visible between crossed polarizers.

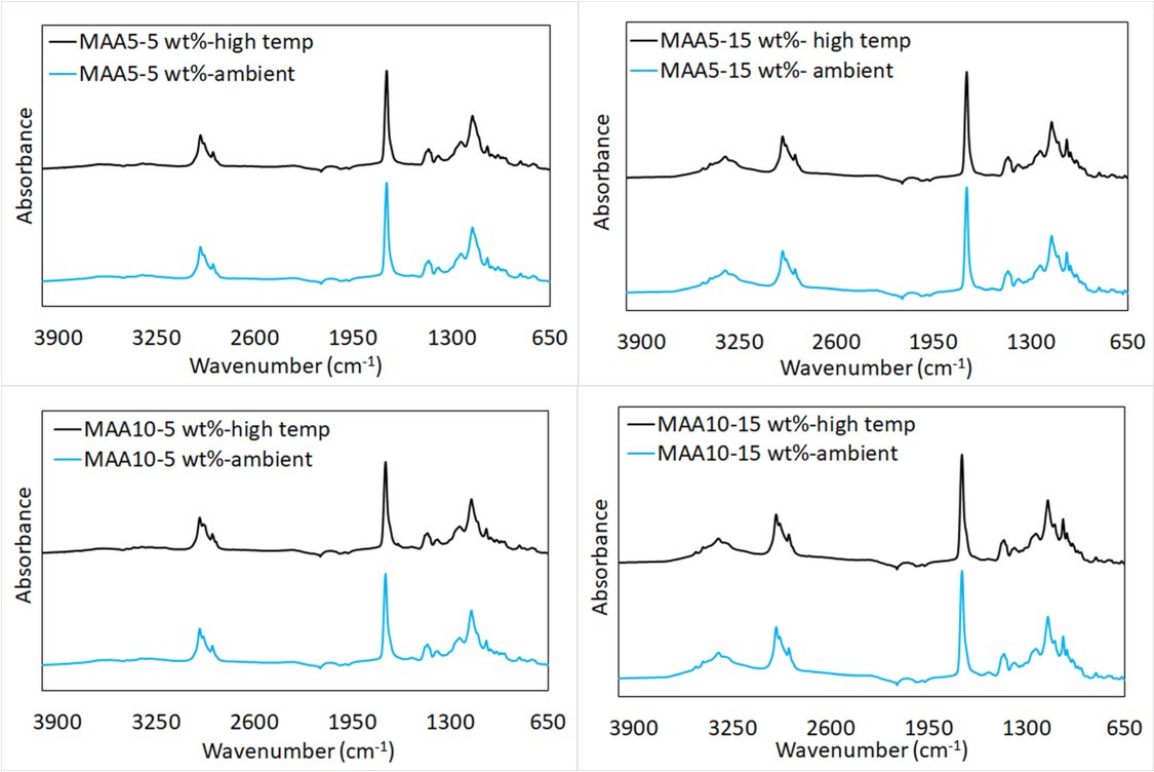

Figure A.3: ATR-FTIR spectra of 5 and 15 wt% CNC loaded latex films dried at ambient temperature and high temperature.

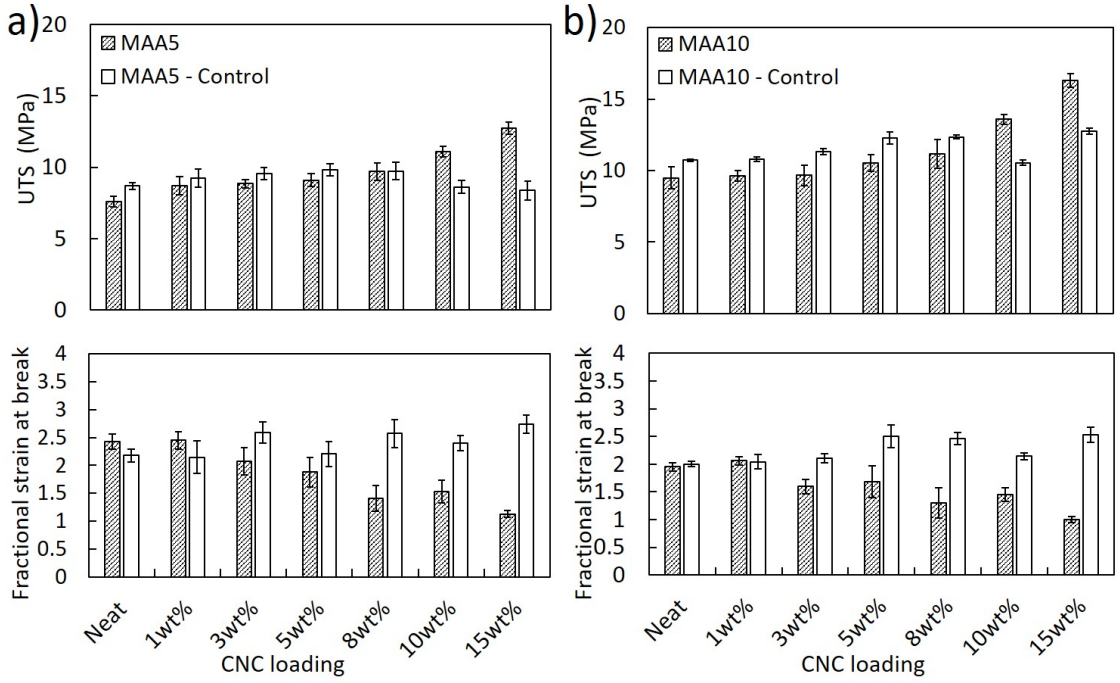

Figure A.4: Biaxial tensile test results of neat and CNC loaded latex films prepared with added water: a) MAA5, b) MAA10.

We prepared control samples that do not contain CNCs by diluting the latexes with the same amount of water in the CNC dispersions. The resulting films were tested by biaxial tensile load. We obtained a similar tensile strength in each control film, suggesting that water content in the latex dispersion did not affect the mechanical performance.

Table A.5: Young's modulus (MPa) values of neat and CNC loaded latex films.

CNC loading	Young's modulus (MPa)	
(wt%)	MAA5	MAA10
0	14 ± 1.6	17 ± 0.3
5	85 ± 8.2	94 ± 2.4
15	488 ± 31.0	583 ± 46.8

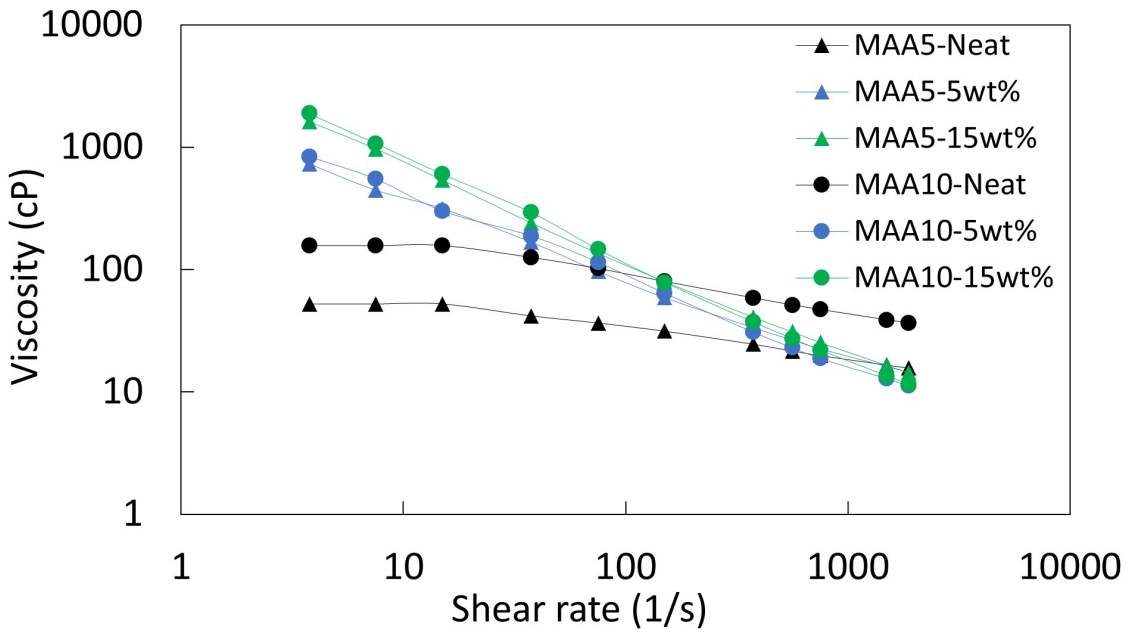

Figure A.5: Viscosity of neat and CNC loaded latexes as a function of shear rate.

Viscosity of each sample was measured by using Brookfield DV3T Viscometer at ambient temperature.

APPENDIX B

SUPPORTING INFORMATION FOR CHAPTER 3

B.1 Tables

Table B.1: The measured N wt% and the calculated degree of substitution for umCNC and mCNC samples.

		Sample name	N wt% ± 0.3	Degree of substitution (DS) ± 0.04
		umCNC	0	0
		30C-6h	1.28	0.17
50C	samples	50C-2h	1.89	0.28
		50C-6h	2.16	0.33
		50C-12h	2.28	0.35
		50C-18h	2.14	0.32
		50C-24h	2.47	0.39
65C	samples	65C-30m	2.73	0.45
		65C-2h	4.73	1.15
		65C-6h	5.46	1.6
		65C-18h	5.86	1.93

DS is the number of hydroxyl groups modified per AGU. N wt% is calculated by using DS and molecular weights of Nitrogen, CNC and IEM.

$$N\% = \frac{DS \times 14.007}{162.141 + DS \times 155.153} \times 100$$

DS becomes:

$$DS = \frac{162.141 \times N\%}{14.007 \times 100 - 155.153 \times N\%}$$

Table B.2: Composition, molecular weight, polydispersity, and T_g of free polymers of the copolymers.

Properties	Copolymers		
	Neat acrylic	umCNC/acrylic	gmCNC/acrylic
Monomer composition (wt%)	58% MMA/42% BA	58% MMA/42% BA	48% MMA/52% BA
M_n (g/mol)	62003	63042	63971
M_w (g/mol)	127041	121413	120082
PDI (M_w/M_n)	2.01	1.93	1.88
T_g (°C)	26.5 $\pm$ 1	27.2 $\pm$ 1	29.1 $\pm$ 1

B.2 Calculations

B.2.1 Calculation of AGU:IEM molar ratio in mCNC

The molar of AGU units relative to the anchored IEM units was evaluated based on the elemental composition of mCNC and details of the calculation are given below.

	C (12.01 g)	H (1.01 g)	N (14.01 g)	S (32.07g)
mCNC (50C-2h)	44.2	6.1	1.7	0.96

Let us assume that we have 100 g mCNC.

$$n(N) = \frac{100 \times 1.7/100}{14.01} = 0.12\ mol$$

$$n(C) = \frac{100 \times 44.2/100}{12.01} = 3.68\ mol$$

There are 6 C in one AGU ($C_6H_{10}O_5$) and 7 C in one IEM ($C_7H_9NO_3$) unit.

$$n(C) = 6 \times n(AGU) + 7 \times n(IEM) = 3.68\ mol$$

$$n(IEM) = n(N) = 0.12\ mol$$

$$n(AGU) = \frac{3.68 - 7 \times 0.12}{6} = 0.473\ mol$$

$$\frac{n(AGU)}{n(IEM)} = \frac{0.473\ mol}{0.12\ mol} = 3.94$$

The molecular formula of mCNC: $(C_6H_{10}O_5)_{3.94}(C_7H_9NO_3)_1$.

B.2.2 Calculation of surface hydroxyl conversion

We first calculated the surface hydroxyl groups by referring to the study by Brand et al. [192] based on the lateral dimensions and lattice parameters of the CNCs. We used the lattice parameters from work by Wu et al. [193] for cellulose I monoclinic unit cells and assumed a square-shape geometry for the CNCs.

$$OH_s\% = 100 \times \left(\frac{d_{(1\bar{1}0)} + d_{(110)}}{h}\right) = 100 \times \left(\frac{0.61\ nm + 0.54\ nm}{4\ nm}\right) = 28.8\%$$

$$n(OH) : n(Glu) = 3 \qquad n(OH_s) : n(Glu) = 3 \times 0.288 = 0.864$$

The percent of hydroxyl groups reacted with IEM on the CNC surface was calculated by using the results obtained from elemental analyses of mCNCs. An example of the calculation is shown below for the 50C-2h sample. The calculation method is adapted from Ref. [194].

	C (12.01 g)	H (1.01 g)	N (14.01 g)	S (32.07 g)
umCNC	41.69	6.23	0	1.02
mCNC	44.50	6.18	1.89	0.95

Let us assume that we have 100 g CNC.

In umCNC:

$$n(S) = \frac{100 \times 0.95/100}{32.07} = 0.03\ mol = n(SO_3)$$

$$n(C) = \frac{100 \times 41.69/100}{12.01} = 3.47\ mol$$

$$n(AGU) = \frac{n(C)}{6} = \frac{3.47}{6} = 0.58\ mol$$

$$n(SO_3) : n(AGU) = \frac{0.03}{0.58} = 0.052$$

In mCNC:

$$n(N) = \frac{100 \times 1.89/100}{14.01} = 0.13\ mol = n(IEM)$$

$$n(C) = \frac{100 \times 44.50/100}{12.01} = 3.71\ mol$$

$$n(AGU) = \frac{n(C) - 7 \times n(IEM)}{6} = 0.46\ mol$$

$$n(IEM) : n(AGU) = 0.29$$

$$\%OH\ conversion = \frac{n(IEM) : n(AGU)}{n(OH_s) : n(Glu) - n(SO_3) : n(Glu)} \times 100\% = 36.7\%$$

B.2.3 Calculation of BA/MMA ratio in the grafted polymer

	C (12.01 g)	H (1.01 g)	N (14.01 g)	S (32.07 g)
gmCNC	52.8	7.3	0.7	0.38

Assuming that we have 100 g gmCNC:

$$n(N) = \frac{100 \times 0.7/100}{14.01} = 0.05\ mol = n(IEM)$$

The molar AGU:IEM ratio was found to be 3.94 in the previous section.

$$n(AGU) = 3.94 \times n(IEM) = 0.19\ mol$$

Carbon balance:

$$n(C)_{gmCNC} = n(C)_{mCNC} + n(C)_{polymer} = \frac{100 \times 52.8/100}{12.01} = 4.39\ mol$$

There are 6 C in one AGU ($C_6H_{10}O_5$) and 7 C in one IEM ($C_7H_9NO_3$) unit.

$$n(C)_{mCNC} = 6 \times n(AGU) + 7 \times n(IEM) = 6 \times 0.19 + 7 \times 0.05 = 1.52\ mol$$

$$n(C)_{polymer} = 4.39 - 1.52 = 2.87\ mol$$

Hydrogen balance:

$$n(H)_{gmCNC} = n(H)_{mCNC} + n(H)_{polymer} = \frac{100 \times 7.3/100}{1.01} = 7.18\ mol$$

There are 10 H in one AGU ($C_6H_{10}O_5$) and 9 H in one IEM ($C_7H_9NO_3$) unit.

$$n(H)_{mCNC} = 10 \times n(AGU) + 9 \times n(IEM) = 10 \times 0.19 + 9 \times 0.05 = 2.39\ mol$$

$$n(H)_{polymer} = 7.18 - 2.39 = 4.79\ mol$$

The molecular formula of MMA/BA copolymer: $(C_5H_8O_2)_m(C_7H_{12}O_2)_n$.

$$n(C)_{polymer} = 5 \times m + 7 \times n = 2.87\ mol$$

$$n(H)_{polymer} = 8 \times m + 12 \times n = 4.79\ mol$$

where $m = 0.25$ and $n = 0.24$.

Mass of 0.25 mol MMA: $m(C_5H_8O_2) = 25.03\ g$

Mass of 0.24 mol BA: $m(C_7H_{12}O_2) = 30.76\ g$

$$m(polymer) = m(C_5H_8O_2) + m(C_7H_{12}O_2) = 55.79\ mol$$

$m(mCNC) = m(gmCNC) - m(polymer)$ (we assumed gmCNC as 100 g.)

$$m(mCNC) = 100 - 55.79 = 44.02\ g$$

Based on this calculation, 56 wt% of gmCNC is the grafted polymer and the composition of the grafted polymer is 44.9 wt% MMA/55.1 wt% BA. We found the estimated composition consistent with the composition calculated form weight loss curve of TGA.

gmCNC was analyzed by TGA and the composition of gmCNC was found to be 42.6 wt% mCNC/57.1 wt% polymer. The weight ratio of the grafted polymer to mCNC is 1.34. We added the residual amount to mCNC composition since the residual mass of neat polymer was less than 0.5 wt%.

B.2.4 Calculation of $M_n^{grafted\ BA/MMA}$ using TGA

The molecular composition of mCNC found in the previous section: $(C_6H_{10}O_5)_{3.94}(C_7H_9NO_3)_1$. The molecular composition of gmCNC can be simplified as:

$$(C_6H_{10}O_5)_{3.94}(C_7H_9NO_3)_1(C_5H_8O_2)_m(C_7H_{12}O_2)_n$$

The molar ratio of monomers to IEM are calculated as:

$$\frac{n(MMA)}{n(IEM)} = 5 \quad \text{and} \quad \frac{n(BA)}{n(IEM)} = 4.8$$

So, the molecular composition becomes $(C_6H_{10}O_5)_{3.94}(C_7H_9NO_3)_1(C_5H_8O_2)_5(C_7H_{12}O_2)_{4.8}$. We can check the weight ratio of the polymer to mCNC by using the estimated molecular formula.

$$m(mCNC) = m[(C_6H_{10}O_5)_{3.94}(C_7H_9NO_3)_1] = 3.94 \times 162.15\ g + 1 \times 155.16\ g = 794\ g$$

$$m(polymer) = m[(C_5H_8O_2)_5(C_7H_{12}O_2)_{4.8}] = 5 \times 100.12\ g + 4.18 \times 128.18\ g = 1115\ g$$

$\frac{m(polymer)}{m(mCNC)} = \frac{1115\ g}{794\ g} = 1.40$ which is consistent with the weight ratio obtained from TGA.

According to the protocol published by Zhang et al. [162]:

One mole of gmCNC contains 1115 g BA/MMA copolymer: $M_n^{grafted\ polymer} = 1115$

g/mol. Average molecular weight of monomer unit for 44.9 wt% MMA/55.1 wt% BA = 111.9 g/mol.

So, the number average degree of polymerization is approximately 10 units.

B.2.5 Calculation of surface area of CNC

Based on the calculation by Majoinen et al. [195], we assumed an infinitely long cylinder resembling the CNCs with a diameter 3.8 nm (measured by AFM) and work with a cylindrical volume segment with a length of 1 nm.

Volume of the segment: 11.34 nm^3

Surface area of the segment: 11.94 nm^2

By using the density of CNC (1.6 g/mol), the mass of the volume segment was found and used to calculate specific surface area (A) of the CNC.

$$A = \frac{m_{segment}}{V_{segment}} = \frac{11.94\ nm^2}{1.81 \times 10^{-20}\ g} = 658 \times 10^{20}\ nm^2/g = 658\ m^2/g$$

B.2.6 Calculation of grafting density of the polymer

Grafting density (σ) is calculated by using the equation below [196].

$$\sigma = \frac{\frac{wt\%}{100} \times N_A}{M_n \times A}$$

$$\sigma = \frac{\frac{57.1}{100} \times N_A}{1115\ g/mol \times 6.58 \times 10^{20}\ nm^2/g} = 0.47\ \frac{chains}{nm^2}$$

APPENDIX C

SUPPORTING INFORMATION FOR CHAPTER 4

C.1 Figures

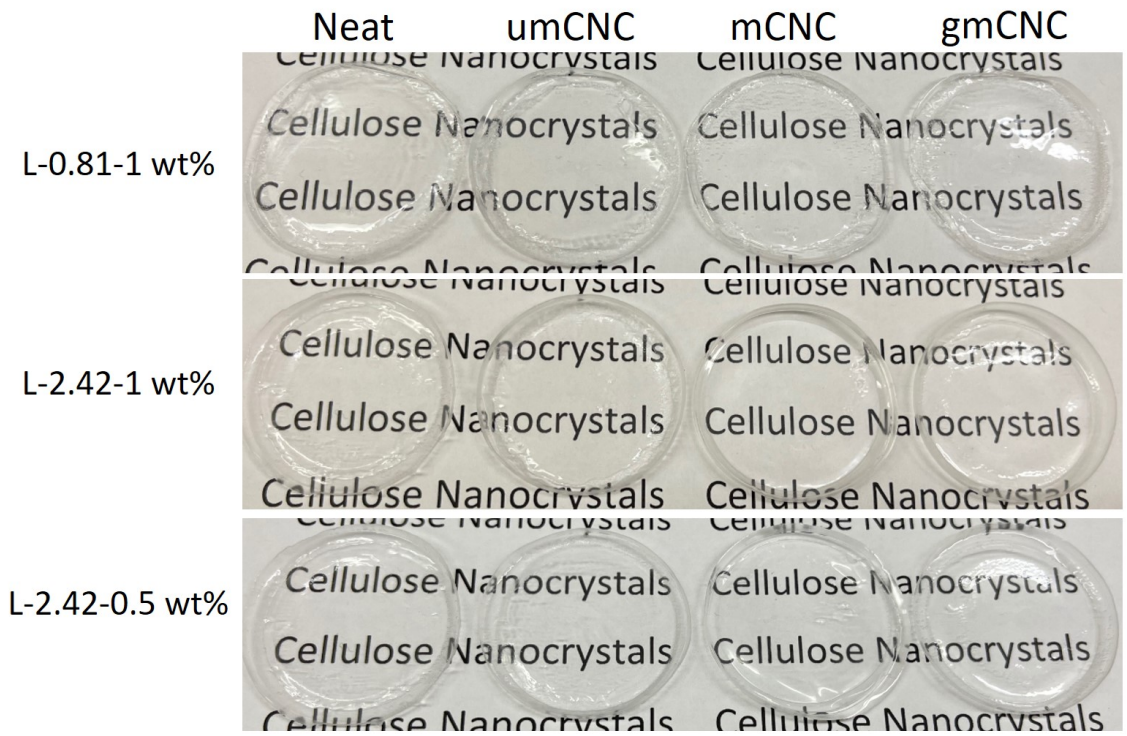

Figure C.1: Dried latex films used for mechanical testing.

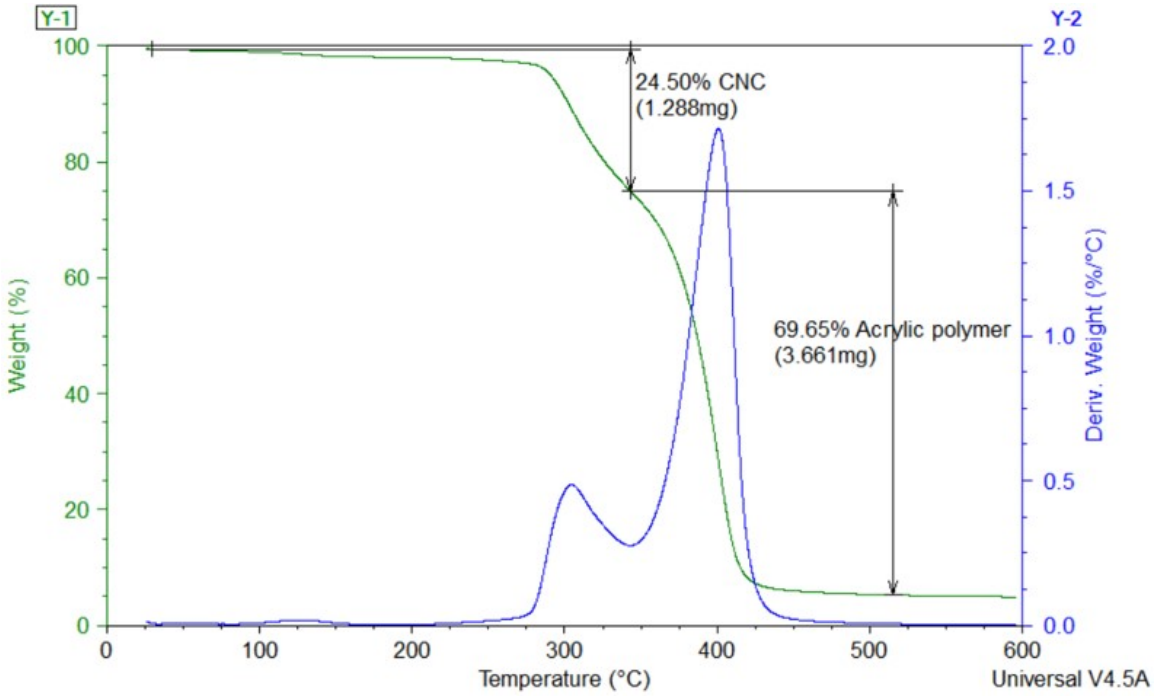

Figure C.2: Calculation of relative weight changes of CNCs and the attached polymer from the weight loss curve of gmCNC.

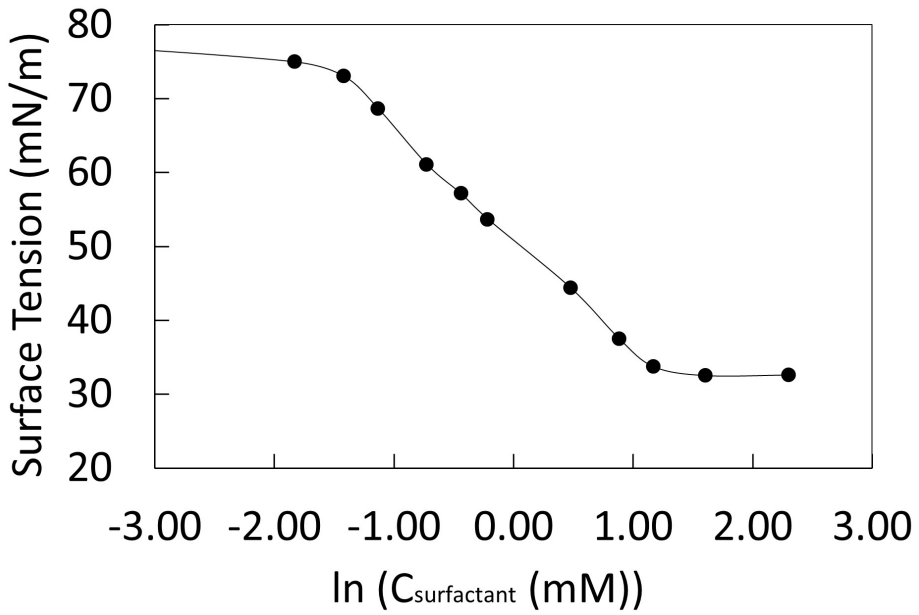

Figure C.3: Surface tension measurements of aqueous SDBS solution as a function of surfactant concentration (CMC = 2.95 mM).

C.2 Tables

Table C.1: Elemental analysis results of latex films and coagula for carbon (C), hydrogen (H), and nitrogen (N) – L represents latex films and C stands for coagulum.

Samples	Elements (wt%) ± 0.3 wt%		
	C	H	N
L-0.81-Neat	61.85	8.53	0
C-0.81-Neat	62.49	8.75	0
L-0.81-umCNC-1 wt%	60.78	8.5	0
C-0.81-umCNC-1 wt%	62.85	8.75	0
L-0.81-mCNC-1 wt%	61.68	8.69	0
C-0.81-mCNC-1 wt%	56.81	8.15	0.97
L-0.81-gmCNC-1 wt%	61.16	8.67	0
C-0.81-gmCNC-1 wt%	61.29	8.64	0
L-2.42-Neat	60.57	8.55	0
C-2.42-Neat	62.52	8.74	0
L-2.42-umCNC-1 wt%	60.82	8.46	0
C-2.42-umCNC-1 wt%	62.71	8.83	0
L-2.42-umCNC-0.5 wt%	61.63	8.6	0
C-2.42-umCNC-0.5 wt%	62.63	8.81	0
L-2.42-mCNC-1 wt%	61.25	8.61	0
C-2.42-mCNC-1 wt%	59.62	8.43	0.75
L-2.42-mCNC-0.5 wt%	61.24	8.62	0
C-2.42-mCNC-0.5 wt%	59.84	8.4	0.5
L-2.42-gmCNC-1 wt%	61.47	8.64	0
C-2.42-gmCNC-1 wt%	61.72	8.67	0
L-2.42-gmCNC-0.5 wt%	61.77	8.73	0
C-2.42-gmCNC-0.5 wt%	62.91	8.79	0

Table C.2: Storage modulus (MPa), loss modulus (MPa), and tanδ of latex films as a function of frequency obtained from DMA.

Frequency (Hz)	Storage modulus (MPa)	Loss modulus (MPa)	tanδ	Storage modulus (MPa)	Loss modulus (MPa)	tanδ
	L-2.42 -Neat			L-0.81 -Neat		
0.1	20	16	0.78	18	17	0.95
1	54	32	0.6	60	38	0.64
10	125	62	0.5	149	86	0.58
100	250	107	0.43	302	153	0.51
	L-2.42-umCNC-1 wt%			L-0.81-umCNC-1 wt%		
0.1	28	15	0.54	24	22	0.92
1	69	34	0.49	60	43	0.72
10	148	70	0.47	131	82	0.63
100	288	124	0.43	252	140	0.55
	L-2.42-mCNC-1 wt%			L-0.81-mCNC-1 wt%		
0.1	16	13	0.83	16	13	0.87
1	40	40	1	50	35	0.71
10	121	90	0.74	125	93	0.74
100	282	163	0.58	310	184	0.56
	L-2.42-gmCNC-1 wt%			L-0.81-gmCNC-1 wt%		
0.1	17	13	0.77	15	13	0.87
1	45	31	0.68	39	31	0.79
10	108	68	0.63	139	95	0.69
100	245	136	0.55	329	209	0.63
	L-2.42-umCNC-0.5 wt%					
0.1	30	20	0.66			
1	70	33	0.47			
10	130	58	0.46			
100	239	101	0.42			
	L-2.42-mCNC-0.5 wt%					
0.1	15	16	1.06			
1	47	33	0.71			
10	103	66	0.64			
100	256	137	0.53			
	L-2.42-gmCNC-0.5 wt%					
0.1	15	17	1.12			
1	37	42	1.14			
10	104	70	0.67			
100	210	101	0.48			

C.3 Calculations

C.3.1 Calculation of AGU:IEM molar ratio in mCNC

The molar of AGU units relative to the anchored IEM units was evaluated based on the elemental composition of mCNC and details of the calculation are given below.

	C (12.01 g)	H (1.01 g)	N (14.01 g)	S (32.07g)
mCNC (65C-30m)	45.36	6.10	2.87	0.85

Let us assume that we have 100 g mCNC.

$$n(N) = \frac{100 \times 2.87/100}{14.01} = 0.205\ mol$$

$$n(C) = \frac{100 \times 45.36/100}{12.01} = 3.78\ mol$$

There are 6 C in one AGU ($C_6H_{10}O_5$) and 7 C in one IEM ($C_7H_9NO_3$) unit.

$$n(C) = 6 \times n(AGU) + 7 \times n(IEM) = 3.78\ mol$$

$$n(IEM) = n(N) = 0.205\ mol$$

$$n(AGU) = \frac{3.78 - 7 \times 0.205}{6} = 0.391\ mol$$

$$\frac{n(AGU)}{n(IEM)} = \frac{0.391\ mol}{0.205\ mol} = 1.91$$

The molecular formula of mCNC: $(C_6H_{10}O_5)_{1.91}(C_7H_9NO_3)_1$.

C.3.2 Calculation of surface hydroxyl conversion

We first calculated the surface hydroxyl groups by referring to the study by Brand et al. [192] based on the lateral dimensions and lattice parameters of the CNCs. We used the lattice parameters from work by Wu et al. [193] for cellulose I monoclinic unit cells and assumed a square-shape geometry for the CNCs.

$$OH_s\% = 100 \times \left(\frac{d_{(1\bar{1}0)} + d_{(110)}}{h}\right) = 100 \times \left(\frac{0.61\ nm + 0.54\ nm}{4\ nm}\right) = 28.8\%$$

$$n(OH) : n(Glu) = 3 \qquad n(OH_s) : n(Glu) = 3 \times 0.288 = 0.864$$

The percent of hydroxyl groups reacted with IEM on the CNC surface was calculated by using the results obtained from elemental analyses of mCNCs. The calculation method is adapted from Ref. [194].

	C (12.01 g)	H (1.01 g)	N (14.01 g)	S (32.07 g)
umCNC	40.58	6.22	0	1.1
mCNC	45.36	6.10	2.87	0.85

Let us assume that we have 100 g CNC.

In umCNC:

$$n(S) = \frac{100 \times 1.1/100}{32.07} = 0.034\ mol = n(SO_3)$$

$$n(C) = \frac{100 \times 40.58/100}{12.01} = 3.38\ mol$$

$$n(AGU) = \frac{n(C)}{6} = \frac{3.38}{6} = 0.56\ mol$$

$$n(SO_3) : n(AGU) = \frac{0.034}{0.56} = 0.061$$

In mCNC:

$$n(N) = \frac{100 \times 2.87/100}{14.01} = 0.205\ mol = n(IEM)$$

$$n(C) = \frac{100 \times 45.36/100}{12.01} = 3.78\ mol$$

$$n(AGU) = \frac{n(C) - 7 \times n(IEM)}{6} = 0.391\ mol$$

$$n(IEM) : n(AGU) = 0.524$$

$$\%OH\ conversion = \frac{n(IEM) : n(AGU)}{n(OH_s) : n(Glu) - n(SO_3) : n(Glu)} \times 100\% = 65\%$$

C.3.3 Calculation of BA/MMA ratio in the grafted polymer

	C (12.01 g)	H (1.01 g)	N (14.01 g)	S (32.07 g)
gmCNC	56.50	7.70	0.66	0.31

Assuming that we have 100 g gmCNC:

$$n(N) = \frac{100 \times 0.66/100}{14.01} = 0.047\ mol = n(IEM)$$

The molar AGU:IEM ratio was found to be 1.91 in the previous section.

$$n(AGU) = 1.91 \times n(IEM) = 0.090\ mol$$

Carbon balance:

$$n(C)_{gmCNC} = n(C)_{mCNC} + n(C)_{polymer} = \frac{100 \times 56.5/100}{12.01} = 4.70\ mol$$

There are 6 C in one AGU ($C_6H_{10}O_5$) and 7 C in one IEM ($C_7H_9NO_3$) unit.

$$n(C)_{mCNC} = 6 \times n(AGU) + 7 \times n(IEM) = 6 \times 0.090 + 7 \times 0.047 = 0.87\ mol$$

$$n(C)_{polymer} = 4.70 - 0.87 = 3.83\ mol$$

Hydrogen balance:

$$n(H)_{gmCNC} = n(H)_{mCNC} + n(H)_{polymer} = \frac{100 \times 7.70/100}{1.01} = 7.62\ mol$$

There are 10 H in one AGU ($C_6H_{10}O_5$) and 9 H in one IEM ($C_7H_9NO_3$) unit.

$$n(H)_{mCNC} = 10 \times n(AGU) + 9 \times n(IEM) = 10 \times 0.089 + 9 \times 0.047 = 1.32\ mol$$

$$n(H)_{polymer} = 7.62 - 1.32 = 6.30\ mol$$

The molecular formula of MMA/BA copolymer: $(C_5H_8O_2)_m(C_7H_{12}O_2)_n$.

$$n(C)_{polymer} = 5 \times m + 7 \times n = 3.83\ mol$$

$$n(H)_{polymer} = 8 \times m + 12 \times n = 6.30\ mol$$

where $m = 0.477$ and $n = 0.207$.

Mass of 0.477 mol MMA: $m(C_5H_8O_2) = 48.0\ g$

Mass of 0.207 mol BA: $m(C_7H_{12}O_2) = 26.3\ g$

$$m(polymer) = m(C_5H_8O_2) + m(C_7H_{12}O_2) = 74.3\ mol$$

$$m(mCNC) = m(gmCNC) - m(polymer) \qquad \text{(we assumed gmCNC as 100 g.)}$$

$$m(mCNC) = 100 - 74.3 = 25.7\ g$$

Based on this calculation, 74.3 wt% of gmCNC is the grafted polymer and the composition of the grafted polymer is 64.6 wt% MMA/35.4 wt% BA.

C.3.4 Calculation of $M_n^{grafted\ BA/MMA}$ using TGA

The molecular composition of mCNC found in the previous section: $(C_6H_{10}O_5)_{1.91}(C_7H_9NO_3)_1$.

The molecular composition of gmCNC can be simplified as:

$$(C_6H_{10}O_5)_{1.91}(C_7H_9NO_3)_1(C_5H_8O_2)_m(C_7H_{12}O_2)_n$$

The molar ratio of monomers to IEM are calculated as:

$$\frac{n(MMA)}{n(IEM)} = 10.17 \quad \text{and} \quad \frac{n(BA)}{n(IEM)} = 4.36$$

So, the molecular composition becomes $(C_6H_{10}O_5)_{1.91}(C_7H_9NO_3)_1(C_5H_8O_2)_{10.17}(C_7H_{12}O_2)_{4.36}$.

According to the protocol published by Zhang et al. [162]:

One mole of gmCNC contains $10.17 \times 100.12 + 4.36 \times 128.17 = 1577$ g BA/MMA copolymer: $M_n^{grafted\ polymer} = 1577$ g/mol.

Average molecular weight of monomer unit for 64.6 wt% MMA/35.4 wt% BA = 110 g/mol.

So, the number average degree of polymerization is approximately 15 units.

C.3.5 Calculation of surface area of CNC

Based on the calculation by Majoinen et al. [195], we assumed an infinitely long cylinder resembling the CNCs with a diameter 3.8 nm (measured by AFM) and work with a cylindrical volume segment with a length of 1 nm.

Volume of the segment: 11.34 nm^3

Surface area of the segment: 11.94 nm^2

By using the density of CNC (1.6 g/mol), the mass of the volume segment was found and used to calculate specific surface area (A) of the CNC.

$$A = \frac{m_{segment}}{V_{segment}} = \frac{11.94\ nm^2}{1.81 \times 10^{-20}\ g} = 658 \times 10^{20}\ nm^2/g = 658\ m^2/g$$

C.3.6 Calculation of grafting density of the polymer

Grafting density (σ) is calculated by using the equation below [196].

$$\sigma = \frac{\frac{wt\%}{100} \times N_A}{M_n \times A}$$

$$\sigma = \frac{\frac{70}{100} \times N_A}{1577\ g/mol \times 6.58 \times 10^{20}\ nm^2/g} = 0.41\ \frac{chains}{nm^2}$$

REFERENCES

[1] Wicks, Z. W., Jones, F. N., Pappas, S. P., and Wicks, D. A., "What are Coatings?" In *Organic Coatings: Science and Technology*. 2007, pp. 1–6. DOI: https://doi.org/10.1002/9780470079072.ch1.

[2] Lambourne, R., "1 - Paint composition and applications — a general introduction," in *Paint and Surface Coatings (Second Edition)*, R. Lambourne and T. A. Strivens, Eds. Woodhead Publishing, 1999, pp. 1–18, ISBN: 978-1-85573-348-0. DOI: https://doi.org/10.1533/9781855737006.1.

[3] Ghosh, S. K., "Functional Coatings and Microencapsulation: A General Perspective," in *Functional Coatings*. 2006, pp. 1–28. DOI: https://doi.org/10.1002/3527608478.ch1.

[4] "Introduction," in *Paints, Coatings and Solvents*. 1998, pp. 1–10. DOI: https://doi.org/10.1002/9783527611867.ch1.

[5] Resins in Paints and Coatings Market - Growth, Trends, Covid-19 Impact, and Forecasts (2021-2026). 2020. Available from: https://www.mordorintelligence.com/industry-reports/resins-in-paints-and-coatings-market, Accessed: April 22, 2021.

[6] Paints and Coatings Market by Product (High Solids, Powder, Waterborne, Solventborne), By Material (Acrylic, Alkyd, Polyurethane, Epoxy & Polyesters), By Application, And Segment Forecasts, 2018 - 2025. 2017, Grand View Research.

[7] Paint and Coatings Industry Overview. Chemical Economics Handbook 2017. Available from: https://ihsmarkit.com/products/paint-and-coatings-industry-chemical-economics-handbook.html, Accessed: April 1, 2019.

[8] Price, T. I. and Turner, S., "Solvent-Borne Thermosetting Acrylics," in *Surface Coatings: Volume 1 Raw Materials and Their Usage*. Dordrecht: Springer Netherlands, 1993, pp. 247–262, ISBN: 978-94-011-1220-8. DOI: 10.1007/978-94-011-1220-8_16.

[9] Ren, X., Meng, L., and Soucek, M., "Environmentally Friendly Coatings," in *Biobased and Environmental Benign Coatings*. 2016, pp. 183–223. DOI: https://doi.org/10.1002/9781119185055.ch8.

[10] Grandhee, S., "Applications for Automotive Coatings," in *Polymer Dispersions and Their Industrial Applications*. 2002, pp. 163–189. DOI: https://doi.org/10.1002/3527600582.ch7.

[11] Srivastava, S., "Co-polymerization of Acrylates," *Designed Monomers and Polymers*, vol. 12, no. 1, pp. 1–18, 2009, ISSN: null. DOI: 10.1163/156855508X391103.

[12] Schork, F. J., Luo, Y., Smulders, W., Russum, J. P., Butté, A., and Fontenot, K., "Miniemulsion Polymerization," in *Polymer Particles*, M. Okubo, Ed. Berlin, Heidelberg: Springer Berlin Heidelberg, 2005, pp. 129–255, ISBN: 978-3-540-31565-0. DOI: 10.1007/b100115.

[13] El-hoshoudy, A., "Emulsion Polymerization Mechanism," in 2018, ISBN: 978-953-51-3746-7. DOI: 10.5772/intechopen.72143.

[14] Dobler, F. and Holl, Y., "Mechanisms of Particle Deformation During Latex Film Formation," in *Film Formation in Waterborne Coatings*, ser. ACS Symposium Series. American Chemical Society, 1996, vol. 648, ch. 2, pp. 22–43, ISBN: 9780841234574. DOI: doi:10.1021/bk-1996-0648.ch00210.1021/bk-1996-0648.ch002.

[15] Winnik, M. A., "Latex film formation," *Current Opinion in Colloid & Interface Science*, vol. 2, no. 2, pp. 192–199, 1997, ISSN: 1359-0294. DOI: https://doi.org/10.1016/S1359-0294(97)80026-X.

[16] Steward, P. A., Hearn, J., and Wilkinson, M. C., "An overview of polymer latex film formation and properties," *Adv Colloid Interface Sci*, vol. 86, no. 3, pp. 195–267, 2000, ISSN: 0001-8686 (Print) 0001-8686. DOI: 10.1016/s0001-8686(99)00037-8.

[17] Keddie, J., *Film formation of latex*. 1997, vol. 21, pp. 101–170. DOI: 10.1016/S0927-796X(97)00011-9.

[18] Wang, Y. and Winnik, M. A., "Effect of a coalescing aid on polymer diffusion in latex films," *Macromolecules*, vol. 23, no. 21, pp. 4731–4732, 1990, ISSN: 0024-9297. DOI: https://doi.org/10.1021/ma00223a038.

[19] US EPA Archive Document - Paint and Coatings. Available from: https://archive.epa.gov/sectors/web/pdf/paintandcoatings-2.pdf, Accessed: April 17, 2019.

[20] United States Environmental Protection Agency. Volatile Organic Compounds' Impact on Indoor Air Quality. Available from: https://www.epa.gov/indoor-air-quality-iaq/volatile-organic-compounds-impact-indoor-air-quality, Accessed: March 12, 2019.

[21] Krieger, S. and Petri, H., "Soft vinyl acetate/ethylene emulsions for high-performance, environmental friendly interior paints," *European Coatings Journal*, p. 44, 2007.

[22] Chang, J. C., Fortmann, R., Roache, N., and Lao, H. C., "Evaluation of low-VOC latex paints," *Indoor Air*, vol. 9, no. 4, pp. 253–8, 1999, ISSN: 0905-6947 (Print) 0905-6947.

[23] Wicks, Z. W., Jones, F. N., Pappas, S. P., and Wicks, D. A., "Polymerization and Film Formation," in *Organic Coatings*. 2007, pp. 7–40. DOI: https://doi.org/10.1002/9780470079072.ch2.

[24] Böckelmann, I., Pfister, E. A., Peters, B., and Duchstein, S., "Psychological effects of occupational exposure to organic solvent mixtures on printers," *Disability and Rehabilitation*, vol. 26, no. 13, pp. 798–807, 2004, ISSN: 0963-8288. DOI: 10.1080/09638280410001696719.

[25] Shuai, J., Kim, S., Ryu, H., Park, J., Lee, C. K., Kim, G.-B., Ultra, V. U., and Yang, W., "Health risk assessment of volatile organic compounds exposure near Daegu dyeing industrial complex in South Korea," *BMC Public Health*, vol. 18, no. 1, p. 528, 2018, ISSN: 1471-2458. DOI: 10.1186/s12889-018-5454-1.

[26] The Paints Directive. Available from: https://ec.europa.eu/environment/air/pollutants/stationary/paints/paints_legis.htm, Accessed: April 24, 2021.

[27] Challener, C. Important Market Trends Impact the Industry in 2016. 2016. Available from: https://www.paint.org/article/important-market-trends-impact-the-industry-in-2016/, Accessed: March 12, 2019.

[28] Geurts, J., Bouman, J., and Overbeek, A., "New waterborne acrylic binders for zero VOC paints," *Journal of Coatings Technology and Research*, vol. 5, no. 1, pp. 57–63, 2008, ISSN: 1935-3804. DOI: 10.1007/s11998-007-9036-x.

[29] Colombini, D., Hassander, H., Karlsson, O. J., and Maurer, F. H. J., "Influence of the Particle Size and Particle Size Ratio on the Morphology and Viscoelastic Properties of Bimodal Hard/Soft Latex Blends," *Macromolecules*, vol. 37, no. 18, pp. 6865–6873, 2004, ISSN: 0024-9297. DOI: 10.1021/ma030455j.

[30] Domingues Dos Santos, F. and Leibler, L., "Large deformation of films from soft-core/hard-shell hydrophobic latices," *Journal of Polymer Science Part B: Polymer Physics*, vol. 41, no. 3, pp. 224–234, 2003, ISSN: 0887-6266. DOI: https://doi.org/10.1002/polb.10379.

[31] Schuler, B., Baumstark, R., Kirsch, S., Pfau, A., Sandor, M., and Zosel, A., "Structure and properties of multiphase particles and their impact on the performance of architectural coatings," *Progress in Organic Coatings*, vol. 40, no. 1, pp. 139–150, 2000, ISSN: 0300-9440. DOI: https://doi.org/10.1016/S0300-9440(00)00136-3.

[32] Keddie, J. L. and Routh, A. F., "Future Directions and Challenges," in *Fundamentals of Latex Film Formation: Processes and Properties*. Dordrecht: Springer Netherlands, 2010, pp. 261–274, ISBN: 978-90-481-2845-7. DOI: 10.1007/978-90-481-2845-7_8.

[33] Lee, D. I. and Chen, F. B., "Development of VOC-free, high-T_g latex binders by a high-temperature water-extended latex technology," *Journal of Coatings Technology and Research*, vol. 4, no. 2, pp. 161–165, 2007, ISSN: 1935-3804. DOI: 10.1007/s11998-007-9016-1.

[34] Klemm, D., Heublein, B., Fink, H.-P., and Bohn, A., "Cellulose: Fascinating Biopolymer and Sustainable Raw Material," *Angewandte Chemie International Edition*, vol. 44, no. 22, pp. 3358–3393, 2005, ISSN: 1433-7851. DOI: https://doi.org/10.1002/anie.200460587.

[35] George, J. and Sabapathi, S. N., "Cellulose nanocrystals: synthesis, functional properties, and applications," *Nanotechnology, science and applications*, vol. 8, pp. 45–54, 2015, ISSN: 1177-8903. DOI: 10.2147/NSA.S64386.

[36] Rowell, R., "Composites from Agri-Based Resources," 1996.

[37] Varshney, V. K. and Naithani, S., "Chemical Functionalization of Cellulose Derived from Nonconventional Sources," in *Cellulose Fibers: Bio- and Nano-Polymer Composites: Green Chemistry and Technology*, S. Kalia, B. S. Kaith, and I. Kaur, Eds. Berlin, Heidelberg: Springer Berlin Heidelberg, 2011, pp. 43–60, ISBN: 978-3-642-17370-7. DOI: 10.1007/978-3-642-17370-7_2.

[38] Staudinger, H., "Über Polymerisation," *Berichte der deutschen chemischen Gesellschaft (A and B Series)*, vol. 53, no. 6, pp. 1073–1085, 1920, ISSN: 0365-9488. DOI: https://doi.org/10.1002/cber.19200530627.

[39] Zugenmaier, P., "Cellulose," in *Crystalline Cellulose and Derivatives: Characterization and Structures*. Berlin, Heidelberg: Springer Berlin Heidelberg, 2008, pp. 101–174, ISBN: 978-3-540-73934-0. DOI: 10.1007/978-3-540-73934-0_5.

[40] Sinha, A., Martin, E., Lim, K.-T., Carrier, D. J., Han, H., Zharov, V., and Kim, J.-W., "Cellulose Nanocrystals as Advanced "Green" Materials for Biological and Biomedical Engineering," *Journal of Biosystems Engineering*, vol. 40, pp. 373–393, 2015. DOI: 10.5307/JBE.2015.40.4.373.

[41] Nishiyama, Y., Langan, P., Wada, M., and Forsyth, V. T., "Looking at hydrogen bonds in cellulose," *Acta Crystallogr D Biol Crystallogr*, vol. 66, no. Pt 11, pp. 1172–7, 2010, ISSN: 0907-4449. DOI: 10.1107/s0907444910032397.

[42] Isogai, A., "Wood nanocelluloses: fundamentals and applications as new bio-based nanomaterials," *Journal of Wood Science*, vol. 59, no. 6, pp. 449–459, 2013, ISSN: 1611-4663. DOI: 10.1007/s10086-013-1365-z.

[43] Jarvis, M. C., "Cellulose Biosynthesis: Counting the Chains," *Plant Physiology*, vol. 163, no. 4, pp. 1485–1486, 2013, ISSN: 0032-0889. DOI: 10.1104/pp.113.231092.

[44] Nixon, B. T., Mansouri, K., Singh, A., Du, J., Davis, J. K., Lee, J.-G., Slabaugh, E., Vandavasi, V. G., O'Neill, H., Roberts, E. M., Roberts, A. W., Yingling, Y. G., and Haigler, C. H., "Comparative Structural and Computational Analysis Supports Eighteen Cellulose Synthases in the Plant Cellulose Synthesis Complex," *Scientific Reports*, vol. 6, no. 1, p. 28 696, 2016, ISSN: 2045-2322. DOI: 10.1038/srep28696.

[45] Lavoine, N., Desloges, I., Dufresne, A., and Bras, J., "Microfibrillated cellulose – Its barrier properties and applications in cellulosic materials: A review," *Carbohydrate Polymers*, vol. 90, no. 2, pp. 735–764, 2012, ISSN: 0144-8617. DOI: https://doi.org/10.1016/j.carbpol.2012.05.026.

[46] Trache, D., Tarchoun, A. F., Derradji, M., Hamidon, T. S., Masruchin, N., Brosse, N., and Hussin, M. H., "Nanocellulose: From Fundamentals to Advanced Applications," *Frontiers in Chemistry*, vol. 8, no. 392, 2020, ISSN: 2296-2646. DOI: 10.3389/fchem.2020.00392.

[47] Börjesson, M. and Westman, G., "Crystalline Nanocellulose - Preparation, Modification, and Properties," in *Cellulose: Fundamental Aspects and Current Trends*. IntechOpen, 2015, ch. 7, pp. 159–191, ISBN: 978-953-51-5059-6. DOI: 10.5772/59889.

[48] Zambrano, F., Starkey, H., Wang, Y., Abbati, C., Venditti, R., Pal, L., Jameel, H., Hubbe, M., Rojas, O., and Gonzalez, R., "Using Micro-and Nanofibrillated Cellulose as a Means to Reduce Weight of Paper Products: A Review," *Bioresources*, vol. 15, 2020. DOI: 10.15376/biores.15.2.Zambrano.

[49] Moon, R. J., Schueneman, G. T., and Simonsen, J., "Overview of Cellulose Nanomaterials, Their Capabilities and Applications," *JOM*, vol. 68, no. 9, pp. 2383–2394, 2016, ISSN: 1543-1851. DOI: https://doi.org/10.1007/s11837-016-2018-7.

[50] Moon, R. J., Martini, A., Nairn, J., Simonsen, J., and Youngblood, J., "Cellulose nanomaterials review: structure, properties and nanocomposites," *Chemical Society Reviews*, vol. 40, no. 7, pp. 3941–3994, 2011, ISSN: 0306-0012. DOI: https://doi.org/10.1039/C0CS00108B.

[51] Saito, T., Kimura, S., Nishiyama, Y., and Isogai, A., "Cellulose Nanofibers Prepared by TEMPO-Mediated Oxidation of Native Cellulose," *Biomacromolecules*, vol. 8, no. 8, pp. 2485–2491, 2007, ISSN: 1525-7797. DOI: 10.1021/bm0703970.

[52] Nickerson, R. F. and Habrle, J. A., "Cellulose Intercrystalline Structure," *Industrial & Engineering Chemistry*, vol. 39, no. 11, pp. 1507–1512, 1947, ISSN: 0019-7866. DOI: 10.1021/ie50455a024.

[53] Klemm, D., Kramer, F., Moritz, S., Lindström, T., Ankerfors, M., Gray, D., and Dorris, A., "Nanocelluloses: A New Family of Nature-Based Materials," *Angewandte Chemie International Edition*, vol. 50, no. 24, pp. 5438–5466, 2011, ISSN: 1433-7851. DOI: https://doi.org/10.1002/anie.201001273.

[54] Beck-Candanedo, S., Roman, M., and Gray, D. G., "Effect of Reaction Conditions on the Properties and Behavior of Wood Cellulose Nanocrystal Suspensions," *Biomacromolecules*, vol. 6, no. 2, pp. 1048–1054, 2005, ISSN: 1525-7797. DOI: https://doi.org/10.1021/bm049300p.

[55] Elazzouzi-Hafraoui, S., Nishiyama, Y., Putaux, J.-L., Heux, L., Dubreuil, F., and Rochas, C., "The Shape and Size Distribution of Crystalline Nanoparticles Prepared by Acid Hydrolysis of Native Cellulose," *Biomacromolecules*, vol. 9, no. 1, pp. 57–65, 2008, ISSN: 1525-7797. DOI: 10.1021/bm700769p.

[56] Hamad, W. Y. and Hu, T. Q., "Structure–process–yield interrelations in nanocrystalline cellulose extraction," *The Canadian Journal of Chemical Engineering*, vol. 88, no. 3, pp. 392–402, 2010, ISSN: 0008-4034. DOI: https://doi.org/10.1002/cjce.20298.

[57] Araki, J., Wada, M., Kuga, S., and Okano, T., "Flow properties of microcrystalline cellulose suspension prepared by acid treatment of native cellulose," *Colloids and Surfaces A: Physicochemical and Engineering Aspects*, vol. 142, no. 1, pp. 75–82, 1998, ISSN: 0927-7757. DOI: https://doi.org/10.1016/S0927-7757(98)00404-X.

[58] Fengel, D. and Wegener, G., *Wood*. De Gruyter, 2011. DOI: doi:10.1515/9783110839654.

[59] Revol, J. F., "On the cross-sectional shape of cellulose crystallites in Valonia ventricosa," *Carbohydrate Polymers*, vol. 2, no. 2, pp. 123–134, 1982, ISSN: 0144-8617. DOI: https://doi.org/10.1016/0144-8617(82)90058-3.

[60] Hanley, S. J., Giasson, J., Revol, J.-F., and Gray, D. G., "Atomic force microscopy of cellulose microfibrils: comparison with transmission electron microscopy," *Polymer*, vol. 33, no. 21, pp. 4639–4642, 1992, ISSN: 0032-3861. DOI: https://doi.org/10.1016/0032-3861(92)90426-W.

[61] Tokoh, C., Takabe, K., Fujita, M., and Saiki, H., "Cellulose Synthesized by Acetobacter Xylinum in the Presence of Acetyl Glucomannan," *Cellulose*, vol. 5, no. 4, pp. 249–261, 1998, ISSN: 1572-882X. DOI: 10.1023/A:1009211927183.

[62] Grunert, M. and Winter, W. T., "Nanocomposites of Cellulose Acetate Butyrate Reinforced with Cellulose Nanocrystals," *Journal of Polymers and the Environment*, vol. 10, no. 1, pp. 27–30, 2002, ISSN: 1572-8900. DOI: 10.1023/A:1021065905986.

[63] Favier, V., Chanzy, H., and Cavaille, J. Y., "Polymer Nanocomposites Reinforced by Cellulose Whiskers," *Macromolecules*, vol. 28, no. 18, pp. 6365–6367, 1995, ISSN: 0024-9297. DOI: 10.1021/ma00122a053.

[64] Terech, P., Chazeau, L., and Cavaille, J. Y., "A Small-Angle Scattering Study of Cellulose Whiskers in Aqueous Suspensions," *Macromolecules*, vol. 32, no. 6, pp. 1872–1875, 1999, ISSN: 0024-9297. DOI: 10.1021/ma9810621.

[65] Vanderfleet, O. M. and Cranston, E. D., "Production routes to tailor the performance of cellulose nanocrystals," *Nature Reviews Materials*, vol. 6, no. 2, pp. 124–144, 2021, ISSN: 2058-8437. DOI: 10.1038/s41578-020-00239-y.

[66] Yu, H., Qin, Z., Liang, B., Liu, N., Zhou, Z., and Chen, L., "Facile extraction of thermally stable cellulose nanocrystals with a high yield of 93% through hydrochloric acid hydrolysis under hydrothermal conditions," *Journal of Materials Chemistry A*, vol. 1, no. 12, pp. 3938–3944, 2013, ISSN: 2050-7488. DOI: 10.1039/C3TA01150J.

[67] Camarero Espinosa, S., Kuhnt, T., Foster, E. J., and Weder, C., "Isolation of Thermally Stable Cellulose Nanocrystals by Phosphoric Acid Hydrolysis," *Biomacromolecules*, vol. 14, no. 4, pp. 1223–1230, 2013, ISSN: 1525-7797. DOI: 10.1021/bm400219u.

[68] Sadeghifar, H., Filpponen, I., Clarke, S. P., Brougham, D. F., and Argyropoulos, D. S., "Production of cellulose nanocrystals using hydrobromic acid and click reactions on their surface," *Journal of Materials Science*, vol. 46, no. 22, pp. 7344–7355, 2011, ISSN: 1573-4803. DOI: 10.1007/s10853-011-5696-0.

[69] Chen, L., Zhu, J. Y., Baez, C., Kitin, P., and Elder, T., "Highly thermal-stable and functional cellulose nanocrystals and nanofibrils produced using fully recyclable organic acids," *Green Chemistry*, vol. 18, no. 13, pp. 3835–3843, 2016, ISSN: 1463-9262. DOI: https://doi.org/10.1039/C6GC00687F.

[70] Bian, H., Chen, L., Dai, H., and Zhu, J. Y., "Effect of fiber drying on properties of lignin containing cellulose nanocrystals and nanofibrils produced through maleic acid hydrolysis," *Cellulose*, vol. 24, no. 10, pp. 4205–4216, 2017, ISSN: 1572-882X. DOI: 10.1007/s10570-017-1430-7.

[71] Reid, M. S., Villalobos, M., and Cranston, E. D., "Benchmarking Cellulose Nanocrystals: From the Laboratory to Industrial Production," *Langmuir*, vol. 33, no. 7, pp. 1583–1598, 2017, ISSN: 0743-7463. DOI: https://doi.org/10.1021/acs.langmuir.6b03765.

[72] Zhong, L., Fu, S., Peng, X., Zhan, H., and Sun, R., "Colloidal stability of negatively charged cellulose nanocrystalline in aqueous systems," *Carbohydrate Polymers*, vol. 90, no. 1, pp. 644–649, 2012, ISSN: 0144-8617. DOI: https://doi.org/10.1016/j.carbpol.2012.05.091.

[73] Rusli, R. and Eichhorn, S. J., "Determination of the stiffness of cellulose nanowhiskers and the fiber-matrix interface in a nanocomposite using Raman spectroscopy," *Applied Physics Letters*, vol. 93, no. 3, p. 033 111, 2008. DOI: 10.1063/1.2963491.

[74] Šturcová, A., Davies, G. R., and Eichhorn, S. J., "Elastic Modulus and Stress-Transfer Properties of Tunicate Cellulose Whiskers," *Biomacromolecules*, vol. 6, no. 2, pp. 1055–1061, 2005, ISSN: 1525-7797. DOI: 10.1021/bm049291k.

[75] Habibi, Y., "Key advances in the chemical modification of nanocelluloses," *Chemical Society Reviews*, vol. 43, no. 5, pp. 1519–1542, 2014, ISSN: 0306-0012. DOI: http://dx.doi.org/10.1039/C3CS60204D.

[76] Habibi, Y., Hoeger, I., Kelley, S. S., and Rojas, O. J., "Development of Langmuir-Schaeffer Cellulose Nanocrystal Monolayers and Their Interfacial Behaviors," *Langmuir*, vol. 26, no. 2, pp. 990–1001, 2010, ISSN: 0743-7463. DOI: 10.1021/la902444x.

[77] Dhar, N., Au, D., Berry, R. C., and Tam, K. C., "Interactions of nanocrystalline cellulose with an oppositely charged surfactant in aqueous medium," *Colloids and Surfaces A: Physicochemical and Engineering Aspects*, vol. 415, pp. 310–319, 2012, ISSN: 0927-7757. DOI: https://doi.org/10.1016/j.colsurfa.2012.09.010.

[78] Brinatti, C., Huang, J., Berry, R. M., Tam, K. C., and Loh, W., "Structural and Energetic Studies on the Interaction of Cationic Surfactants and Cellulose Nanocrystals," *Langmuir*, vol. 32, no. 3, pp. 689–698, 2016, ISSN: 0743-7463. DOI: 10.1021/acs.langmuir.5b03893.

[79] Fraschini, C., Chauve, G., and Bouchard, J., "TEMPO-mediated surface oxidation of cellulose nanocrystals (CNCs)," *Cellulose*, vol. 24, no. 7, pp. 2775–2790, 2017, ISSN: 1572-882X. DOI: 10.1007/s10570-017-1319-5.

[80] Kwon, G., Lee, K., Kim, D., Jeon, Y., Kim, U.-J., and You, J., "Cellulose nanocrystal-coated TEMPO-oxidized cellulose nanofiber films for high performance all-cellulose nanocomposites," *Journal of Hazardous Materials*, vol. 398,

p. 123 100, 2020, ISSN: 0304-3894. DOI: https://doi.org/10.1016/j.jhazmat.2020.123100.

[81] Hasani, M., Cranston, E. D., Westman, G., and Gray, D. G., "Cationic surface functionalization of cellulose nanocrystals," *Soft Matter*, vol. 4, no. 11, pp. 2238–2244, 2008, ISSN: 1744-683X. DOI: 10.1039/B806789A.

[82] Lin, N., Huang, J., Chang, P. R., Feng, J., and Yu, J., "Surface acetylation of cellulose nanocrystal and its reinforcing function in poly(lactic acid)," *Carbohydrate Polymers*, vol. 83, no. 4, pp. 1834–1842, 2011, ISSN: 0144-8617. DOI: https://doi.org/10.1016/j.carbpol.2010.10.047.

[83] Braun, B., Dorgan, J. R., and Hollingsworth, L. O., "Supra-Molecular EcoBio-Nanocomposites Based on Polylactide and Cellulosic Nanowhiskers: Synthesis and Properties," *Biomacromolecules*, vol. 13, no. 7, pp. 2013–2019, 2012, ISSN: 1525-7797. DOI: 10.1021/bm300149w.

[84] Goussé, C., Chanzy, H., Excoffier, G., Soubeyrand, L., and Fleury, E., "Stable suspensions of partially silylated cellulose whiskers dispersed in organic solvents," *Polymer*, vol. 43, no. 9, pp. 2645–2651, 2002, ISSN: 0032-3861. DOI: https://doi.org/10.1016/S0032-3861(02)00051-4.

[85] Follain, N., Belbekhouche, S., Bras, J., Siqueira, G., Marais, S., and Dufresne, A., "Water transport properties of bio-nanocomposites reinforced by Luffa cylindrica cellulose nanocrystals," *Journal of Membrane Science*, vol. 427, pp. 218–229, 2013, ISSN: 0376-7388. DOI: https://doi.org/10.1016/j.memsci.2012.09.048.

[86] Morandi, G. and Thielemans, W., "Synthesis of cellulose nanocrystals bearing photocleavable grafts by ATRP," *Polymer Chemistry*, vol. 3, no. 6, pp. 1402–1407, 2012, ISSN: 1759-9954. DOI: 10.1039/C2PY20069D.

[87] Henze, M., Mädge, D., Prucker, O., and Rühe, J., ""Grafting Through": Mechanistic Aspects of Radical Polymerization Reactions with Surface-Attached Monomers," *Macromolecules*, vol. 47, no. 9, pp. 2929–2937, 2014, ISSN: 0024-9297. DOI: https://doi.org/10.1021/ma402607d.

[88] Dogan-Guner, E. M., Brownell, S., Schueneman, G. T., Shofner, M. L., and Meredith, J. C., "Enabling zero added-coalescent waterborne acrylic coatings with cellulose nanocrystals," *Progress in Organic Coatings*, vol. 150, p. 105 969, 2021, ISSN: 0300-9440. DOI: https://doi.org/10.1016/j.porgcoat.2020.105969.

[89] Pennock, A., et al. 2014. Selecting green paint. Available from: https://greenhomeguide.com/know-how/article/selecting-green-paint, Accessed: March 12, 2019.

[90] The Society for Protetice Coatings Learning Center - VOC regulations and why they matter for your next coating project. Available from: https://www.sspc.org/learning_center/voc-regulations-and-why-they-matter-for-your-next-coating-project/, Accessed: April 17, 2019.

[91] United States Environmental Protection Agency. Ground-level Ozone Pollution. Available from: https://www.epa.gov/ground-level-ozone-pollution/ground-level-ozone-basics, Accessed: March 12, 2019.

[92] Hussain, F., Hojjati, M., Okamoto, M., and Gorga, R. E., "Review article: Polymer-matrix Nanocomposites, Processing, Manufacturing, and Application: An Overview," *Journal of Composite Materials*, vol. 40, no. 17, pp. 1511–1575, 2006. DOI: https://doi.org/10.1177/0021998306067321.

[93] Babu Valapa, R., Loganathan, S., Pugazhenthi, G., Thomas, S., and Varghese, T. O., "Chapter 2: An Overview of Polymer–Clay Nanocomposites," in *Clay-Polymer Nanocomposites*, K. Jlassi, M. M. Chehimi, and S. Thomas, Eds. Elsevier, 2017, pp. 29–81, ISBN: 978-0-323-46153-5. DOI: https://doi.org/10.1016/B978-0-323-46153-5.00002-1.

[94] Meer, S., Kausar, A., and Iqbal, T., "Attributes of polymer and silica nanoparticle composites: A review," *Polymer-Plastics Technology and Engineering*, vol. 55, no. 8, pp. 826–861, 2016, ISSN: 0360-2559. DOI: https://doi.org/10.1080/03602559.2015.1103267.

[95] Spitalsky, Z., Tasis, D., Papagelis, K., and Galiotis, C., "Carbon nanotube–polymer composites: Chemistry, processing, mechanical and electrical properties," *Progress in Polymer Science*, vol. 35, no. 3, pp. 357–401, 2010, ISSN: 0079-6700. DOI: https://doi.org/10.1016/j.progpolymsci.2009.09.003.

[96] Lee, K.-Y., *Nanocellulose and Sustainability: Production, Properties, Applications, and Case Studies*, ser. Nanocellulose and Sustainability: Production, Properties, Applications, and Case Studies. CRC Press, 2018, pp. 1–295. DOI: https://doi.org/10.1201/9781351262927.

[97] Eichhorn, S. J., Dufresne, A., Aranguren, M., Marcovich, N. E., Capadona, J. R., Rowan, S. J., Weder, C., Thielemans, W., Roman, M., Renneckar, S., Gindl, W., Veigel, S., Keckes, J., Yano, H., Abe, K., Nogi, M., Nakagaito, A. N., Mangalam, A., Simonsen, J., Benight, A. S., Bismarck, A., Berglund, L. A., and Peijs, T., "Review: current international research into cellulose nanofibres and nanocomposites," *Journal of Materials Science*, vol. 45, no. 1, pp. 1–33, 2010, ISSN: 1573-4803. DOI: https://doi.org/10.1007/s10853-009-3874-0.

[98] Miao, C. and Hamad, W., "Cellulose reinforced polymer composites and nanocomposites: a critical review," *Cellulose*, vol. 20, 2013. DOI: https://doi.org/10.1007/s10570-013-0007-3.

[99] Xu, S., Girouard, N., Schueneman, G., Shofner, M. L., and Meredith, J. C., "Mechanical and thermal properties of waterborne epoxy composites containing cellulose nanocrystals," *Polymer*, vol. 54, no. 24, pp. 6589–6598, 2013, ISSN: 0032-3861. DOI: https://doi.org/10.1016/j.polymer.2013.10.011.

[100] Abitbol, T., Prevo, B. G., Galli, C., Choudhary, S., Corwin, J., Villalpando-Páez, F., Nguyen, L., Komarov, A., Villalobos, M., Veldhuis, S. C., and Cranston, E. D., "Comparison of nanocrystalline cellulose and fumed silica in latex coatings," *Green Materials*, vol. 2, no. 4, pp. 206–221, 2014. DOI: https://doi.org/10.1680/gmat.14.00017.

[101] Pu, Y., Zhang, J., Elder, T., Deng, Y., Gatenholm, P., and Ragauskas, A. J., "Investigation into nanocellulosics versus acacia reinforced acrylic films," *Composites Part B: Engineering*, vol. 38, no. 3, pp. 360–366, 2007, ISSN: 1359-8368. DOI: https://doi.org/10.1016/j.compositesb.2006.07.008.

[102] Limousin, E., Rafaniello, I., Schäfer, T., Ballard, N., and Asua, J. M., "Linking Film Structure and Mechanical Properties in Nanocomposite Films Formed from Dispersions of Cellulose Nanocrystals and Acrylic Latexes," *Langmuir*, vol. 36, no. 8, pp. 2052–2062, 2020, ISSN: 0743-7463. DOI: https://doi.org/10.1021/acs.langmuir.9b03861.

[103] Koh, A. Y. C., Mange, S., Bothe, M., Leyrer, R. J., and Gilbert, R. G., "The influence of copolymerization with methacrylic acid on poly(butyl acrylate) film properties," *Polymer*, vol. 47, no. 4, pp. 1159–1165, 2006, ISSN: 0032-3861. DOI: https://doi.org/10.1016/j.polymer.2005.12.053.

[104] Akarsu Dulgar, C. and Serhatli, I. E., "Synthesis of poly(BA-co-MMA) dispersions having AA/MAA/AAm/MAAm comonomers and the comparison of their effect on adhesive performance," *Polymer Bulletin*, vol. 75, no. 2, pp. 877–890, 2018, ISSN: 1436-2449. DOI: 10.1007/s00289-017-2055-6.

[105] Yang, J., Zhao, J.-J., Xu, F., and Sun, R.-C., "Revealing Strong Nanocomposite Hydrogels Reinforced by Cellulose Nanocrystals: Insight into Morphologies and Interactions," *ACS Applied Materials & Interfaces*, vol. 5, no. 24, pp. 12 960–12 967, 2013, ISSN: 1944-8244. DOI: https://doi.org/10.1021/am403669n.

[106] Lu, P. and Hsieh, Y.-L., "Cellulose nanocrystal-filled poly(acrylic acid) nanocomposite fibrous membranes," *Nanotechnology*, vol. 20, no. 41, p. 415 604, 2009, ISSN: 0957-4484 1361-6528. DOI: https://doi.org/10.1088/0957-4484/20/41/415604.

[107] Sormana, J.-L., Chattopadhyay, S., and Meredith, J. C., "High-throughput mechanical characterization of free-standing polymer films," *Review of Scientific Instruments*, vol. 76, no. 6, p. 062 214, 2005. DOI: https://doi.org/10.1063/1.1926967.

[108] Boluk, Y. and Danumah, C., "Analysis of cellulose nanocrystal rod lengths by dynamic light scattering and electron microscopy," *Journal of Nanoparticle Research*, vol. 16, no. 1, p. 2174, 2013, ISSN: 1572-896X. DOI: https://doi.org/10.1007/s11051-013-2174-4.

[109] Foster, E. J., Moon, R. J., Agarwal, U. P., Bortner, M. J., Bras, J., Camarero-Espinosa, S., Chan, K. J., Clift, M. J. D., Cranston, E. D., Eichhorn, S. J., Fox, D. M., Hamad, W. Y., Heux, L., Jean, B., Korey, M., Nieh, W., Ong, K. J., Reid, M. S., Renneckar, S., Roberts, R., Shatkin, J. A., Simonsen, J., Stinson-Bagby, K., Wanasekara, N., and Youngblood, J., "Current characterization methods for cellulose nanomaterials," *Chemical Society Reviews*, vol. 47, no. 8, pp. 2609–2679, 2018, ISSN: 0306-0012. DOI: https://doi.org/10.1039/C6CS00895J.

[110] Kalia, S, Kaith, B., and Kaur, I, *Cellulose Fibers: Bio- and Nano- Polymer Composites*, ser. Green Chemistry and Technology. Springer, 2011.

[111] Limousin, E., Ballard, N., and Asua, J. M., "Synthesis of cellulose nanocrystal armored latex particles for mechanically strong nanocomposite films," *Polymer Chemistry*, vol. 10, no. 14, pp. 1823–1831, 2019, ISSN: 1759-9954. DOI: https://doi.org/10.1039/C8PY01785A.

[112] Siqueira, G., Kokkinis, D., Libanori, R., Hausmann, M. K., Gladman, A. S., Neels, A., Tingaut, P., Zimmermann, T., Lewis, J. A., and Studart, A. R., "Cellulose Nanocrystal Inks for 3D Printing of Textured Cellular Architectures," *Advanced Functional Materials*, vol. 27, no. 12, p. 1 604 619, 2017, ISSN: 1616-301X. DOI: https://doi.org/10.1002/adfm.201604619.

[113] Wang, P.-X., Hamad, W. Y., and MacLachlan, M. J., "Structure and transformation of tactoids in cellulose nanocrystal suspensions," *Nature Communications*, vol. 7, p. 11 515, 2016. DOI: https://doi.org/10.1038/ncomms11515.

[114] Tang, L. and Weder, C., "Cellulose Whisker/Epoxy Resin Nanocomposites," *ACS Applied Materials & Interfaces*, vol. 2, no. 4, pp. 1073–1080, 2010, ISSN: 1944-8244. DOI: https://doi.org/10.1021/am900830h.

[115] Annamalai, P. K., Dagnon, K. L., Monemian, S., Foster, E. J., Rowan, S. J., and Weder, C., "Water-responsive mechanically adaptive nanocomposites based on styrene –butadiene rubber and cellulose nanocrystals-processing matters," *ACS Applied Materials & Interfaces*, vol. 6, no. 2, pp. 967–976, 2014, ISSN: 1944-8244. DOI: 10.1021/am404382x.

[116] Ben Mabrouk, A., Rei Vilar, M., Magnin, A., Belgacem, M. N., and Boufi, S., "Synthesis and characterization of cellulose whiskers/polymer nanocomposite dispersion by mini-emulsion polymerization," *Journal of Colloid and Interface Science*, vol. 363, no. 1, pp. 129–136, 2011, ISSN: 0021-9797. DOI: https://doi.org/10.1016/j.jcis.2011.07.050.

[117] Podgorski, L., Meijer, M. de, and Lanvin, J. D., "Influence of Coating Formulation on Its Mechanical Properties and Cracking Resistance," *Coatings*, vol. 7, no. 10, 2017, ISSN: 2079-6412. DOI: https://doi.org/10.3390/coatings7100163.

[118] Dastjerdi, Z., Cranston, E. D., and Dubé, M. A., "Pressure sensitive adhesive property modification using cellulose nanocrystals," *International Journal of Adhesion and Adhesives*, vol. 81, pp. 36–42, 2018, ISSN: 0143-7496. DOI: https://doi.org/10.1016/j.ijadhadh.2017.11.009.

[119] Ding, T., Daniels, E. S., El-Aasser, M. S., and Klein, A., "Synthesis and characterization of functionalized polymer latex particles through a designed semicontinuous emulsion polymerization process," *Journal of Applied Polymer Science*, vol. 97, no. 1, pp. 248–256, 2005, ISSN: 0021-8995. DOI: https://doi.org/10.1002/app.21678.

[120] Santos, A. M., Guillot, J., and McKenna, T. F., "Partitioning of styrene, butyl acrylate and methacrylic acid in emulsion systems," *Chemical Engineering Science*, vol. 53, no. 12, pp. 2143–2151, 1998, ISSN: 0009-2509. DOI: https://doi.org/10.1016/S0009-2509(98)00031-1.

[121] Wang, T., Canetta, E., Weerakkody, T. G., Keddie, J. L., and Rivas, U., "pH Dependence of the Properties of Waterborne Pressure-Sensitive Adhesives Containing Acrylic Acid," *ACS Applied Materials & Interfaces*, vol. 1, no. 3, pp. 631–639, 2009, ISSN: 1944-8244. DOI: https://doi.org/10.1021/am800179y.

[122] Feng, J. and Winnik, M. A., "Effect of Water on Polymer Diffusion in Latex Films," *Macromolecules*, vol. 30, no. 15, pp. 4324–4331, 1997, ISSN: 0024-9297. DOI: https://doi.org/10.1021/ma970174+.

[123] Voogt, B., Huinink, H. P., Erich, S. J. F., Scheerder, J., Venema, P., Keddie, J. L., and Adan, O. C. G., "Film Formation of High T_g Latex Using Hydroplasticization: Explanations from NMR Relaxometry," *Langmuir*, vol. 35, no. 38, pp. 12 418–12 427, 2019, ISSN: 0743-7463. DOI: https://doi.org/10.1021/acs.langmuir.9b01353.

[124] Dow Coating Materials. Lower VOC-Faster Dry Time-Higher Productivity. Available from: http://msdssearch.dow.com/PublishedLiteratureDOWCOM/dh_08c0/0901b803808c0792.pdf?filepath=dcc_na/pdfs/noreg/884-00023.pdf&fromPage=GetDoc, Accessed: July 17, 2019.

[125] Santos, P., Paula, N. F., Pagani, R. A., Caldato, R. A., Da Silva, R., and Barrios, S. B., "Low-VOC Coalescents," *Coating World - Technical Paper*, 2019.

[126] Ramos-Fernández, J. M., Guillem, C., Lopez-Buendía, A., Paulis, M., and Asua, J. M., "Synthesis of poly-(BA-co-MMA) latexes filled with SiO_2 for coating in construction applications," *Progress in Organic Coatings*, vol. 72, no. 3, pp. 438–442, 2011, ISSN: 0300-9440. DOI: https://doi.org/10.1016/j.porgcoat.2011.05.017.

[127] Maren, R., "Toxicity of Cellulose Nanocrystals: A Review," *Industrial Biotechnology*, vol. 11, no. 1, pp. 25–33, 2015. DOI: https://doi.org/10.1089/ind.2014.0024.

[128] Gu, H., Reiner, R., Bergman, R., and Rudie, A., "LCA Study for Pilot Scale Production of Cellulose Nano Crystals (CNC) from Wood Pulp," *LCA XV Paper Proceedings – A Bright Green Future*, 2013.

[129] Arvidsson, R., Nguyen, D., and Svanstrom, M., "Life Cycle Assessment of Cellulose Nanofibrils Production by Mechanical Treatment and Two Different Pretreatment Processes," *Environmental Science & Technology*, vol. 49, no. 11, pp. 6881–6890, 2015, ISSN: 0013-936X. DOI: 10.1021/acs.est.5b00888.

[130] Li, Q., McGinnis, S., Sydnor, C., Wong, A., and Renneckar, S., "Nanocellulose Life Cycle Assessment," *ACS Sustainable Chemistry & Engineering*, vol. 1, no. 8, pp. 919–928, 2013. DOI: https://doi.org/10.1021/sc4000225.

[131] Assis, C. A. de, Houtman, C., Phillips, R., Bilek, E., Rojas, O. J., Pal, L., Peresin, M. S., Jameel, H., and Gonzalez, R., "Conversion Economics of Forest Biomaterials: Risk and Financial Analysis of CNC Manufacturing," *Biofuels, Bioproducts and Biorefining*, vol. 11, no. 4, pp. 682–700, 2017, ISSN: 1932-104X. DOI: https://doi.org/10.1002/bbb.1782.

[132] Xie, H., Du, H., Yang, X., and Si, C., "Recent Strategies in Preparation of Cellulose Nanocrystals and Cellulose Nanofibrils Derived from Raw Cellulose Materials," *International Journal of Polymer Science*, vol. 2018, p. 7 923 068, 2018, ISSN: 1687-9422. DOI: https://doi.org/10.1155/2018/7923068.

[133] Wang, Q. Q., Zhu, J. Y., Reiner, R. S., Verrill, S. P., Baxa, U., and McNeil, S. E., "Approaching zero cellulose loss in cellulose nanocrystal (CNC) production: recovery and characterization of cellulosic solid residues (CSR) and CNC," *Cellulose*, vol. 19, no. 6, pp. 2033–2047, 2012, ISSN: 1572-882X. DOI: https://doi.org/10.1007/s10570-012-9765-6.

[134] Nelson, K., Retsina, T., Iakovlev, M., Heiningen, A. van, Deng, Y., Shatkin, J. A., and Mulyadi, A., "American Process: Production of Low Cost Nanocellulose for Renewable, Advanced Materials Applications," in *Materials Research for Manufacturing: An Industrial Perspective of Turning Materials into New Products*, L. D.

Madsen and E. B. Svedberg, Eds. Cham: Springer International Publishing, 2016, pp. 267–302, ISBN: 978-3-319-23419-9. DOI: https://doi.org/10.1007/978-3-319-23419-9_9.

[135] Blue Goose Biorefineries Inc., R3™ technology. Available from: https://bluegoosebiorefineries.com/process/, Accessed: April 17, 2019.

[136] Kedzior, S. A., Gabriel, V. A., Dubé, M. A., and Cranston, E. D., "Nanocellulose in Emulsions and Heterogeneous Water-Based Polymer Systems: A Review," *Advanced Materials*, p. 2 002 404, ISSN: 0935-9648. DOI: https://doi.org/10.1002/adma.202002404.

[137] Chang, H., Luo, J., Bakhtiary Davijani, A. A., Chien, A.-T., Wang, P.-H., Liu, H. C., and Kumar, S., "Individually Dispersed Wood-Based Cellulose Nanocrystals," *ACS Applied Materials & Interfaces*, vol. 8, no. 9, pp. 5768–5771, 2016, ISSN: 1944-8244. DOI: https://doi.org/10.1021/acsami.6b00094.

[138] Viet, D., Beck-Candanedo, S., and Gray, D. G., "Dispersion of cellulose nanocrystals in polar organic solvents," *Cellulose*, vol. 14, no. 2, pp. 109–113, 2007, ISSN: 1572-882X. DOI: https://doi.org/10.1007/s10570-006-9093-9.

[139] Siqueira, G., Bras, J., Follain, N., Belbekhouche, S., Marais, S., and Dufresne, A., "Thermal and mechanical properties of bio-nanocomposites reinforced by Luffa cylindrica cellulose nanocrystals," *Carbohydrate Polymers*, vol. 91, no. 2, pp. 711–717, 2013, ISSN: 0144-8617. DOI: https://doi.org/10.1016/j.carbpol.2012.08.057.

[140] Missoum, K., Bras, J., and Belgacem, M. N., "Organization of aliphatic chains grafted on nanofibrillated cellulose and influence on final properties," *Cellulose*, vol. 19, no. 6, pp. 1957–1973, 2012, ISSN: 1572-882X. DOI: https://doi.org/10.1007/s10570-012-9780-7.

[141] Rueda, L., Fernández d'Arlas, B., Zhou, Q., Berglund, L. A., Corcuera, M. A., Mondragon, I., and Eceiza, A., "Isocyanate-rich cellulose nanocrystals and their selective insertion in elastomeric polyurethane," *Composites Science and Technology*, vol. 71, no. 16, pp. 1953–1960, 2011, ISSN: 0266-3538. DOI: https://doi.org/10.1016/j.compscitech.2011.09.014.

[142] Siqueira, G., Bras, J., and Dufresne, A., "New Process of Chemical Grafting of Cellulose Nanoparticles with a Long Chain Isocyanate," *Langmuir*, vol. 26, no. 1, pp. 402–411, 2010, ISSN: 0743-7463. DOI: https://doi.org/10.1021/la9028595.

[143] Gwon, J.-G., Cho, H.-J., Chun, S.-J., Lee, S., Wu, Q., and Lee, S.-Y., "Physiochemical, optical and mechanical properties of poly(lactic acid) nanocomposites filled with toluene diisocyanate grafted cellulose nanocrystals," *RSC Advances*, vol. 6, no. 12, pp. 9438–9445, 2016. DOI: http://dx.doi.org/10.1039/C5RA26337A.

[144] Gwon, J.-G., Cho, H.-J., Chun, S.-J., Lee, S., Wu, Q., Li, M.-C., and Lee, S.-Y., "Mechanical and thermal properties of toluene diisocyanate-modified cellulose nanocrystal nanocomposites using semi-crystalline poly(lactic acid) as a base matrix," *RSC Advances*, vol. 6, no. 77, pp. 73 879–73 886, 2016. DOI: http://dx.doi.org/10.1039/C6RA10993D.

[145] Abushammala, H. and Mao, J., "A Review of the Surface Modification of Cellulose and Nanocellulose Using Aliphatic and Aromatic Mono- and Di-Isocyanates," *Molecules*, vol. 24, no. 15, 2019, ISSN: 1420-3049. DOI: https://doi.org/10.3390/molecules24152782.

[146] Girouard, N. M., Xu, S., Schueneman, G. T., Shofner, M. L., and Meredith, J. C., "Site-Selective Modification of Cellulose Nanocrystals with Isophorone Diisocyanate and Formation of Polyurethane-CNC Composites," *ACS Applied Materials & Interfaces*, vol. 8, no. 2, pp. 1458–1467, 2016, ISSN: 1944-8244. DOI: https://doi.org/10.1021/acsami.5b10723.

[147] Qu, Z., Schueneman, G. T., Shofner, M. L., and Meredith, J. C., "Acrylic Functionalization of Cellulose Nanocrystals with 2-Isocyanatoethyl Methacrylate and Formation of Composites with Poly(methyl methacrylate)," *ACS Omega*, 2020, ISSN: 2470-1343. DOI: https://doi.org/10.1021/acsomega.0c04246.

[148] Kedzior, S. A., Zoppe, J. O., Berry, R. M., and Cranston, E. D., "Recent advances and an industrial perspective of cellulose nanocrystal functionalization through polymer grafting," *Current Opinion in Solid State and Materials Science*, vol. 23, no. 2, pp. 74–91, 2019, ISSN: 1359-0286. DOI: https://doi.org/10.1016/j.cossms.2018.11.005.

[149] Wohlhauser, S., Delepierre, G., Labet, M., Morandi, G., Thielemans, W., Weder, C., and Zoppe, J. O., "Grafting Polymers from Cellulose Nanocrystals: Synthesis, Properties, and Applications," *Macromolecules*, vol. 51, no. 16, pp. 6157–6189, 2018, ISSN: 0024-9297. DOI: https://doi.org/10.1021/acs.macromol.8b00733.

[150] Eyley, S. and Thielemans, W., "Surface modification of cellulose nanocrystals," *Nanoscale*, vol. 6, no. 14, pp. 7764–7779, 2014, ISSN: 2040-3364. DOI: http://dx.doi.org/10.1039/C4NR01756K.

[151] Pinheiro, I. F., Ferreira, F. V., Alves, G. F., Rodolfo, A., Morales, A. R., and Mei, L. H. I., "Biodegradable PBAT-Based Nanocomposites Reinforced with Functionalized Cellulose Nanocrystals from Pseudobombax munguba: Rheological, Thermal, Mechanical and Biodegradability Properties," *Journal of Polymers and the Environment*, vol. 27, no. 4, pp. 757–766, 2019, ISSN: 1572-8919. DOI: https://doi.org/10.1007/s10924-019-01389-z.

[152] Morelli, C. L., Belgacem, N., Bretas, R. E. S., and Bras, J., "Melt extruded nanocomposites of polybutylene adipate-co-terephthalate (PBAT) with phenylbutyl isocyanate modified cellulose nanocrystals," *Journal of Applied Polymer Science*, vol. 133, no. 34, 2016, ISSN: 0021-8995. DOI: https://doi.org/10.1002/app.43678.

[153] Zoppe, J. O., Peresin, M. S., Habibi, Y., Venditti, R. A., and Rojas, O. J., "Reinforcing Poly(ϵ-caprolactone) Nanofibers with Cellulose Nanocrystals," *ACS Applied Materials & Interfaces*, vol. 1, no. 9, pp. 1996–2004, 2009, ISSN: 1944-8244. DOI: https://doi.org/10.1021/am9003705.

[154] Yu, H.-Y. and Qin, Z.-Y., "Surface grafting of cellulose nanocrystals with poly(3-hydroxybutyrate-co-3-hydroxyvalerate)," *Carbohydrate Polymers*, vol. 101, pp. 471–478, 2014, ISSN: 0144-8617. DOI: https://doi.org/10.1016/j.carbpol.2013.09.048.

[155] Morelli, C. L., Belgacem, M. N., Branciforti, M. C., Bretas, R. E. S., Crisci, A., and Bras, J., "Supramolecular aromatic interactions to enhance biodegradable film properties through incorporation of functionalized cellulose nanocrystals," *Composites Part A: Applied Science and Manufacturing*, vol. 83, pp. 80–88, 2016, ISSN: 1359-835X. DOI: https://doi.org/10.1016/j.compositesa.2015.10.038.

[156] Park, S., Baker, J. O., Himmel, M. E., Parilla, P. A., and Johnson, D. K., "Cellulose crystallinity index: measurement techniques and their impact on interpreting cellulase performance," *Biotechnology for Biofuels*, vol. 3, no. 1, p. 10, 2010, ISSN: 1754-6834. DOI: https://doi.org/10.1186/1754-6834-3-10.

[157] Gong, J., Li, J., Xu, J., Xiang, Z., and Mo, L., "Research on cellulose nanocrystals produced from cellulose sources with various polymorphs," *RSC Advances*, vol. 7, no. 53, pp. 33 486–33 493, 2017. DOI: https://doi.org/10.1039/C7RA06222B.

[158] Langan, P., Nishiyama, Y., and Chanzy, H., "X-ray Structure of Mercerized Cellulose II at 1 Å Resolution," *Biomacromolecules*, vol. 2, no. 2, pp. 410–416, 2001, ISSN: 1525-7797. DOI: https://doi.org/10.1021/bm005612q.

[159] Espino-Pérez, E., Bras, J., Ducruet, V., Guinault, A., Dufresne, A., and Domenek, S., "Influence of chemical surface modification of cellulose nanowhiskers on thermal, mechanical, and barrier properties of poly(lactide) based bionanocomposites," *European Polymer Journal*, vol. 49, no. 10, pp. 3144–3154, 2013, ISSN: 0014-3057. DOI: https://doi.org/10.1016/j.eurpolymj.2013.07.017.

[160] Rämänen, P., Penttilä, P. A., Svedström, K., Maunu, S. L., and Serimaa, R., "The effect of drying method on the properties and nanoscale structure of cellulose whiskers," *Cellulose*, vol. 19, no. 3, pp. 901–912, 2012, ISSN: 1572-882X. DOI: https://doi.org/10.1007/s10570-012-9695-3.

[161] Chambers, J., Jiricny, J., and Reese, C. B., "The thermal decomposition of polyurethanes and polyisocyanurates," *Fire and Materials*, vol. 5, no. 4, pp. 133–141, 1981, ISSN: 0308-0501. DOI: https://doi.org/10.1002/fam.810050402.

[162] Zhang, Z., Tam, K. C., Sèbe, G., and Wang, X., "Convenient characterization of polymers grafted on cellulose nanocrystals via SI-ATRP without chain cleavage," *Carbohydrate Polymers*, vol. 199, pp. 603–609, 2018, ISSN: 0144-8617. DOI: https://doi.org/10.1016/j.carbpol.2018.07.060.

[163] Zhang, J., Li, M.-C., Zhang, X., Ren, S., Dong, L., Lee, S., Cheng, H. N., Lei, T., and Wu, Q., "Surface modified cellulose nanocrystals for tailoring interfacial miscibility and microphase separation of polymer nanocomposites," *Cellulose*, vol. 26, no. 7, pp. 4301–4312, 2019, ISSN: 1572-882X. DOI: https://doi.org/10.1007/s10570-019-02379-z.

[164] Yu, J., Wang, C., Wang, J., and Chu, F., "In situ development of self-reinforced cellulose nanocrystals based thermoplastic elastomers by atom transfer radical polymerization," *Carbohydrate Polymers*, vol. 141, pp. 143–150, 2016, ISSN: 0144-8617. DOI: https://doi.org/10.1016/j.carbpol.2016.01.006.

[165] DeFusco, A. J., Sehgal, K. C., and Bassett, D. R., "Overview of Uses of Polymer Latexes," in *Polymeric Dispersions: Principles and Applications*, J. M. Asua, Ed. Dordrecht: Springer Netherlands, 1997, pp. 379–396, ISBN: 978-94-011-5512-0. DOI: 10.1007/978-94-011-5512-0_25.

[166] Richey, B. and Burch, M., "Applications for Decorative and Protective Coatings," in *Polymer Dispersions and Their Industrial Applications*. 2002, pp. 123–161. DOI: https://doi.org/10.1002/3527600582.ch6.

[167] Lovell, P. A. and Schork, F. J., "Fundamentals of Emulsion Polymerization," *Biomacromolecules*, vol. 21, no. 11, pp. 4396–4441, 2020, ISSN: 1525-7797. DOI: 10.1021/acs.biomac.0c00769.

[168] Antonietti, M. and Landfester, K., "Polyreactions in Miniemulsions," *Progress in Polymer Science*, vol. 27, pp. 689–757, 2002. DOI: 10.1016/S0079-6700(01)00051-X.

[169] Hecht, L. L., Wagner, C., Landfester, K., and Schuchmann, H. P., "Surfactant Concentration Regime in Miniemulsion Polymerization for the Formation of MMA Nanodroplets by High-Pressure Homogenization," *Langmuir*, vol. 27, no. 6, pp. 2279–2285, 2011, ISSN: 0743-7463. DOI: 10.1021/la104480s.

[170] Landfester, K., Bechthold, N., Tiarks, F., and Antonietti, M., "Formulation and Stability Mechanisms of Polymerizable Miniemulsions," *Macromolecules*, vol. 32, no. 16, pp. 5222–5228, 1999, ISSN: 0024-9297. DOI: 10.1021/ma990299+.

[171] Theisinger, S., Schoeller, K., Osborn, B., Sarkar, M., and Landfester, K., "Encapsulation of a Fragrance via Miniemulsion Polymerization for Temperature-Controlled Release," *Macromolecular Chemistry and Physics*, vol. 210, no. 6, pp. 411–420, 2009, ISSN: 1022-1352. DOI: https://doi.org/10.1002/macp.200800499.

[172] Barraza, H. J., Pompeo, F., O'Rea, E. A., and Resasco, D. E., "SWNT-Filled Thermoplastic and Elastomeric Composites Prepared by Miniemulsion Polymerization," *Nano Letters*, vol. 2, no. 8, pp. 797–802, 2002, ISSN: 1530-6984. DOI: 10.1021/nl0256208.

[173] Han, H., Lee, J., Park, D. W., and Shim, S. E., "Surface modification of carbon black by oleic acid for miniemulsion polymerization of styrene," *Macromolecular Research*, vol. 18, no. 5, pp. 435–441, 2010, ISSN: 2092-7673. DOI: 10.1007/s13233-010-0505-1.

[174] Tiarks, F., Landfester, K., and Antonietti, M., "Silica Nanoparticles as Surfactants and Fillers for Latexes Made by Miniemulsion Polymerization," *Langmuir*, vol. 17, no. 19, pp. 5775–5780, 2001, ISSN: 0743-7463. DOI: 10.1021/la010445g.

[175] Zhang, S.-W., Zhou, S.-X., Weng, Y.-M., and Wu, L.-M., "Synthesis of SiO_2/Polystyrene Nanocomposite Particles via Miniemulsion Polymerization," *Langmuir*, vol. 21, no. 6, pp. 2124–2128, 2005, ISSN: 0743-7463. DOI: 10.1021/la047652b.

[176] Erdem, B., Sudol, E. D., Dimonie, V. L., and El-Aasser, M. S., "Encapsulation of inorganic particles via miniemulsion polymerization. III. Characterization of encapsulation," *Journal of Polymer Science Part A: Polymer Chemistry*, vol. 38, no. 24, pp. 4441–4450, 2000, ISSN: 0887-624X. DOI: https://doi.org/10.1002/1099-0518(20001215)38:24$\langle$4441::AID-POLA130$\rangle$3.0.CO;2-U.

[177] Liu, X., Guan, Y., Ma, Z., and Liu, H., "Surface Modification and Characterization of Magnetic Polymer Nanospheres Prepared by Miniemulsion Polymerization," *Langmuir*, vol. 20, no. 23, pp. 10 278–10 282, 2004, ISSN: 0743-7463. DOI: 10.1021/la0491908.

[178] Voorn, D. J., Ming, W., and Herk, A. M. van, "Clay Platelets Encapsulated Inside Latex Particles," *Macromolecules*, vol. 39, no. 14, pp. 4654–4656, 2006, ISSN: 0024-9297. DOI: 10.1021/ma060900l.

[179] Weiss, C. K. and Landfester, K., "Miniemulsion Polymerization as a Means to Encapsulate Organic and Inorganic Materials," in *Hybrid Latex Particles: Preparation with (Mini)emulsion Polymerization*, A. M. van Herk and K. Landfester, Eds. Berlin, Heidelberg: Springer Berlin Heidelberg, 2010, pp. 185–236, ISBN: 978-3-642-16060-8. DOI: 10.1007/12_2010_61.

[180] Kedzior, S. A., Kiriakou, M., Niinivaara, E., Dubé, M. A., Fraschini, C., Berry, R. M., and Cranston, E. D., "Incorporating Cellulose Nanocrystals into the Core of Polymer Latex Particles via Polymer Grafting," *ACS Macro Letters*, vol. 7, no. 8, pp. 990–996, 2018. DOI: 10.1021/acsmacrolett.8b00334.

[181] Yu, Q., Yang, W., Wang, Q., Dong, W., Du, M., and Ma, P., "Functionalization of cellulose nanocrystals with γ-MPS and its effect on the adhesive behavior of acrylic pressure sensitive adhesives," *Carbohydrate Polymers*, vol. 217, pp. 168–177, 2019, ISSN: 0144-8617. DOI: https://doi.org/10.1016/j.carbpol.2019.04.049.

[182] Lizundia, E., Meaurio, E., and Vilas, J. L., "Chapter 3 - Grafting of Cellulose Nanocrystals," in *Multifunctional Polymeric Nanocomposites Based on Cellulosic Reinforcements*, D. Puglia, E. Fortunati, and J. M. Kenny, Eds. William Andrew Publishing, 2016, pp. 61–113, ISBN: 978-0-323-44248-0. DOI: https://doi.org/10.1016/B978-0-323-44248-0.00003-1.

[183] Dimonie, V., Sudol, D., and El-Aasser, M., "Role of Surfactants in Emulsion Polymerization Polymers by Design," *Revista de Chimie*, vol. 59, pp. 1218–1221, 2008. DOI: 10.37358/RC.08.11.2005.

[184] Fontenot, K. and Schork, F. J., "Batch polymerization of methyl methacrylate in mini/macroemulsions," *Journal of Applied Polymer Science*, vol. 49, no. 4, pp. 633–655, 1993, ISSN: 0021-8995. DOI: https://doi.org/10.1002/app.1993.070490410.

[185] Bradley, M. A., Prescott, S. W., Schoonbrood, H. A. S., Landfester, K., and Grieser, F., "Miniemulsion Copolymerization of Methyl Methacrylate and Butyl Acrylate by Ultrasonic Initiation," *Macromolecules*, vol. 38, no. 15, pp. 6346–6351, 2005, ISSN: 0024-9297. DOI: 10.1021/ma0473622.

[186] Chappelow, C. C., Byerley, T. J., Pinzino, C. S., Millich, F., and Eick, J. D., "Design and development of isocyanatoacrylates as dental adhesives," *J Dent Res*, vol. 75, no. 2, pp. 761–7, 1996, ISSN: 0022-0345 (Print) 0022-0345. DOI: 10.1177/00220345960750020501.

[187] Elmabrouk, A. B., Wim, T., Dufresne, A., and Boufi, S., "Preparation of poly(styrene-co-hexylacrylate)/cellulose whiskers nanocomposites via miniemulsion polymerization," *Journal of Applied Polymer Science*, vol. 114, no. 5, pp. 2946–2955, 2009, ISSN: 0021-8995. DOI: https://doi.org/10.1002/app.30886.

[188] Herk, A. M. van, "Encapsulation with conventional emulsion polymerization," in *Encyclopedia of Polymeric Nanomaterials*, S. Kobayashi and K. Müllen, Eds. Berlin, Heidelberg: Springer Berlin Heidelberg, 2021, pp. 1–6, ISBN: 978-3-642-36199-9. DOI: 10.1007/978-3-642-36199-9_260-1.

[189] Paulis, M. and Leiza, J. R., "Encapsulation with Miniemulsion Polymerization," in *Encyclopedia of Polymeric Nanomaterials*, S. Kobayashi and K. Müllen, Eds. Verlag Berlin Heidelberg: Springer, 2014. DOI: DOI10.1007/978-3-642-36199-9_261-1.

[190] Fox, D. M., Rodriguez, R. S., Devilbiss, M. N., Woodcock, J., Davis, C. S., Sinko, R., Keten, S., and Gilman, J. W., "Simultaneously Tailoring Surface Energies and Thermal Stabilities of Cellulose Nanocrystals Using Ion Exchange: Effects on Polymer Composite Properties for Transportation, Infrastructure, and Renewable Energy Applications," *ACS Applied Materials & Interfaces*, vol. 8, no. 40, pp. 27 270–27 281, 2016, ISSN: 1944-8244. DOI: 10.1021/acsami.6b06083.

[191] Nagata, K. and Takase, H., "Effect of glass transition temperature of polymers on rheological behavior of alumina suspension and properties of alumina green sheets," *Journal of The Ceramic Society of Japan*, vol. 116, pp. 298–302, 2008. DOI: https://doi.org/10.2109/jcersj2.116.298.

[192] Brand, J., Pecastaings, G., and Sèbe, G., "A versatile method for the surface tailoring of cellulose nanocrystal building blocks by acylation with functional vinyl esters," *Carbohydr Polym*, vol. 169, pp. 189–197, 2017, ISSN: 0144-8617. DOI: https://doi.org/10.1016/j.carbpol.2017.03.077.

[193] Wu, X., Moon, R., and Martini, A., "Crystalline cellulose elastic modulus predicted by atomistic models of uniform deformation and nanoscale indentation," *Cellulose*, vol. 20, 2012. DOI: https://doi.org/10.1007/s10570-012-9823-0.

[194] Bullard, K. K., Srinivasarao, M., and Gutekunst, W. R., "Modification of cellulose nanocrystal surface chemistry with diverse nucleophiles for materials integration," *Journal of Materials Chemistry A*, vol. 8, no. 35, pp. 18 024–18 031, 2020, ISSN: 2050-7488. DOI: http://dx.doi.org/10.1039/D0TA05757F.

[195] Majoinen, J., Walther, A., McKee, J. R., Kontturi, E., Aseyev, V., Malho, J. M., Ruokolainen, J., and Ikkala, O., "Polyelectrolyte Brushes Grafted from Cellulose Nanocrystals Using Cu-Mediated Surface-Initiated Controlled Radical Polymerization," *Biomacromolecules*, vol. 12, no. 8, pp. 2997–3006, 2011, ISSN: 1525-7797. DOI: https://doi.org/10.1021/bm200613y.

[196] Zoppe, J. O., Ataman, N. C., Mocny, P., Wang, J., Moraes, J., and Klok, H.-A., "Surface-Initiated Controlled Radical Polymerization: State-of-the-Art, Opportunities, and Challenges in Surface and Interface Engineering with Polymer Brushes," *Chemical Reviews*, vol. 117, no. 3, pp. 1105–1318, 2017, ISSN: 0009-2665. DOI: https://doi.org/10.1021/acs.chemrev.6b00314.

VITA

Ezgi M. Dogan Guner was born in August 1991 in Ankara, Turkey. She earned two Bachelor of Science degrees in Food Engineering and Chemical Engineering from the Middle East Technical University (METU) in June 2014. While engaging in a master's degree in the METU after graduation, she was awarded Fulbright Scholarship, which brought her to the United States. Meanwhile, she earned her first Master of Science degree from the METU in August 2016. After that, she received another Master of Science degree in Chemical Engineering from the University of Massachusetts Lowell in May 2017 by studying structure-property relationship in hydrogen peroxide encapsulated silica hydrogels. Next, she joined the School of Chemical and Biomolecular Engineering at the Georgia Institute of Technology in August 2017 to pursue a Doctor of Philosophy (Ph.D.) degree. During her Ph.D. studies, Ezgi investigated the use of cellulose nanocrystals in waterborne acrylic formulations for more environmentally friendly coatings.